An analysis of Pc5 pulsations observed in the SuperDARN radar data

by

Lindsay Gerald Magnus

A thesis submitted in fulfilment of the academic
requirements for the degree of
Doctor Of Philosophy
in the School of Pure and Applied Physics,
University of KwaZulu-Natal,
Durban

March 2009

As the candidate's supervisor I have/have not approved this thesis for submission

Signed: ..... Name: ..... Date: .....

As the candidate's supervisor I have/have not approved this thesis for submission

Signed: ..... Name: ..... Date: .....

Abstract

This thesis deals with the development of automatic methods for finding pulsation events in time series produced by the radars in the SuperDARN network. These methods are then applied to the detection and analysis of pulsation events illustrating the relative usefulness of radar data for the study of global pulsation dynamics.

Each of the SuperDARN radars produces 1200 Doppler velocity records every hour. If backscatter is present, and there is a pulsation occurring in the same region as the scatter, the pulsation can be measured as periodic changes in the Doppler velocity of that record. There are over 85 million Doppler velocity data records for 2004. In order to identify pulsations in these data, an automated pulsation finder was developed. All records with significant peaks in the FFT spectra were tagged as having a pulsation present.

If a record had less than 20% data missing it was termed a clean record as it was suitable for use with the automated pulsation finder. As pulsations can only be observed if there are scatter, an investigation into scatter characteristics are presented. It is shown that the occurrence of clean records is most strongly influenced by IMF B_z, and the underlying spatial structure of the SuperDARN network.

The results for the automated pulsation finder for 2004 are then presented. It was found that the average daily distribution of pulsation events, shown as a function of pulsation frequency, followed $1/f$ distribution with no distinct peaks. It was also found, however, that the standard deviation of the average showed peaks close to the "magic" frequencies indicating that on average there is more variation at these frequencies that any of the other pulsation frequencies measured.

The occurrence of pulsations followed the clean scatter statistics both temporally and directionally telling us that the network is not suited for studying global pulsation dynamics because the variations in scatter dominated any variations in pulsation occurrence.

Data from a few events identified by the pulsation finder are then presented to illustrate the advantages and disadvantages of using SuperDARN data for pulsation event studies. The events show a pulsation that occurs at its fundamental and third harmonics, an aliased pulsation, a pulsation, interrupted by sounding frequency changes, that shows how ionospheric scatter was tagged as ground scatter and how data from two overlapping pulsations in different radars can be merged to give the poloidal and toroidal characteristics of the event.

Preface

The experimental work described in this thesis was carried out in the School of Pure and Applied Physics, University of KwaZulu-Natal, Durban, from March 2004 to March 2009 under the supervision of Professors J. P. S. Rash and A. D. M. Walker.

These studies represent original work by the author and have not otherwise been submitted in any form for any degree or diploma to any tertiary institution. Where use has been made of the work of others it is duly acknowledged in the text.

Declaration - Plagiarism

I, ... declare that

1. The research reported in this thesis, except where otherwise indicated, is my original research.
2. This thesis has not been submitted for any degree or examination at any other university.
3. This thesis does not contain other persons' data, pictures, graphs or other information, unless specifically acknowledged as being sourced from other persons.
4. This thesis does not contain other persons' writing, unless specifically acknowledged as being sourced from other researchers. Where other written sources have been quoted, then:
   (a) Their words have been re-written but the general information attributed to them has been referenced
   (b) Where their exact words have been used, then their writing has been placed in italics and inside quotation marks, and referenced.
5. This thesis does not contain text, graphics or tables copied and pasted from the Internet, unless specifically acknowledged, and the source being detailed in the thesis and in the References sections.

Signed: .....

Acknowledgements

Data were used from all the radars in the SuperDARN network. I would like to acknowledge the individual funders of each of the different radars who realise that the total network is greater than the sum of the different radars. A big word of thanks goes to all the technical staff at all the radars without whom the network would not function.

I would also like to thank the South African National Research Foundation for funding the SHARE project that runs the SANAE SuperDARN radar.

GOES 12 data were from Dr. H. Singer at NOAA/SEC, ACE MAG data were from N. Ness at the Bartol Research Institute and ACE SWEPAM data were from D. J. McComas at the Los Alamos National Laboratory.

The BAS low power magnetometer data were from M. Freeman at the British Antarctic Survey.

The SuperDARN data was read using software developed and maintained by the TIGER group in Australia. Thank you to C. Waters and P. Ponomarenko for the initial IDL software. The ray tracing in chapter 14 was done with software from QinetiQ.

I would also like to thank the Hermanus Magnetic Observatory especially Dr. P. Sutcliffe for making this research opportunity available to me. To Dr. L. McKinnell, I know at times it seemed like it would never end so thank you for your patience. To the rest of the staff and students of the HMO, thank you for making it a pleasure to go into work every day.

To my two supervisors, Professsors J. P. S. Rash and A. D. M. Walker, and the staff at UKZN, thank you for easing me into the SuperDARN community and for being there as I fumbled to find my feet.

A PhD is a process that requires support and encouragement from one's family, thank you all for what you have done for me.

Finally I would like to dedicate this work to my Mother whose support throughout my life made it possible for me to arrive at this point.

Contents

List of Figures

List of Tables

Chapter 1

Introduction

This chapter outlines the history of pulsation observations and its theory. Then follows the problem statement and an outline of the thesis.

1.1 Historical outline

Geomagnetic micropulsations, pulsations for short, were first reported in 1861 by Stewart [60]. There he described a number of variations in the magnetic field observed with magnetograms at Kew Observatory. Dungey, [24] [25], was the first to propose that pulsations were in fact Alfvèn standing waves. The classification of the types of pulsations that is in use today was accepted by the International Association of Geomagnetism and Aeronomy (IAGA) in 1964 [35]. The classification is based on the duration of the pulsation, either continuous or impulsive, and the period of the pulsation (see table 1.1).

Samson *et al* made a comprehensive study of long-period geomagnetic pulsations [53]. In this paper they demonstrated that the amplitude of pulsations with a frequency of approximately 5 mHz varies through local time. The structure of this variation showed that the amplitude of the pulsations peaks just after noon local time and then decreased until just after midnight local time. The amplitudes also peaked in geomagnetic latitude with the polarisation of the pulsation switching either side of the time and latitude peaks.

	Label	Period range/[s]	Frequency range/[mHz]
Continuous pulsations	Pc1	0.2 - 5	200 - 5000
	Pc2	5 - 10	100 - 200
	Pc3	10 - 45	22 - 100
	Pc4	45 - 150	6.7 - 22
	Pc5	150 - 600	1.67 - 6.7
Impulsive pulsations	Pi1	1 - 40	25 - 1000
	Pi2	40 - 150	6.7 - 25

Table 1.1: IAGA classification of pulsations.

The authors concluded that the structure observed was a manifestation of a toroidal mode eigenoscillation of the geomagnetic lines of force (field line resonant pulsation) driven by a Kelvin-Helmholtz instability.

Southwood created a simple model for the magnetosphere [58]. In the model the magnetic field is straight in the direction of the z axis. In order to maintain the realistic variation of Alfvén velocity with x a non-realistic number density variation was introduced $n(x)$. There are boundaries in x and z, but not in y. Using a finite length field line in z and no mention of the boundaries in x, Southwood showed that there are two physical points of interest in x, namely a turning point and a resonant point. He went on to show that the value of the electric field perturbation will be finite at the resonance due to losses such as collisionless damping or due to a resistive ionosphere. His discussion can be seen as an analytical explanation of the latitude dependent structure of the pulsation amplitudes studied by Samson. His results were simultaneously reported by Chen and Hasegawa [18].

Hughes, in his two papers [33, 34] on the effect of the magnetosphere-ionosphere-atmosphere system, showed how perturbations in the magnetosphere would be modified as they propagate through the ionosphere and down to the ground. Results of the two papers demonstrated that, given a magnetic perturbation in the y direction in the magnetosphere, the ionosphere would screen this perturbation due to the Pedersen currents induced in the ionosphere. However, a perturbation in the x direction was observable on the ground due to the simultaneous Hall currents. Hughes and Southwood [34] showed that small scale variations in the magnetosphere were severely attenuated and not observable on the ground thus limiting ground based observations to large scale dynamics only.

Walker *et al* [72] addressed the limited spatial resolution shown by Hughes and Southwood by using the Scandinavian twin auroral radar experiment (STARE) to make *in situ* observations of the dynamics inside the ionosphere. STARE was able to measure variations in the electric field in the ionosphere by measuring the Doppler velocity of the targets in the ionosphere. The experiment showed, with 20km resolution, a distinct resonance structure with the amplitudes of the pulsations. There was a peak at a certain latitude and the amplitudes fell off on either side. There was also a relative 180° phase change across the amplitude measurements.

Although the theory so far was able to explain the observables, that is, a resonant structure, little explanation could be given as to the source of the pulsation. Kivelson and Southwood [37] argued that a broadband source in the magnetosphere would not give rise to the discrete pulsations observations to date. Furthermore, there was no narrow band source specified. In an attempt to address this Kivelson and Southwood used the box model used by Southwood [58] and imposed a boundary in the y (azimuthal) direction. They showed that a global compressional mode oscillation with these boundaries would have a discrete frequency. If this frequency matched a transverse pulsation frequency then the energy would be transferred from the global compressional mode to the local transverse mode and the resonant structure would be observed.

The cavity model put forward by Kivelson and Southwood attempted to explain why pulsations were observed at discrete frequencies simultaneously at different latitudes. Ruohoniemi *et al* and Samson *et al,* [51] and [52], used the model to try to explain why pulsations were not only observed for a fixed frequency, but also why there was always a set of "magic" frequencies that was observed. These frequencies are 1.3, 1.9, 2.6 and 3.4 mHz. Samson *et al* showed that the structure created by the magnetopause turning point cavity allowed for a selection of discrete frequencies that met the condition that the phase integral between the two boundaries was constructive and thus allowed that frequency mode to exist for a significant length of time.

Wright extended this cavity model to that of a waveguide, thus removing any requirements on the boundaries in the y direction [76]. He discussed the relationship between the dispersion relation and coupling between the fast and transverse modes. He showed that if k_y was zero then there would be no coupling between the fast and the transverse modes and so no energy could be delivered to the resonance point. He showed that as k_y tended to infinity all the wave energy would propagate down the waveguide towards the flanks of the magnetosphere boundary and again there would be no energy available for the resonance. This meant that there was an intermediate k_y where there would be an optimum coupling between the modes and that there would be enough energy present to drive the pulsation.

1.2 Problem statement

The history outlined above, although brief, gives a consistent understanding of one part of pulsation research, that is, that the pulsation characteristics that are observed by the various instruments are standing plasma waves on the field lines between the northern and southern ionospheres. Furthermore, the latitudinal characteristics observed are consistent with a driven resonant system, so it follows that there must be a discrete source driving the system [81]. The nature of this source is where authors differ. These sources could be Kelvin-Helmholtz [53, 27], filtered by a magnetospheric cavity [37] or by a source inside the solar wind [59, 70].

This thesis describes how the data collected by the SuperDARN HF radar network, [30] [21], can be used to observe and characterise Pc5 pulsations. An automated pulsation finder searched through the radar data and identified pulsation events. These events were analysed to in an attempt to give an understanding of the nature of the source of the pulsations. The main advantage of the SuperDARN system is that it is able to simultaneously view large areas of the northern and southern polar regions with high temporal and spatial resolution. There are, however, limitations to the radar's ability to observe pulsations due to the fact that the radar observations are made from ground scatter and backscatter off ionospheric irregularities. If there was no scatter then there would be no observations, irrespective of the fact that there may have been pulsations occurring at that moment.

1.3 What the thesis contains

The Hermanus Magnetic Observatory (HMO) has long been conducting research in the field of geomagnetic pulsations but, until recently, this research was limited to low-latitude Pc3 as well a Pi2 pulsations [32, 62, 63]. The HMO became involved in the SuperDARN community when it agreed to take over the responsibility of the hardware maintenance of the SANAE radar as part of the then SHARE project[69]. This thesis thus serves two purposes: first, to provide an institutional reference for the use of the SuperDARN data for pulsation research and second, to report on an analysis of SuperDARN data to characterise Pc5 pulsations.

First, the derivation of the MHD equations that govern the system of interest will be discussed. In order to obtain analytic solutions certain assumptions and simplifications are made about the system. These will be discussed and their limitations noted.

Once the differential equations governing the system have been established, possible wave types will be identified as the most likely candidates for the delivery of the energy to the field lines of interest.

Once the theory of delivery of the energy has been established, the resulting structure and dynamics of standing waves in the magnetosphere will be studied. These standing waves are bounded by the ionosphere at their endpoints. The conductivity of the ionosphere plays an important role in standing wave structure and so the effects of an ionosphere with a finite conductivity will be discussed. Numerical solutions to the differential equations allow the mapping of the observations made in the ionosphere into the magnetosphere where they can be correlated with spacecraft measurements.

Since the SuperDARN radars are the primary data source, the process of radar measurement will be explained. This is important in order to highlight the possible pitfalls of using SuperDARN data for pulsation observations.

The rest of the thesis covers that analysis of the SuperDARN data and how it is used to determine pulsation characteristics.

Chapter 2

Derivation of the MHD wave equations

2.1 Introduction

There is a basic scheme that most authors apply in their use of MHD. Firstly, they derive a set of equations governing the dynamics of the electromagnetism as well as the fluid behaviour of the plasma[10]. Through assumptions of the system and simplifications they demonstrate that the differential equations that result are of the same form as the differential equation for a travelling wave. Next, using the fact that all waves can be recreated by a superposition of various sinusoids (Fourier), they use an analysis of the behaviour of this basis function to then provide an understanding of the dynamics of more complex wave mechanisms.

Use will be made of Walker's text [71] for the derivation of the wave equation. Only the significant steps for the understanding of the wave equation are mentioned here. For a more thorough discussion of the derivation the reader is referred to the text. A table of symbols can be found in appendix B.

2.2 Reduced MHD Equations

The reduced MHD equations can be listed as:

The momentum equation

$$\rho\frac{d\mathbf{v}}{dt} = -\nabla\left\{p + \frac{B^2}{2\mu_0}\right\} + \frac{\mathbf{B}}{\mu_0}.\nabla\mathbf{B} \tag{2.1}$$

states that the forces acting on a plasma will come from pressure gradients, thermal and magnetic pressure, gradients in the magnetic field and motion through the magnetic field.

The equation of continuity

$$\frac{d\rho}{dt} = -\rho\nabla \cdot \mathbf{v} \tag{2.2}$$

tells us that if the plasma density of a volume is changing with time then there must be a source or sink of velocity in that space, that is, the divergence is non-zero.

The thermodynamic nature of the plasma can be related to the rate of change of pressure by

$$\frac{dp}{dt} = -\gamma p\nabla.\mathbf{v}. \tag{2.3}$$

Finally, using a simplified version of Ohm's law and a low velocity version of the Maxwell equations the time variation of the magnetic filed is given as

$$\frac{d\mathbf{B}}{dt} = \mathbf{B}.\nabla\mathbf{v} - \mathbf{B}\nabla.\mathbf{v}. \tag{2.4}$$

2.3 Derivation of the wave equation

The wave perturbations studied here are assumed to be small amplitude perturbations. This allows the system to be linearised, that is, only first order terms are included as the higher order terms will be insignificantly small in comparison with the lower order terms. The space environment that will be studied satisfies the conditions for the use of MHD, that is, the velocities are small compared to the speed of light and that any time scales of the system must be long compared to the the gyroperiod of the heaviest ions.

The linearised first order MHD equations are given as

$$\rho_0\frac{\partial\mathbf{v}}{\partial t} = -\nabla\left\{p + \frac{\mathbf{B}.\mathbf{b}}{\mu_0}\right\} + \frac{\mathbf{B}}{\mu_0}.\nabla\mathbf{b} \tag{2.5}$$

$$\frac{\partial p}{\partial t} = -\gamma P\nabla.\mathbf{v} \tag{2.6}$$

$$\frac{\partial\mathbf{b}}{\partial t} = -\mathbf{B}\nabla.\mathbf{v} + \mathbf{B}.\nabla\mathbf{v}. \tag{2.7}$$

If (2.5) is differentiated with time and (2.6) and (2.7) used to eliminate p and B you get

$$\begin{aligned}\rho_0\frac{\partial^2\mathbf{v}}{\partial t^2} &= \nabla\left\{\left(\gamma P + \frac{B^2}{\mu_0}\right)\nabla.\mathbf{v}\right\} - \nabla\left\{\frac{\mathbf{B}}{\mu_0}.\left(\mathbf{B}.\nabla\right)\mathbf{v}\right\} \\ &\quad -\frac{1}{\mu_0}\left(\mathbf{B}.\nabla\right)\left\{\mathbf{B}\nabla.\mathbf{v} - \left(\mathbf{B}.\nabla\right)\mathbf{v}\right\}.\end{aligned}$$

If the zero order quantities do not vary in space then

$$\begin{aligned}\frac{\partial^2 \mathbf{v}}{\partial t^2} &= \left(V_A^2 + V_S^2\right) \nabla \left(\nabla . \mathbf{v}\right) - \nabla \left(\mathbf{V}_A . \nabla\right) \left(\mathbf{V}_A . \mathbf{v}\right) \\ &\quad -\mathbf{V}_A \left(\mathbf{V}_A . \nabla\right) \left(\nabla . \mathbf{v}\right) + \left(\mathbf{V}_A . \nabla\right) \left(\mathbf{V}_A . \nabla\right) \mathbf{v} \end{aligned} \tag{2.8}$$

where

$$\mathbf{V}_A = \frac{\mathbf{B}}{\sqrt{\mu_0 \rho_0}}; V_S = \sqrt{\frac{\gamma P}{\rho_0}}. \tag{2.9}$$

Equation (2.8) is the wave equation governing small amplitude velocity perturbations in a uniform magnetised plasma.

Fourier theory dictates that any arbitrary signal can be made up of a sum of sine and cosine waves of various amplitudes. It is therefore possible to get a good understanding of the dynamics of the system by analysing the response of the system to a harmonic basis variation. To that end, we will assume that the variations observed in our system are harmonic and of the form

$$A \exp\left\{\imath \left(\mathbf{k}.\mathbf{r} - \omega t\right)\right\}. \tag{2.10}$$

The operators ∇ and $\partial/\partial t$ in equation (2.8) can be replaced by $\imath\mathbf{k}$ and $-\imath\omega$ respectively so that you get

$$\left\{\omega^2 - \left(k.\mathbf{V}_A\right)^2\right\} \mathbf{v} - k \left(V_A^2 + V_S^2\right) \mathbf{k}.\mathbf{v} + \left(\mathbf{k}.\mathbf{V}_A\right) \left\{\mathbf{k} \left(\mathbf{V}_A.\mathbf{v}\right) + \mathbf{V}_A \left(\mathbf{k}.\mathbf{v}\right)\right\} = 0. \tag{2.11}$$

This can be written in component form using as

$$\begin{pmatrix} \omega^2 - k_z^2 V_A^2 - k_x^2 \left(V_A^2 + V_S^2\right) & 0 & -k_x k_z V_S^2 \\ 0 & \omega^2 - k_z^2 V_A^2 & 0 \\ -k_x k_z V_S^2 & 0 & \omega^2 - k_z^2 V_S^2 \end{pmatrix} \begin{pmatrix} v_x \\ v_y \\ v_z \end{pmatrix} = 0. \tag{2.12}$$

If this expression is transformed to wave normal aligned coordinates it becomes

$$\begin{aligned} \begin{pmatrix} \omega^2 - k^2 V_A^2 \cos^2\theta & k^2 V_A^2 \cos^2\theta \\ -k^2 V_A^2 \sin^2\theta & \omega^2 - k^2 \left(V_A^2 \cos^2\theta + V_S^2\right) \end{pmatrix} \begin{pmatrix} v_T \\ v_L \end{pmatrix} &= 0 \\ \left(\omega^2 - k^2 \cos^2\theta\right) v_y &= 0 \end{aligned}. \tag{2.13}$$

A non-trivial solution for this system of equations is obtained if the determinant of the coefficient matrix is set equal to zero giving the dispersion relations

	$\theta = 0°$	$\theta = 90°$
Alfvén	$v_p = V_A$	0
Magnetosonic	$v_p = V_A$ or V_S	0 or $v_p = \sqrt{V_A^2 + V_S^2}$

Table 2.1: Limiting cases for Alfvén and magnetosonic phase velocity.

$$\begin{aligned} \omega^2 - k^2 V_A^2 \cos^2\theta &= 0 \\ \omega^4 - k^2\left\{V_A^2 + V_S^2\right\}\omega^2 + k^4 V_A^2 V_S^2 \cos^2\theta &= 0 \end{aligned} . \tag{2.14}$$

The form of the second equation in (2.14) is a quadratic in ω^2 which will yield the familiar two root solution. Furthermore, if the equations are divided by k^2 and k^4 respectively they yield

$$\begin{aligned} v_p^2 &= V_A^2 \cos^2\theta \\ v_p^2 &= \tfrac{1}{2}\left\{\left(V_A^2 + V_S^2\right) \pm \sqrt{\left(V_A^2 + V_S^2\right)^2 - 4V_A^2 V_S^2 \cos^2\theta}\right\} \end{aligned} \tag{2.15}$$

which are the equations governing the phase velocity of the various waves permitted by (2.8).

There are three types of waves permitted by this set of dispersion relations. The first is derived from the first equation in (2.15) and is called the transverse Alfvén wave. The next two come from the positive and negative solutions of the quadratic equation. They are called the fast and slow magnetospheric waves respectively.

Table 2.1 shows the limiting cases for situations where the wave is either travelling parallel to the ambient magnetic field ($\theta = 0°$) or travelling perpendicular ($\theta = 90°$) to the field.

2.4 Applicability

This chapter outlines the basic theory of how perturbations will propagate in a uniform magnetised plasma. The origin of Pc5 pulsations is the topic of much debate, but no matter what the source, the energy must propagate through the magnetosphere as one of the plasma waves given in table 2.1 and so any Pc5 band perturbation that is observed by the radar can be thought of, in its very simple form, as one of the waves described in this chapter.

2.5 Summary

Magnetohydrodynamic and small amplitude approximations were made of the differential equations describing a uniform magnetised plasma. These simplifications yielded a differential equation in the velocity perturbation parameter $\mathbf{v}$ in both space and time. This

differential equation is of the same form as that for a travelling wave indicating that the perturbation will propagate through the medium as a plasma wave. Two main waves were found to exist, namely the magnetosonic and the Alfvén waves. Magnetosonic waves can travel isotropically, while Alfvén waves are constrained to propagate along a field line. Although too simplistic to be of any quantitative use in studies of pulsations observed with SuperDARN radars, this chapter gives a basic qualitative view of the types of waves that may give rise to the observations.

Chapter 3

MHD waves in the magnetosphere

3.1 Introduction

In the previous chapter the kinds of waves that will propagate in a homogeneous medium were established. Next a modelled magnetosphere that is not homogeneous will be studied. This chapter begins with a discussion of a model for the magnetosphere and how this differs from the homogeneous system discussed before. It will be noted that as the perturbations propagate through the magnetosphere they encounter two regions of interest, namely the turning point and the resonance point. At the resonance point our model fails as some of the parameters describing the perturbation become singular. The behaviour at this point is the subject of the next chapter (chapter 4). The current chapter focuses of how wave energy can propagate through the magnetosphere.

3.2 The magnetosphere

The magnetosphere can be thought of that region of our near space environment where the earth's main field dominates. The layer that separates the interplanetary medium from the magnetosphere is called the magnetosheath. This is where the magnetic pressure from the main field balances with the solar wind plasma pressure. Figure 3.1 shows a cartoon of the magnetosphere. The dipolar nature of the closed filed lines of the main field can be seen. A field line is termed closed if it forms a closed loop inside the magnetosphere. An open field line is one that, although it passes through the earth, is connected directly to the interplanetary magnetic field through magnetic reconnection. In order to model the behaviour of the magnetosphere many authors, starting with Southwood [58], have made use of the box model. An extremely simplified version of this model is to assume that instead of curved field lines, as you would expect in a dipolar field, the field lines are straight and are in the z direction and that the magnetic field strength is constant through-out the box. The boundaries for the box are infinite in every direction. In

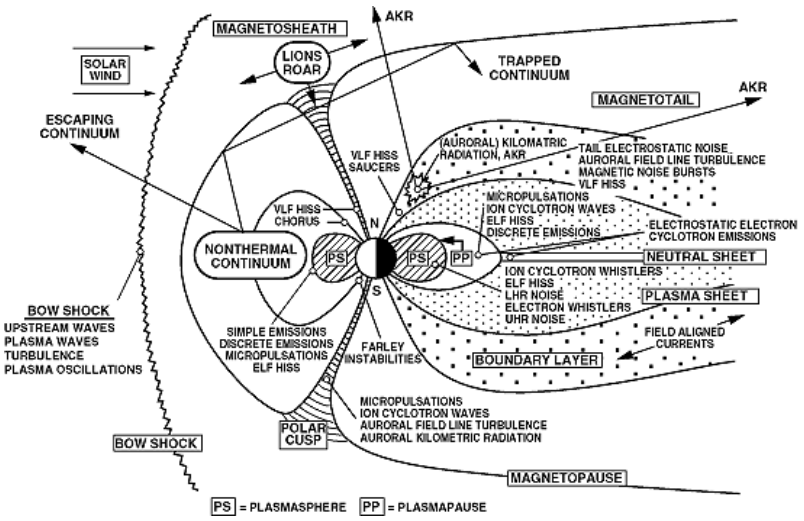

Figure 3.1: A cartoon of the magnetosphere showing the various regions of interest as well as the typical waves that are found in that region [29].

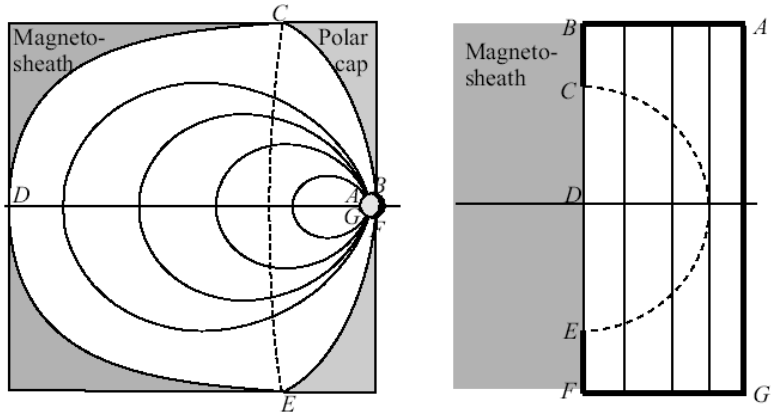

Figure 3.2: A meridional slice through a box model of the magnetosphere [71]. The locations in the magnetosphere A-G are indicated in the box model.

this model perturbations are governed by equation (2.8). A more realistic model, shown in figure 3.2, would introduce finite boundaries in x and z and introduce some spatial dependence for the magnetic field and plasma parameters. Taking our cue from the actual magnetosphere and for Cartesian simplicity, we will orient our model such that the $x-y$ plane is in the equatorial ecliptic, with x directed into the magnetosphere, y directed west and z directed north. Boundaries in the x direction are the magnetosheath (B-C-D-E-F in figure 3.2) at some negative x and the equatorial ionosphere (A-G) in the positive x direction. The z direction also has a boundary at some negative z (G-F) and positive z (A-B), but the distance between the boundaries is the length of the field line between the northern and southern ionospheres. There are no fixed boundaries in the y direction. Use will be made of straight field lines but will be using a fictitiously high magnetic gradient in the x direction to compensate for the lack of curvature in the field lines. Similarly, to recreate plasma conditions gradients in plasma pressure and density in the x direction

only will be introduced.

3.3 The MHD equations for the magnetosphere

As has been established, perturbations in a homogeneous medium will lead to the waves described in section 2.3, namely the fast and slow magnetosonic waves and the transverse Alfvén waves. The magnetosphere described above is not homogeneous, but allows for variations in the x direction. $\mathbf{B}$, P and ρ_0 will vary with x. The variation is unknown at this point and so the differential equations describing the plasma perturbations that will hold for these variations in x will be derived. As our magnetosphere is partly homogeneous, we have already derived the way the parameters will vary in y, z and t, namely they will vary as

$$\exp\{-\imath\omega t + \imath k_y y + \imath k_z z\}. \tag{3.1}$$

This means that in the differential equations we can substitute $\partial/\partial t$ with $-\imath\omega$, $\partial/\partial y$ with $\imath k$ and $\partial/\partial z$ with ik_z .

Three new variables that describe the plasma are now introduced, namely the normal displacement ξ , the component of the displacement perpendicular to $\hat{x}$ and $\mathbf{B}$, η , and the generalised pressure $\psi \equiv p + \mathbf{B}.\mathbf{b}/\mu_0$. The two displacement variables ξ and η are in the $\hat{x}$ and $\hat{y}$ directions respectively, these directions are associated with poloidal (in the direction of the poles) and toroidal (in the direction perpendicular to the poles) directions in the magnetosphere. The displacements are related to the velocity perturbations by

$$v_x = -\imath\omega\xi \tag{3.2}$$

$$v_y = -\imath\omega\eta. \tag{3.3}$$

After linearising the MHD equations (2.5), (2.6) and (2.7) again, this time taking note of the spatial variation in x, and after some algebra this gives

$$\frac{d\psi}{dx} = F(x)\xi \tag{3.4}$$

$$\frac{d\xi}{dx} = -\frac{G(x)}{F(x)}\psi, \tag{3.5}$$

where

$$F(x) = \rho_0[\omega^2 - (\mathbf{k}.\mathbf{V}_A)^2] \tag{3.6}$$

$$G(x) = \frac{\omega^4}{\omega^2(V_A^2 + V_S^2) - (\mathbf{k}.\mathbf{V}_A)^2 V_S^2} - k_y^2 - k_z^2. \tag{3.7}$$

The equation governing the perturbation displacement η is given by

$$\eta = i\frac{k_y \psi}{\rho_0(\omega^2 - (\mathbf{k}.\mathbf{V}_A)^2)}, \tag{3.8}$$

where k_y is the component of $\mathbf{k}$ in the direction of η.

ξ or ψ may be eliminated from (3.4) or (3.5) giving

$$\frac{d^2\xi}{dx^2} + \frac{(F/G)'}{F/G}\frac{d\xi}{dx} + G\xi = 0 \tag{3.9}$$

$$\frac{d^2\psi}{dx^2} - \frac{F'}{F}\frac{d\psi}{dx} + G\psi = 0. \tag{3.10}$$

Inside the magnetosphere the generalised pressure ψ is dominated by the magnetic pressure. This means that the Alfvén velocity dominates over the magnetosonic velocity and if we assume that the magnetic field is constant in the z direction, but dependent on x, (3.6) and (3.7) simplify to become

$$F(x) = \rho_0(\omega^2 - k_z^2 V_A^2) \tag{3.11}$$

$$G(x) = \frac{\omega^2}{V_A^2} - k_y^2 - k_z^2. \tag{3.12}$$

Equation (3.9) can be solved numerically, observing how the displacement ξ varies with x. What is of more importance is to ask what happens at the poles and zeros of (3.9).

3.4 Singularities in the magnetosphere

The poles and zeros of (3.9) are controlled by the zeros of (3.11) and (3.12), i.e. when

$$\omega^2 = k_z^2 V_A^2 \text{ and } \frac{\omega^2}{V_A^2} = k_y^2 + k_z^2. \tag{3.13}$$

The first equation in 3.13 gives the values of ω for a zero in F and the second equation gives the values of ω for a zero in G.

Before looking at the accurate behaviour of the perturbed parameters at the singularities, the overall behaviour will be studied.

3.4.1 The turning point

In order to determine how the energy propagates, consider the phase behaviour of the perturbed parameters by using the phase integral method. In our discussion the magnetosphere has been approximated to be uniform in y and z, but with a variation in parameters in x. If the variation in x is slow, then one can assume that for a small slab with thickness dx, the parameters are constant. The phase relationship for this slab will then be $\mathbf{k}.dx$. As the slab is uniform one can use (2.14) so the dispersion relation is $\omega^2 - k^2 V_A^2 = 0$ and in the x direction

$$k_x^2(x) = \frac{\omega^2}{V_A^2(x)} - k_y^2 - k_z^2, \tag{3.14}$$

where V_A is monotonically increasing with x. The total phase of a perturbation propagating from 0 to x is represented by

$$\pm \imath \int_0^x k_x(x) dx. \tag{3.15}$$

At the point where $G = 0$ the second of the equations in (3.13) determines that $k_x = 0$. For x smaller than this point, k_x is real and the wave propagates. For x greater than this point, k_x becomes imaginary and so that wave cannot propagate. This point, the turning point for the wave, is denoted by a subscript T (x_T).

3.4.2 The resonance point

In (3.13), when $F = 0$ then $\omega^2 = k_Z^2 V_A^2$. It will be shown later that this is the condition for standing transverse Alfvén waves on a magnetic field line bounded by the ionosphere at either end. This point, the resonance point for the wave, is denoted by a subscript R (x_R).

3.5 Away from the singular points

The phase integral method is useful to determine the direction of the propagation of the perturbations, but is not useful for determining the amount of energy that is propagated as it ignores the amplitude of the perturbation. To determine the amount of energy the WKBJ solutions of equation (3.10) are used. It is rewritten

$$\psi'' - \frac{F'}{F}\psi' + k^2 q^2(x)\psi = 0, \tag{3.16}$$

where $k^2 q^2(x) = G(x)$ with k a constant and q a dimensionless function that depends on x. Using a WKBJ method this then gives

$$\psi_{\pm}(x) = \left(\frac{F(x)}{q(x)}\right)^{1/2} \exp\left\{\pm \imath k \int^{x} q(x)dx\right\}. \tag{3.17}$$

This approximate solution breaks down when $G \to 0$ and $F \to 0$. To understand what happens at these points their behaviour near the points needs to be studied.

3.6 Near the turning point

Near $G = 0$, i.e. $x = x_T$, we can expand G and F to first order in $|x - x_T|$ to get

$$G = G'_T(x - x_T) + O[(x - x_T)^2] \tag{3.18}$$

$$F = F_T + O(x - x_T). \tag{3.19}$$

Equations (3.9) and (3.10) become

$$\frac{d^2\psi}{dx^2} + G'_T(x - x_T)\psi = 0 \tag{3.20}$$

$$\frac{d^2\xi}{dx^2} - \frac{1}{x - x_T}\frac{d\xi}{dx} + G'_T(x - x_T)\xi = 0. \tag{3.21}$$

If we let $\varsigma = -\left(|G'_T(x_T)|\right)^{1/3}(x - x_T)$ then

$$\frac{d^2\psi}{d\varsigma^2} = \varsigma\psi \tag{3.22}$$

$$\frac{d^2\xi}{d\varsigma^2} - \frac{1}{\varsigma}\frac{d\xi}{d\varsigma} - \varsigma\xi = 0. \tag{3.23}$$

Equation (3.22) is of the form known as a Stokes's equation. It has a general solution

$$\psi = A\mathrm{Ai}(\varsigma) + B\mathrm{Bi}(\varsigma), \tag{3.24}$$

where Ai and Bi are the special functions called Airy functions. For $\varsigma < 0$ (i.e. $x < x_T$) both Ai and Bi exhibit oscillatory behaviour. For $\varsigma > 0$ Bi $\to \infty$ and Ai $\to 0$ as $\varsigma \to \infty$. Thus the coefficient of Bi must be 0, otherwise ψ becomes infinite as $\varsigma \to \infty$.

3.7 Near the resonance point

Similarly, near $F = 0$, i.e. $x = x_R$, if we make the substitution $\zeta = k_y(x - x_R)$ then

$$\frac{d^2\xi}{d\zeta^2} - \frac{1}{\zeta}\frac{d\xi}{d\zeta} - \xi = 0 \tag{3.25}$$

$$\frac{d^2\psi}{d\zeta^2} - \frac{1}{\zeta}\frac{d\psi}{d\zeta} - \psi = 0. \tag{3.26}$$

Equation (3.25) is of the form known as a modified Bessel equation of order zero with solutions $I_0(\zeta)$ and $K_0(\zeta)$. Again we have that $I_0(\zeta) \to \infty$ as $\zeta \to \infty$ whereas $K_0(\zeta) \to 0$ as $\zeta \to \infty$, indicating that, given the magnetospheric boundaries, the solution will be $K_0(\zeta)$. The series solutions for I_0 and K_0 are

$$I_0(\zeta) = 1 + \frac{1}{4}\zeta^2 + \cdots$$

$$K_0(\zeta) = -[\ln\frac{1}{2}\zeta + \gamma]I_0(\zeta) + \frac{1}{4}\zeta^2 + \cdots .$$

So as $\zeta \to 0$ we get $K_0 \to \infty$ which would mean that $\xi \to \infty$. At the resonance the RHS of equation (3.4) will be equal to zero, so $d\psi/dx = 0$, indicating that ψ is a constant. However, equation (3.8) will also be singular as the denominator equals zero. These two singularities (i.e. that $\xi \to \infty$ and $\eta \to \infty$) indicate that there is a loss mechanism missing from our consideration of the system. A possible loss mechanism is the subject of the next chapter.

3.8 Applicability

Why is this chapter applicable to the study of Pc5 pulsations with the radar?

The radar observes the the points at which the earth's magnetic field lines pass through the ionosphere in the polar regions. The observations of the radar and an understanding of how the energy propagates through the magnetosphere allows one to study magnetospheric dynamics [75].

3.9 Summary

In our box model of the magnetosphere a perturbation in either the magnetic or plasma parameters near the magnetosheath will give rise to a fast magnetosonic wave that will propagate at the Alfvén velocity equally in all directions. This is known as the isotropic Alfvén wave. Due to the gradient in the x direction, the Alfvén velocity will increase as the wave moves deeper into the magnetosphere. We can assume that k_z will be constant due to the box nature of our model and that k_y is an undetermined non-zero value at

this time. When using the WKBJ solutions (see phase part of equation 3.17), there is some point in the x direction (which we have denoted x_T) where the wave number in the x direction equals zero. At this point the behaviour of the perturbation is approximated by the Airy function Ai. To the left of this point the perturbation is still oscillatory and indicates that the wave has been reflected. There is, however, still some evanescent penetration to the right of the point as the amplitude of the perturbation falls as it moves deeper into the magnetosphere. If conditions are such that the turning point lies outside the magnetopause then the only propagation of the perturbation in the magnetosphere is as an evanescent wave. The second point of interest in the x direction (which we have denoted as x_R) is where the equations describing the perturbations, i.e. the solution to the Bessel equation of order zero become infinite. Here the differential equations indicate that both the displacements, ξ and η, are infinite and the generalised pressure, ψ, is constant. This is a non-realistic situation and indicates that the description of the system so far has neglected some loss mechanism. The generally accepted loss mechanism is joule heating in the ionosphere as a transverse Alfvén wave is reflected at the ionosphere and sets up standing waves on field line. This is the topic of the next section. In order for the energy from the initial perturbation near the magnetosheath to reach this resonance point x_R the resonance point must be sufficiently near the turning point x_T so that the amplitude of the perturbation has not decayed away. The separation of these two points is governed by the wave number in the y direction k_y. If $k_y = 0$ in equation 3.13, the two points are collocated and one would expect that the influence would be maximum, because the amplitude of the perturbation has not begun to decay. The amplitude is at a maximum, but, from equation (3.8) we see that the coupling between the compressional part, ξ and ψ, is governed by k_y. If $k_y = 0$ there is no coupling. At the same time if $k_y$is too large, there will be too great a separation between x_T and x_R and there will be no energy available for the coupling. An intermediate value of k_y is thus necessary for the energy from the initial perturbation to penetrate past the turning point, begin to decay, and still set a field line into resonance.

Chapter 4

Field line standing waves

4.1 Introduction

The theory outlined in chapter 3 showed how a perturbation that occurs near the magnetosheath can propagate through the magnetosphere and eventually deliver energy to that point in the x direction where $\omega^2 = k_z^2 V_A^2$. Near this point the differential equations governing the system become singular. This chapter discusses this point in the magnetosphere in more detail. It will be seen that there is indeed coupling between the compressional mode wave that was propagating through the magnetosphere and a transverse mode Alfvén wave as indicated in equation (3.8). The transverse mode Alfvén wave will propagate along the closed field line and be reflected by the ionosphere through which the magnetic field line passes and will set up a standing wave between the two ionospheres. As a first approximation we will assume that the ionosphere is infinitely conducting. A discussion will outline how a finite ionosphere is vital for observing these pulsations on the ground with a magnetometer and with the radar. Furthermore, the finite ionosphere provides a loss mechanism through joule losses and thus prevents the singularity from occurring.

4.2 Description of the standing wave perturbations

Our box model has two conducting planes in the $x-y$ plane at some positive and negative z. So far we have not discussed the nature of our perturbation in the z direction, save to say that it will be governed by the boundaries in the z direction. Also mentioned was that perturbed plasma will be displaced in the x and y direction which we have represented by ξ and η respectively. The discussion has been limited to the displacement perturbations until now as it is possible to use equations (2.5), (2.6) and (2.7) to determine the other parameters. If one looks at equation (2.7) then solving for the the x and y components you get

$$b_x = -\frac{k_z B}{\omega} v_x \tag{4.1}$$

$$b_y = -\frac{k_z B}{\omega} v_y. \tag{4.2}$$

If we assume for the moment that the boundaries are infinitely conducting then the **E** field at the boundary must be zero. We also have

$$\mathbf{v} = \frac{\mathbf{E} \times \mathbf{B}}{B^2}, \tag{4.3}$$

so that any velocity perturbation at the boundary in the plane of the boundary must also be zero.

Spatial variation of the perturbations in the z direction are governed by $\exp\{\pm \imath k_z z\}$, where the $\pm$ is determined by the direction of the propagation of the perturbation. The box nature of our model means that there is a discontinuity in the z direction at the boundaries so that the perturbations in the z direction will not be propagated waves, but rather a superposition of forward and reflected waves. The spatial variation of the perturbations in the z direction are now varying as

$$\exp\{\imath k_z z\} + \exp\{-\imath k_z z\} = 2 \cos k_z z. \tag{4.4}$$

Also from (4.1) and (4.2) we see that for propagating waves $b_{x,y} \propto k_z v_{x,y}$, so if (4.4) is for the velocity perturbation then for the magnetic perturbation

$$b = b_{forward} + b_{backward} = k_z \exp\{\imath k_z z\} - k_z \exp\{-\imath k_z z\} = 2\imath k_z \sin k_z z,$$

where the minus sign is from the fact that the backward propagating magnetic perturbation is proportional to k_z which will be negative for the backward propagating wave.

If the velocity perturbations and the electric field perturbations vary as $\cos k_z z$ then there will be nodes at some positive and negative value of z where $k_z z = \pm\pi/2$. A perfectly conducting sheet could be inserted at this point without changing the behaviour of the system. Equation (4.3) shows that the velocity perturbation will be zero at the ionosphere so the points $\pm d$ are a suitable location for the boundaries in the z direction where $k_z(\pm d) = \pm\pi/2$.

The resulting standing wave velocity and magnetic field perturbations can be seen in figure 4.1 where the perturbations on the left show the nodes at the ionosphere and the ones on the right show the anti-nodes at the ionosphere. The higher order standing waves are also shown.

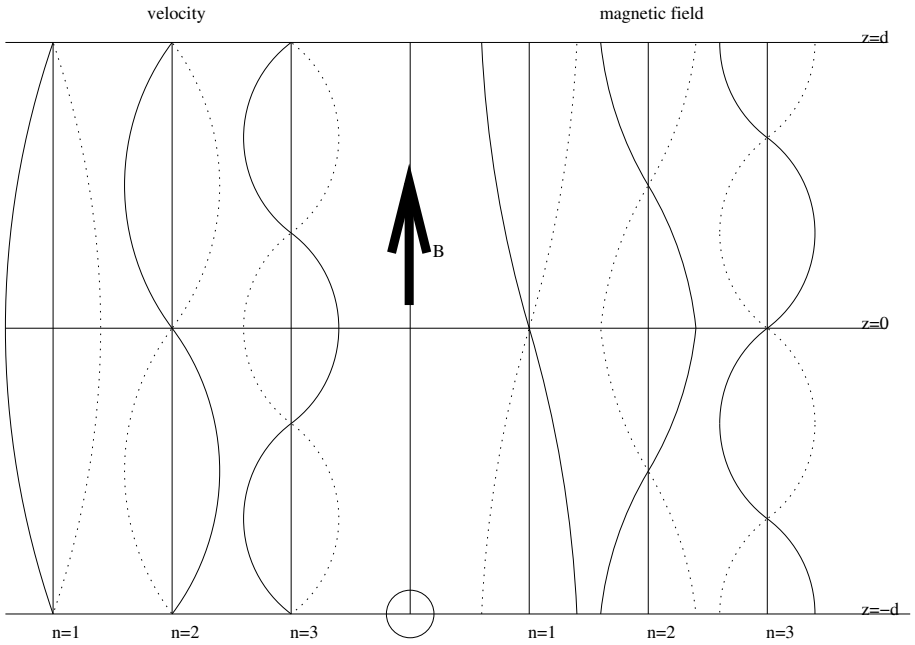

Figure 4.1: Standing waves in the box model, after Walker[71]. The perturbations on the left are velocity, or **E** field, and the perturbations on the right are the magnetic field perturbations.

4.3 Ionospheric conductivity

4.3.1 Conductivity

So far we have assumed an infinitely conducting ionosphere. The ionosphere can be better thought of as a thin transition region between the collisionless plasma of the magnetosphere and the nearly neutral atmosphere [71].

4.3.2 Ideal plasma (collisionless)

An ideal plasma void of a magnetic field will be an infinitely conducting medium. If it is permeated by a magnetic field, then the situation changes and the relationship between the gyro-frequency and the collision frequency is such that $\Omega_e \gg \nu_e$ and $\Omega_i \gg \nu_i$, where $\Omega_{e,i}$ represents the gyro frequency of the electrons and ions and $\nu_{e,i}$ represents the collision frequency of the electrons and ions. In such a medium, the charge carriers are restricted to movement in the direction of the magnetic field only as they are tied to the field via the frozen-in-flux condition and so cannot move perpendicular to the field. One would expect to find this situation above the ionosphere where the neutral population is rare.

4.3.3 Isotropic conductivity

The opposite situation would be where $\Omega_e \ll \nu_e$ and $\Omega_i \ll \nu_i$. Now, instead of the charge carriers being free to move around the field line as they gyrate, they collide with the

neutrals before that can complete a part of the gyro-radius. The motion of the charged particles will now be in the direction of force from an applied electric field such that

$$\mathbf{J} = \sigma \mathbf{E},$$

where $\mathbf{J}$ is the current density, σ is the conductivity and $\mathbf{E}$ is the applied electric field. One would expect to find this situation in a medium consisting of a neutral gas and a plasma, such as at the bottom of the ionosphere.

4.3.4 Anisotropic conductivity

For the situation between these two conditions, where the one population of the plasma is free to move under the influence of an applied electric field and the other is still constrained along the magnetic field, we get a condition of anisotropic conductivity. In the E-region of the ionosphere the heavy ions will collide regularly with the neutrals giving us $\Omega_i \ll \nu_i$. The electrons on the other hand are still able to gyrate, so $\Omega_e \gg \nu_e$. Below the E-region the neutral density increases meaning that now $\Omega_e \ll \nu_e$ and the system will behave with isotropic conductivity. Above the E-region the neutral density decreases so that you get $\Omega_i \gg \nu_i$ and the system behaves like an ideal plasma.

Inside the E-region the conductivity along the field line remains unchanged. If we align the ionosphere such that it is in the $x-y$ plane and that the magnetic field is perpendicular to the plane in the z direction then an applied electric field will give rise to a current density in the $x - y$ plane supported by

$$\begin{matrix} J_x \\ J_y \end{matrix} = \begin{pmatrix} \sigma_P & \sigma_H \\ -\sigma_H & \sigma_P \end{pmatrix} \begin{pmatrix} E_x \\ E_y \end{pmatrix}, \tag{4.5}$$

where J is the current density, E is the applied electric field and σ_P and σ_H are the Pedersen and Hall conductivities respectively.

In a system where we assume that the conductivity along a field line is infinite

$$\sigma_P = \frac{N_i q^2}{m_i \nu_i} \tag{4.6}$$

$$\sigma_H = \frac{Ne}{B}. \tag{4.7}$$

Equation (4.5) shows that if there is an applied electric field in one direction, there will be a current flowing that direction governed by the Pedersen conductivity, and there will also be a current perpendicular to the applied electric field governed by the Hall conductivity.

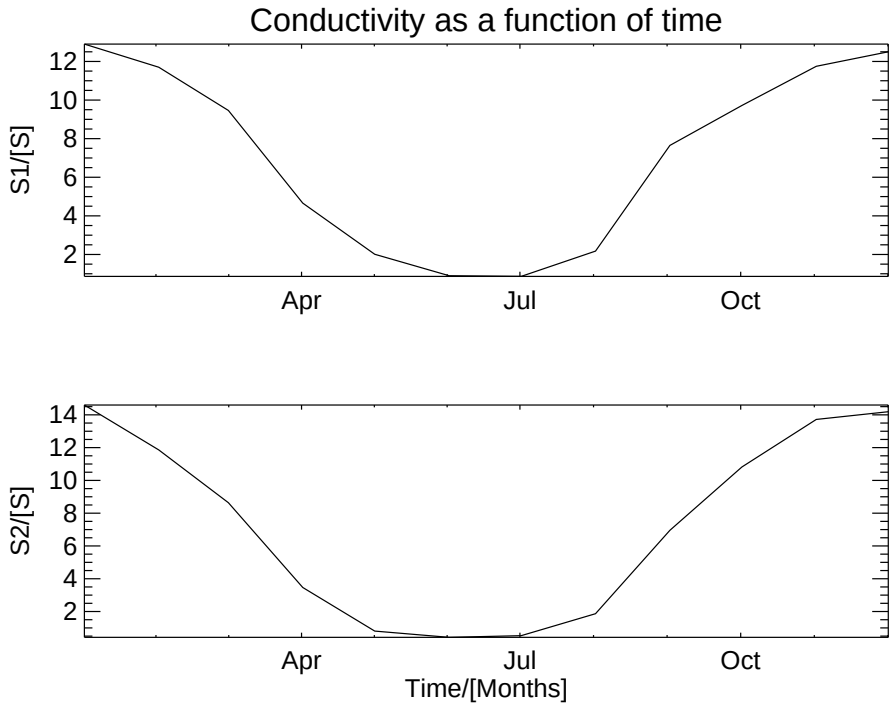

Figure 4.2: The variation of Pedersen (S1) and Hall (S2) conductivity during 2002 for SANAE.

4.3.5 Conductivity variability

The actual current that will flow in the ionosphere is the height integration of the current density of equation (4.5). If we assume that the ionospheric thickness is thin where the current is flowing, then we can say that the electric field is constant with z in this region.

$$\begin{pmatrix} I_x \\ I_y \end{pmatrix} = \int_{z_1}^{z_2} \begin{pmatrix} J_x \\ j_y \end{pmatrix} dz = \int_{z_1}^{z_2} \begin{pmatrix} \sigma_P & \sigma_H \\ H & \sigma_P \end{pmatrix} dz \begin{pmatrix} E_x \\ E_y \end{pmatrix} = \begin{pmatrix} \Sigma_P & \Sigma_H \\ -\Sigma_H & \Sigma_P \end{pmatrix} \begin{pmatrix} E_x \\ E_y \end{pmatrix},$$

where Σ_P and Σ_H are the height integrated Pedersen and Hall conductivities respectively. In order to calculate Σ_P and Σ_H for a specific location one needs to know the constituents of the atmosphere at that time and place. Use was made of the on-line ionospheric conductivity model hosted by World Data Centre for Geomagnetism, Kyoto [3]. This model makes use of IRI90 for the ionised atmosphere and CIRA72 for the neutrals. The height integrated conductivity during 2002 for SANAE (71°40′S 2°51′W geographic) is shown in figure 4.2. One can see that this variability follows a seasonal pattern with the maximum conductivity in the summer and the minimum in the winter. This confirms that the conductivity is solar driven with more ionospheric ionisation in the summer and hence more

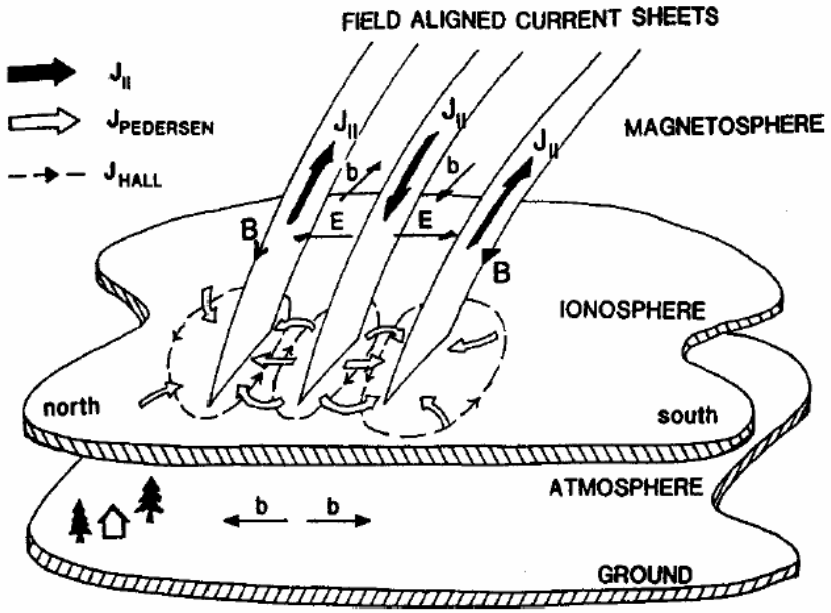

Figure 4.3: The ends of a perturbed magnetic field line in the ionosphere. The Pedersen currents are shown connecting the field aligned currents while the Hall currents form closed loops around the ends of a field line. (From McPherron [42]).

conductivity and less ionisation in the winter hence lower conductivity. This follows from equations (4.6) and (4.7) which show that the conductivities are dependant on the number of charged particles.

4.4 Ionospheric losses

At the end of chapter 3 our description of the perturbations in the magnetosphere broke down as there is a singularity in the equations describing the displacements ξ and η. It was noted that this is due to the fact that there is a yet to be considered loss in the ionosphere.

4.4.1 Closing of the perturbations in the ionosphere

If we view the ends of a perturbed magnetic field line in the ionosphere as in figure 4.3, the magnetic perturbation is in the east-west direction. Equation (4.2) shows b_y and v_y are proportional, and from equation 4.3, $E_x = -v_y B$ so that the electric field perturbations will be in the north-south direction. We have already established that plasma is free to move along the field line. At the bottom of the ionosphere in the E-region the Pedersen conductivity allows current to flow perpendicular to the main field. The changing magnetic field $\mathbf{b}$ causes a current to flow along the field lines, through the ionosphere in the form of a Pedersen current and couple with an adjacent field line to complete the circuit.

The Pedersen current I_x will in turn generate a varying magnetic field b_y^+ and b_y^-, where b^+ is the field above the surface and b^- is the field below the surface. The field line perturbation below the ionosphere can be written as b_y. This perturbation will be cancelled by the Pedersen current perturbation, thus shielding the initial perturbation from the ground. There is however, a secondary current I_y that will flow perpendicular to the Pedersen current which results from the Hall conductivity. Similar to the Pedersen current, the Hall current will create a varying magnetic perturbation above and below the ionosphere as b_x^+ and $-b_x^-$ which are perpendicular to the field line perturbation. This is the perturbation that is observed on the ground and is at right angles to the initial field line perturbation.

4.4.2 Finite Pedersen conductivity

Inside the ionosphere

$$\widehat{\mathbf{z}} \times \mathbf{b} = \pm\mu_0 \mathbf{j}.$$

As the field line current closes with the Pedersen current

$$\pm\mu_0 \mathbf{j} = \pm\mu_0 \Sigma_P \mathbf{E},$$

where Σ_P is the height integrated Pedersen conductivity in the ionosphere so that

$$\mu_0 \Sigma_P E_x = b_y. \tag{4.8}$$

It has already been determined that the velocity and electric field perturbations vary spatially as $\cos k_z z$, so

$$E_x = C \cos\{(k_r + \imath k_i) z\}$$

and it follows that

$$-\imath\omega b_y = C(k_r + \imath k) \sin\{(k_r + \imath k_i) z\},$$

where k_i is a small imaginary part that we have added to the wave vector to account for the losses. The inclusion of k_i means that the electric field E_x now follows a cosine of a sum behaviour ($\cos(a+b) = \cos a \cos b - \sin a \sin b$) and b_y follows a sine of a sum behaviour ($\sin(a+b) = \sin a \cos b + \cos a \sin b$). As $\cos k_r z = 0$ and $\sin k_r z = 1$ at the ionosphere ($z = d/2$)

$$E_x \approx C \sin \imath k_i \frac{d}{2} \tag{4.9}$$

and

$$-\imath\omega b_y \approx C(k_r + \imath k_i)\cos \imath k_i \frac{d}{2}.$$

Using 4.8 in the ionosphere it follows that

$$-\frac{\imath}{\omega}(k_r + \imath k_i)\cos\{(\imath k_i)d/2\} = \mu_0 \Sigma_P \sin\{(\imath k_i)d/2\}.$$

We already have that $k_r = \frac{\pi}{d}$ and with $k_r \gg k_i$ we get that

$$k_i = \frac{2\pi}{\omega \mu_0 \Sigma_P d^2} \tag{4.10}$$

The losses in the ionosphere are then governed by the height integrated Pedersen conductivity. For infinite Pedersen conductivity k_i would be zero and the system would respond in a singular manner as described in chapter 3. With $k_i \neq 0$ the energy that is carried to the resonance point, x_R, in the magnetosphere can be dissipated through resistive losses in the finitely conductive ionosphere. Another consequence of the finite Pedersen conductivity is that, if $k_i = 0$, then according to equation (4.9) E_x would be zero in the ionosphere. The motion that is observed by the HF SuperDARN radars is $\mathbf{E} \times \mathbf{B}$ drift and so with zero **E**-field perturbations, there would be zero drift perturbations. Thus the radar would be useless for observing pulsations.

4.5 Ionospheric filtering

Below the ionosphere the plasma density is negligible and the magnetic perturbation caused by the Hall current will propagate away from the ionosphere with its associated electric field as an electromagnetic wave. The dispersion relation for electromagnetic wave travelling below the ionosphere is

$$\frac{\omega^2}{c^2} = k_x^2 + k_y^2 + k_z^2$$

For Pc5 pulsations $\omega \ll c$ so below the ionosphere

$$k_z \approx \pm\imath\sqrt{k_x^2 + k_y^2},$$

meaning that the wave will be evanescent in the z direction and will decay as a factor of $\sqrt{k_x^2 + k_y^2}$. This means that a higher spatial frequency in x and y will result in a higher attenuation of the signal. This acts as a low pass filter and is why ground based magnetometer chains cannot resolve high spatial variability [34].

4.6 Applicability

The SuperDARN radars observe, *inter alia*, the motion of ionospheric irregularities that are associated with $\mathbf{E} \times \mathbf{B}$ drifts. This chapter demonstrates that with an infinite Pedersen conductivity in the ionosphere there will be no ionospheric electric fields and as a consequence there will be no $\mathbf{E} \times \mathbf{B}$ drift. If there is a finite Pedersen conductivity, then the associated second order electric field will cause a drift that is measurable by the radar. From the plots in figure 4.2 we can also see that there is a greater chance of observing pulsations in winter than in summer. According to equation 4.10 it follows that the higher the Pedersen conductivity, the smaller k_i and from equation 4.9 as $k_i \to 0$ we get $\sin k_i z \to 0$ and $E_x \to 0$.

The fact that the Pedersen current screens the pulsation from the ground means that magnetometers rely on the Hall current to observe pulsations. The Hall current is proportional to the Hall conductivity, and as the conductivity falls in winter one would expect the observations made by magnetometers to be affected. In section 4.5 it was noted that below the ionosphere higher spatial variations in the ionosphere are filtered from the ground. This means that magnetometers are best suited for observing pulsations with low-m, while the radars which do not suffer from this filtering are able to observe pulsations with high-m.

It follows then that magnetometer and radar observations pulsations are complementary: the magnetometer performs better in summer, while the radar better in winter.

4.7 Summary

There is a point in the magnetosphere where $\omega^2 = k_z^2 V_A^2$, and if there is coupling between the compressional component and the transverse component, travelling Alfvén waves will propagate along the field line. The field line passes through the ionosphere where the conductivity characteristics of the medium change. If the ionosphere conducts perfectly, then all the incident energy in the propagating Alfvén wave will be reflected and the result is a standing wave pattern with nodes of electric field strength at the ionosphere and antinodes in the equatorial plane. This situation matches what was described at the end of the previous chapter, where as energy is constantly being transferred to the Alfvén wave, the solution will grow to a singularity.

If we introduce a finite conductivity, then not all the energy is reflected and we have the loss mechanism to counteract the singularity. It is the height integrated Pedersen conductivity that determines the losses in the ionosphere.

Chapter 5

Numerical solutions

5.1 Introduction

The discussion in the previous chapters focused around a Cartesian co-ordinate system in order to find analytical solutions that might give a hint as to the actual dynamics in the magnetosphere.

In this chapter the problem will be approached in terms of the dipole coordinate system with variables ν, μ and ϕ. This is a more accurate description of the magnetosphere, but leads to differential equations that do not have simple analytical solutions. These equations will be solved using numerical methods the results of which will prove to be not too far from the analytical solutions reached in the previous chapters.

5.2 The dipole co-ordinate system

A first approximation of the earth's magnetic field can be modelled using a dipolar field such as in figure 5.1. An orthogonal curvilinear coordinate system is used to describe the field. The choice of this system enables one to transform the curvilinear variables into Cartesian coordinates by multiplying them with the suitable scale factors. The curvilinear coordinates can be related to the more recognisable spherical polar coordinates through the following relationships

$$\mu = \frac{a^2 \sin\lambda}{r^2}$$

$$\nu = \frac{a}{r}\cos^2\lambda$$

$$\phi = \phi,$$

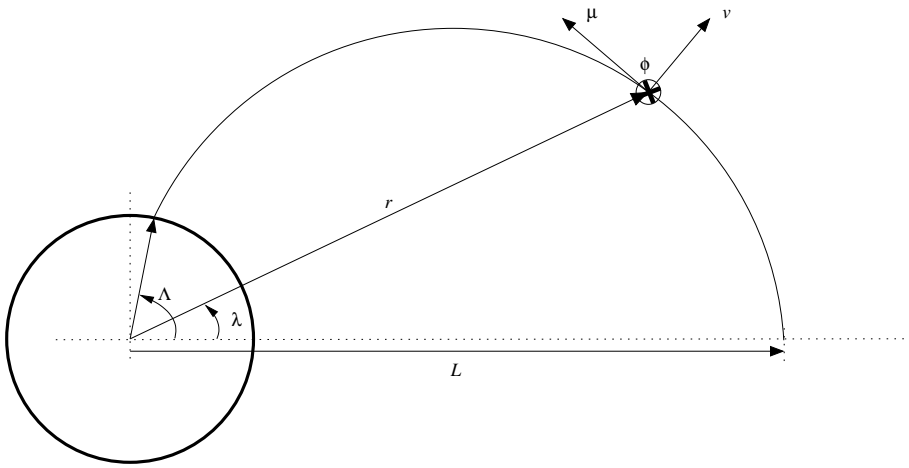

Figure 5.1: Illustration of the various coordinates in a local dipole coordinate system, after Kivelson and Russell [36].

where a is the radius of the earth, r is the distance to the point of interest, λ is the latitude measured positive north of the equator and negative south of the equator, ϕ is the longitude which is identical in both systems, μ is in the direction of the magnetic field and ν is perpendicular to the field and the other two components. The scale factors needed for transforming to Cartesian coordinates are

$$h_\mu = \frac{a\cos^6\lambda}{\nu^3\sqrt{4-3\cos^2\lambda}}$$

$$h_\nu = \frac{a\cos^3\lambda}{\nu^2\sqrt{4-3\cos^2\lambda}}$$

$$h_\phi = r\cos\lambda = \frac{a\cos^3\lambda}{\nu}.$$

In this model a specific field line can be identified by the latitude at which the field line passes through the ionosphere (λ_{iono}), the L-shell number (L) or the dipolar coordinate ν. These descriptions are equivalent because there is a one-to-one relationship between the three. For a specific field line $L = 1/\nu = 1/\cos^2\lambda_{iono}$.

5.3 Dipole differential equations

Perturbation in this dipole field cannot be reduced to a single dimensional dependence as was done in the box model and Cartesian coordinates. We may assume that the variations in time still follow $e^{\imath\omega t}$ and because of the azimuthal symmetry, we can assume the dependence on ϕ is of the form $e^{\imath m\phi}$, where m is a wave number in the ϕ direction.

In dipole coordinates ν, μ and ϕ the differential equation governing the electric field perturbations at frequency ω along a field line in the ν direction is given by ([68] and [64])

$$\frac{d^2\mathcal{E}_\nu}{dz^2} + K^2(\nu)(1-z^2)^{6-p}\mathcal{E}_\nu = -\mathcal{E}_0(1-z^2)^{6-p}. \tag{5.1}$$

Here z is a substitution $z = \sin\lambda$ and K is the normalised frequency and is given by

$$K^2(\nu) = \frac{a^2\omega^2}{V_0^2(\nu)} \tag{5.2}$$

where

$$V_0 = \frac{B_{eq}}{\sqrt{\mu_0\rho_{eq}}}\nu^{4-\frac{1}{2}p}.$$

B_{eq} and ρ_{eq} are the values of the magnetic field and the particle density where the field line crosses the equator, p determines how the number density varies with radius and $\mathcal{E}_0 = C_1 m\omega a$, C_1 being a constant.

Consider equation (5.1). This is an inhomogeneous ordinary differential equation in $\mathcal{E}_\nu$. The right-hand side contains a factor m which describes the perturbations in the azimuthal direction. In terms of the box model (section 3.3), the perturbation moved through the magnetosphere as a compressional wave, coupling with a field line and creating a transverse Alfvén wave on that line. If there were no coupling, then no energy would be transferred from the compressional wave to the Alfvén wave. The coupling was linked to k_y which in our new coordinate system, is analogous to m. If $m = 0$, then equation (5.1) describes the perturbations without a source. This is similar to an un-driven damped harmonic oscillator system. It describes the behaviour of the system when initially perturbed. The perturbation will occur with the characteristic frequency of the system ω_0. If $m \neq 0$ then the right-hand side behaves like a source term for the system. A study of the resonant behaviour of the system is followed by a look at the driven behaviour.

5.3.1 Resonant perturbations

The question is how the electric field varies along a magnetic field line when initially perturbed. The frequency of the perturbation will occur at the resonant frequency for that line. With no coupling ($m = 0$)

$$\frac{d^2\mathcal{E}_\nu}{dz^2} + K^2(1-z^2)^{6-p}\mathcal{E}_\nu = 0 \tag{5.3}$$

with

$$K^2 = \frac{a^2\omega^2}{V^2}.$$

In order to consider losses, a small imaginary part can be added to $K(\nu)$ such that

$$K(\nu)(1 - \imath\epsilon) = K_r + \imath K_i.$$

The differential equation for the azimuthal component of the perturbed magnetic field in a dipole field is

$$\mathcal{B}_\phi = \frac{\imath\nu^2}{KV}\frac{\partial \mathcal{E}_\nu}{\partial z}. \tag{5.4}$$

This differential equation together with the differential equation for $\mathcal{E}_\nu$ can be solved numerically using the Runge-Kutte process. Following the discussions in the box model one can assume that $\mathcal{E}_\nu = 1$ and $\mathcal{B}_\phi = 0$ at the equator. On a specific field line V_0 will be constant and so the behaviour depends only on z. Thus we can find the normalised characteristic frequency K_0 for that line. Practically this is done via an iterative process beginning with a value for K, running the Runge-Kutte process to determine at what latitude $\mathcal{E}_\nu = 0$. One can now vary K until $\mathcal{E}_\nu$ reaches zero at the latitude of interest, thus selecting the right K for that field line.

The latitudes of interest for pulsations in the the radar data are typically $-65°$ to $-70°$ AACGM [16]. These are L-values of 5.6 to 8.5 which at the equator, map to a region of space of approximately 3 earth radii. The determined K values with $\epsilon = 0$ (i.e. K_r) for these latitudes are shown in figure 5.2. Here we can see that the normalised frequency varies almost linearly with latitude with the higher frequencies at the lower latitudes. This can be expected as these field lines are shorter.

Once K_r has been determined then ϵ can be increased until the resulting second order electric field matches the measured values. This will give a value for K_i. The real part and imaginary part of $\mathcal{E}_\nu$ are shown in figure 5.3 for $K = 1.967 - \imath 0.168$.

Although it is not possible to analytically express the un-driven behaviour of $\mathcal{E}_\nu$ it can be said that it varies as $f(z, \nu)$, where f is unknown but can be described numerically.

5.3.2 Driven perturbations

Assuming the system is driven, i.e. $m \neq 0$, meaning that a field line characteristic frequency does not necessarily match the driving frequency, the response of the different field lines to the driving perturbation will be studied.

It has been shown [68] that, although un driven behaviour of $\mathcal{E}_\nu$ explicitly contains a dependence on ν, this variation is small enough to be ignored (see figure 3 of Walker's paper [68]). Furthermore, it is assumed that the variation in z in the driven case is the same as in the un driven case, so $\mathcal{E}_\nu$ will have the same relationship $f(z)$. Consequently the dependence of $\mathcal{E}_\nu$ on ν must derive from an as yet unspecified function. Thus

$$\mathcal{E}_\nu = f(z, \nu)g(\nu) \approx f(z)g(\nu), \tag{5.5}$$

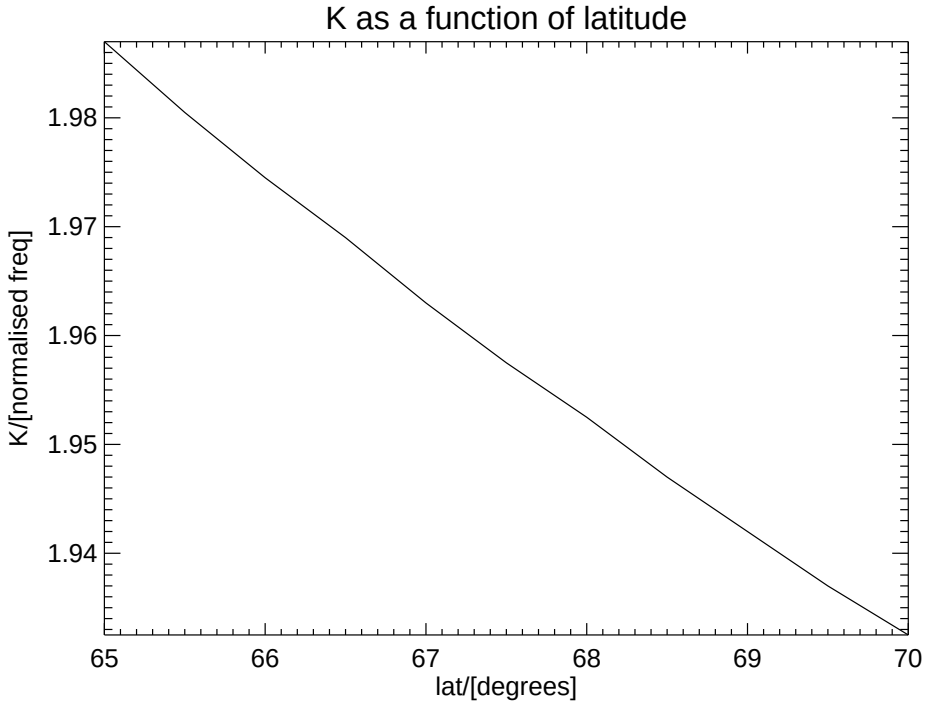

Figure 5.2: The variation of normalised frequency K with latitude.

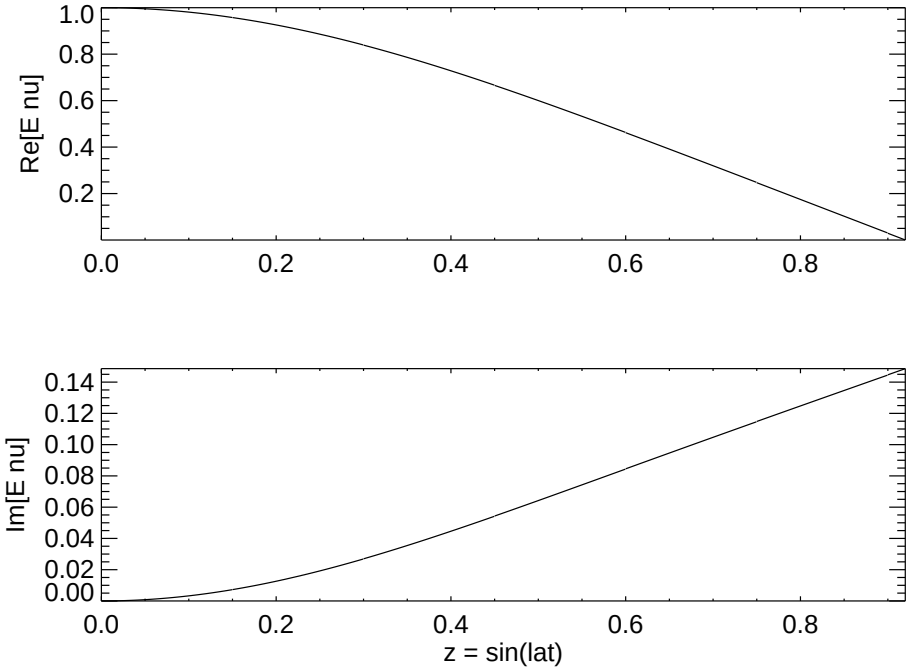

Figure 5.3: $\Re[\mathcal{E}_\nu]$and $\Im[\mathcal{E}_\nu]$ plotted as a function of $z = \sin\lambda$.

where $g(\nu)$ must still be found.

Because the dependence of $\mathcal{E}_\nu$ on z is the same in both the driven and un-driven cases, it follows that $\partial^2\mathcal{E}_\nu/\partial z^2$ will be the same in both cases. After some substitution and algebra

$$\mathcal{E}_\nu = -\frac{\mathcal{E}_0}{\left[K^2(\nu) - K_0^2\right]} = -\frac{\mathcal{E}_0}{K_T^2} = f(z)g(\nu),$$

where K_0^2 is the un-driven normalised characteristic frequency for a resonant field line ν_0. As $g(\nu)$ governs the dependence of $\mathcal{E}_\nu$ on ν, then

$$g(\nu) = \frac{A}{K_T^2}, \tag{5.6}$$

where A is a constant in ν and the dependence of K_T^2 on ν comes from equation (5.2).

So

$$K_T^2 = K^2 - K_0^2 = K^2 - (K_r + \imath K_i)^2 \approx \left[K^2 - K_r^2\right] - \imath 2K_rK_i,$$

which, if we write K, K_0 and K_r out explicitly, is

$$K_T^2 = \left[\frac{a^2\omega^2}{V^2} - \frac{a^2\omega_0^2}{V_0^2}\right] - \imath 2K_i\frac{a^2\omega_0^2}{V_0^2}.$$

ω_0 and V_0 are the resonant values, ω is the current driving frequency and V is the Alfvén velocity on the field line of interest, K_i is the term to include a finite Pedersen conductivity and is analogous to equation 4.10.

Again we see that if $K_i = 0$, then $K_T^2 = 0$, when the driving frequency (ω) matches the resonant frequency (ω_0) for the field line, and $g(\nu)$ will be singular. With $K_i \neq 0$, $g(\nu)$ will not be singular.

Example

Using $a = 6.4 \times 10^6 m$, $B_{eq} = 3.17 \times 10^{-5} T$, $\mu_0 = 4\pi \times 10^{-7} H \cdot m^{-1}$, $\rho_{eq} = m_p n_p$ (with $m_p = 1.6726 \times 10^{-27} kg$ and $n_p = 15 \times 10^6 m^{-3}$) gives $\rho_{eq} = 2.5089 \times 10^{-20} Kg \cdot m^{-3}$, $p = 6$ and choosing the resonant L-shell to be 7, one can plot how $\left|1/K_T^2\right|$ varies with L.

In order to determine the effect of K_i on the amplitude profile $\left|1/K_T^2\right|$ was plotted against L for $K_i = 0 \cdot K_r$, $0.01 \cdot K_r$, $0.1 \cdot K_r$ in figures 5.4, 5.5 and 5.6. Looking at the shape of the plots then it is clear that as K_i gets larger, the peak broadens. This means that if the ionospheric conductivity is high (K_i will then be small) then the resonance peak will narrow. Conversely, if the conductivity is low, one would expect the resonance peak to

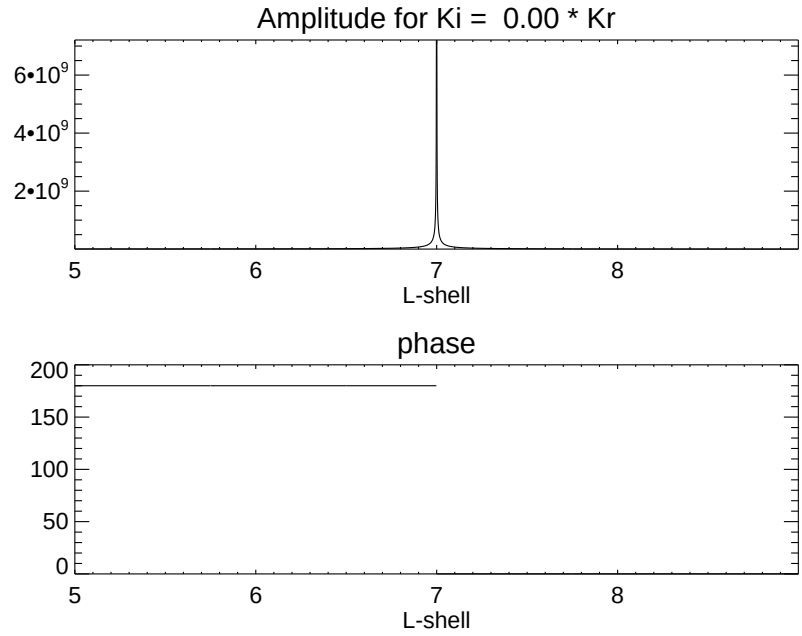

Figure 5.4: $\left|1/K_T^2\right|$ plotted against L for $K_i = 0 \times K_r$.

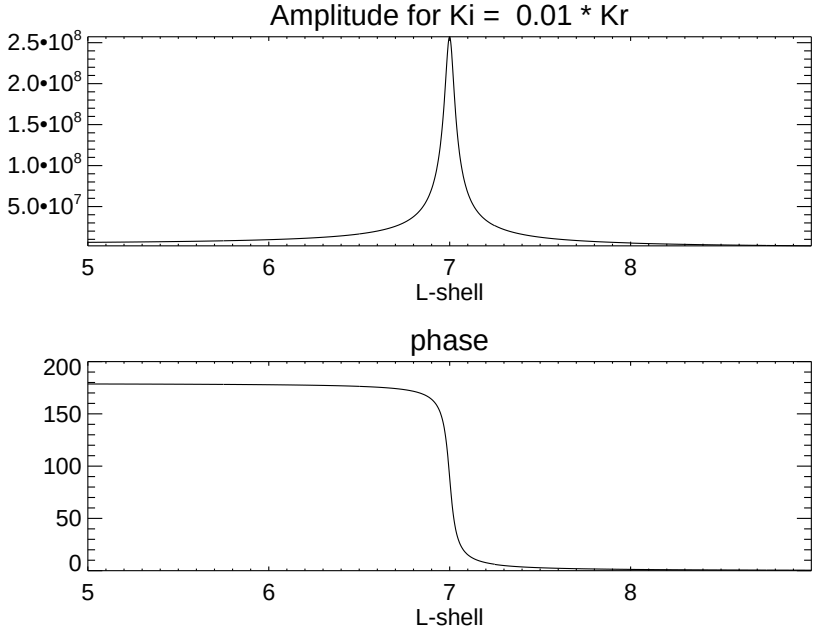

Figure 5.5: $\left|1/K_T^2\right|$ plotted against L for $K_i = 0.01 \times K_r$.

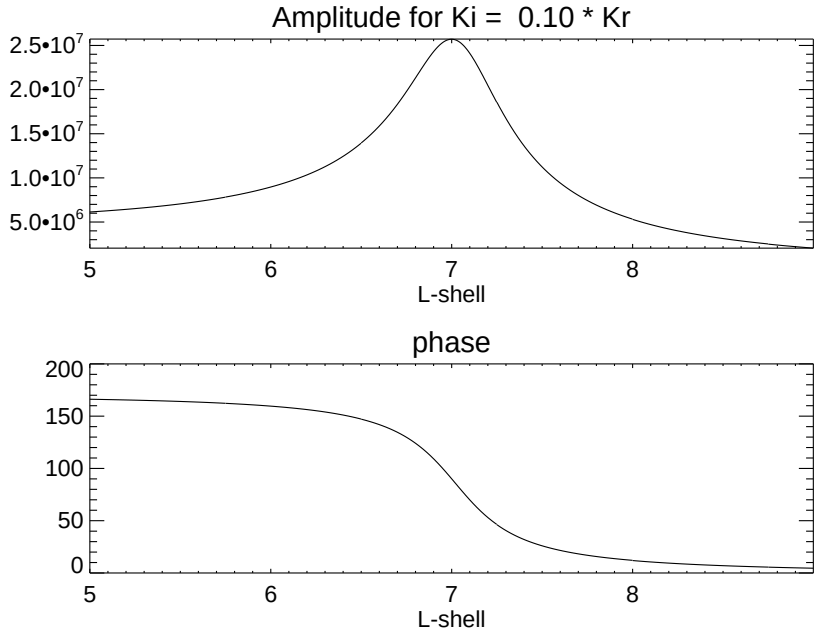

Figure 5.6: $\left|1/K_T^2\right|$ plotted against L for $K_i = 0.1 \times K_r$.

broaden. A non-zero value of K_i was attributed to the dissipation of energy in the ionosphere, thus preventing the singularity from occurring. If $K_i = 0$ then (although not clear in figure 5.4) the amplitude function will be singular. As K_i increases so the amplitude decreases, indicating that some of the energy has been dissipated in the ionosphere. The phase plots indicate that one should expect a phase change of 180° across the resonance.

5.3.3 Finding K_i

Following that

$$b_\phi = \mu_0 \Sigma_P E_\nu \sin\chi,$$

where χ is the magnetic dip angle, then

$$\frac{\mathcal{B}_\phi}{h_\phi} = \mu_0 \Sigma_P \frac{\mathcal{E}_\nu}{h_\nu} \sin\chi.$$

Thus

$$\mathcal{B}_\phi = \frac{h_\phi \sin\chi}{h_\nu} \mu_0 \Sigma_P \mathcal{E}_\nu = -2\nu z \mu_0 \Sigma_P \mathcal{E}_\nu = \frac{\imath\nu^2}{KV} \frac{\partial \mathcal{E}_\nu}{\partial z},$$

as $(h_\phi \sin\chi)/h_\nu = -2\nu z$ and using (5.2) one can now substitute $KV = a\omega$ to get

$$\mathcal{E}_\nu + \frac{\imath\nu}{a\omega\mu_0\Sigma_P z}\frac{\partial\mathcal{E}_\nu}{\partial z} = 0.$$

This gives

$$\mathcal{E}_\nu + \imath\xi\frac{\partial\mathcal{E}_\nu}{\partial z} = 0,$$

where

$$\xi = \frac{\nu}{a\omega\mu_0\Sigma_P z}.$$

K_i can be approximated to first order using the method outlined in *Taylor and Walker* [64] to get

$$|K_i| = K^{(0)}\,|\zeta|$$

with $|\zeta| = 2\xi/s_0$, $K^{(0)}$ is the zero order approximation and where $s_0 = 2z_0 = 2\sin\Lambda$.

So for $|K_i|$

$$|K_i| = \frac{\pi}{s_0}\frac{2\xi_{z=z_0}}{s_0} = \frac{2\pi\nu}{a\omega\mu_0\Sigma_P s_0^3}. \tag{5.7}$$

Note here that equation 5.7 differs from the equation ($k^{(1)}$) given in Taylor and Walker [64] by a factor of $1/a$.

Example

Given a perturbation of 3.6 mHz measured with the radar at an L-value of 8 (69.3° mag lat) and a Pedersen conductivity of $2.5S$ it follows from equation (5.7)

$$|K_i| = \frac{2\cdot\pi\cdot 0.125}{6\times10^6\cdot 2\pi\cdot 3.6\times10^{-3}\cdot 4\pi\times10^{-7}\cdot 2.5\cdot(2\cdot\sin 69.3)^3} = 0.28$$

5.4 Applicability

The level of ionospheric conductivity, Σ_P, determines if there will be pulsating electric fields in the ionosphere and the width of the resonant structure. The radar has a wide field of view and it can observe pulsations that are associated with field lines of differing L-values. The measured amplitude characteristics can then be plotted as a function of

geomagnetic latitude (or L-shell). Now one of two parameters can be determined. If the ionospheric conductivity is known, then one can infer how V varies with L-shell or if the variation in V is known, then one can infer the ionospheric Pedersen conductivity.

The Pedersen conductivity can be measured using incoherent scatter radars, while the variation of V with ν can be measured using VLF waves or by *in situ* satellite measurements.

5.5 Summary

If a field line is initially perturbed and not driven, then the field line will pulsate at the natural resonant frequency of that field line. One can determine that frequency for a given line using the method outlined in section 5.3.1. If the system is driven, then the different field lines will respond differently. The amplitudes of the pulsations in the equatorial plane will vary as $g(\nu)$ and will have a maximum on the field line of which the characteristic frequency matches the driving frequency. The amplitudes will fall away moving further from the field line. The SuperDARN radars can measure the amplitude variation as a function of latitude in the ionosphere. These values can be mapped into the equatorial plane to provide methods of measuring (or confirm measurements of) magnetospheric plasma density or ionospheric conductivity.

Chapter 6

The SuperDARN Radar

6.1 Introduction

As this is the primary instrument used in this analysis, a detailed description will be given of the radar. The following will be discussed: the operation of the radar, the way the data is recorded, the types of data available for analysis and finally, how the data can be used for Pc5 pulsation analysis.

6.2 The SuperDARN network

The SuperDARN (Super Dual Auroral Radar Network) had its beginnings in the HF and VHF coherent scatter radars known as DARN [30]. The network consists of 16 operational radars [5]. The names and locations of the radars are given in table 6.1. The usefulness of the radar network is the collaborative agreement that controls radar operation. Radar operation is divided into three different modes, namely, Common, Special and Discretionary time.

In the Common mode, the entire network will run in a mode that is accepted by all the Principal Investigators (PI's) as the mode most useful to the SuperDARN community. Common mode time is run for 50% of the radar operation.

In Special mode the radars are set into an agreed upon mode that seeks to address one specific scientific goal. Times during which the radars are conjugate with various spacecraft is a good example of special mode use. Special mode time is limited to 20% of the radar schedule.

Discretionary time is time during which individual PI's may use the radar in whatever mode they desire. Discretionary mode time is limited to 30% of the radar schedule.

The radar schedule for a specific month is agreed upon and distributed to all the PI's. The schedule will contain the control programmes and switching times for the entire network

Northern Hemisphere						
Name	Location	Code	Geographic		AACGM	
King Salmon	Alaska, USA	c ksr	58.68 N	156.65 W	57.43 N	100.51 E
Kodiak Island	Alaska, USA	a kod	57.60 N	152.2 W	57.17 N	96.28 W
Prince George	BC, CAN	b pgr	53.98 N	122.59 W	59.88 N	65.67 W
Saskatoon	Saskatchewan, CAN	t sas	52.16 N	106.53 W	61.34 N	45.26 W
Kapuskasing	Ontario, CAN	k kap	49.39 N	82.32 W	60.06 N	9.22 W
Goose Bay	Nfld, CAN	g gbr	53.32 N	60.46 W	61.94 N	23.02 E
Stokkseyri	ICELAND	w sto	63.86 N	22.02 W	65.04 N	67.33 E
Pykkvybaer	ICELAND	e pyk	63.86 N	19.20 W	64.59 N	69.65 E
Hankasalmi	FINLAND	f han	62.32 N	26.61 E	59.78 N	105.53 E
Southern Hemisphere						
Name	Location	Code	Geographic		AACGM	
Halley Station	Antarctica	h hal	75.52 S	26.63 W	61.68 S	28.92 E
SANAE	Antarctica	d san	71.68 S	2.85 W	61.52 S	43.18 E
Syowa South	Antarctica	j sys	69.00 S	39.58 E	55.25 S	23.00 E
Syowa East	Antarctica	n sye	69.01 S	39.61 E	55.25 S	22.98 E
Kergeulen	Kergeulen Island	p ker	49.35 S	70.26 E	58.73 S	122.14 E
TIGER	Tasmania	r tig	43.38 S	147.23 E	55.31 S	133.36 W
Unwin	New Zealand	u unw	46.51 S	168.38 E	55.15 S	106.54 W

Table 6.1: Names and locations of the SuperDARN radars used in this analysis[5].

to ensure that all the radars are operating in the same mode at the same time. If a PI has no specific use for the radar in discretionary mode, it is usually set into the common mode operation.

6.3 Radar targets

For a radar to operate, the RF energy needs to be scattered off a target. In typical radar applications this target is an object of some sort, such as an aircraft. There are three main classes of ionospheric radars and they are divided here by the nature of their targets.

6.3.1 Ionosondes

Ionosondes are used to characterise the electron densities of the bottom side of the ionosphere [40]. They transmit RF energy vertically towards the ionosphere and if the transmitted RF energy is below the plasma frequency of the ionospheric plasma, the energy will be reflected back to the ground for reception. The time of flight of the pulse can be measured to determine the range of the layer of the ionosphere where the plasma frequency matches the sounding frequency. By stepping through the required frequencies, the bottom side of the ionosphere can be characterised. Ionosondes typically start at 500 kHz and keep increasing in small steps until the signal finally penetrates the ionosphere. The highest signal to be returned is designated foF2 varies significantly.

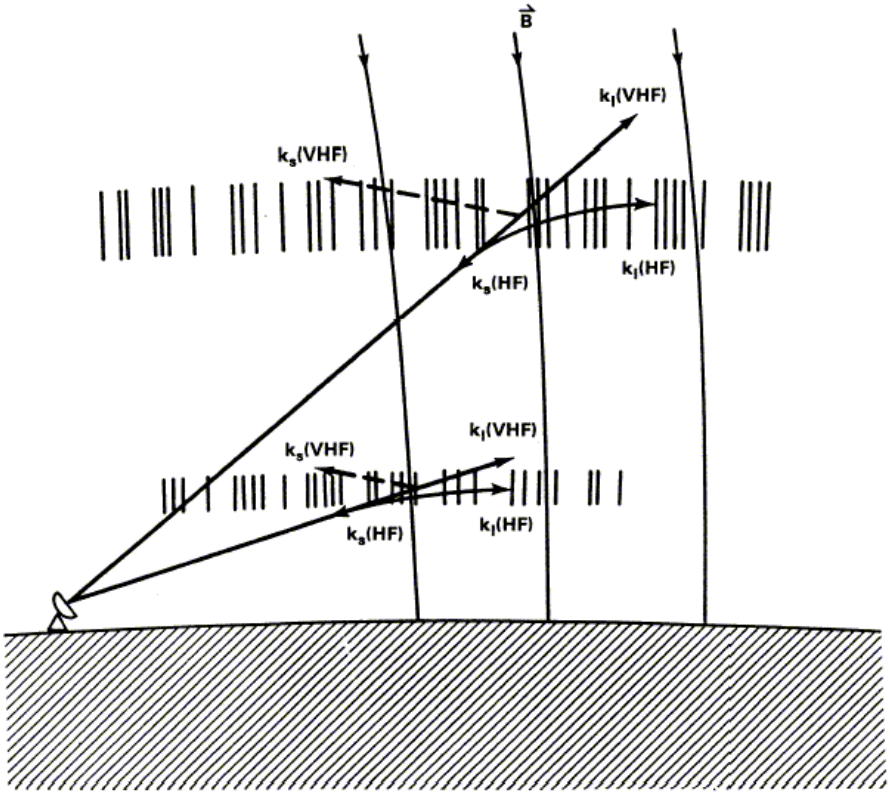

Figure 6.1: VHF and HF scatter from coherent ionospheric irregularities [30].

6.3.2 Incoherent scatter radars

An incoherent scatter radar is able to characterise the entire ionosphere [22]. Large amounts of RF power, typically MW levels, are transmitted at UHF frequencies towards the ionosphere. Each electron in the ionosphere will scatter part of the RF energy back through Thomson scattering. The higher the density of the ionospheric plasma, the larger the returned power. The time of flight verses power levels can be used to determine electron densities throughout the ionosphere above the radar.

6.3.3 Coherent scatter radars

HF radars have long been used to observe naval targets as part of Over The Horizon Radars (OTHR). In the case of coherent radars, the targets are not the ionosphere vertically above the radar but rather the signal is directed horizontally towards scattering regions where the coherent interference from partially scattered signals constitute significant backscattered power. This can be seen in figure 6.1 and 6.2. Here the scattering regions are indicated by vertical field-aligned striations that indicate areas of varying electron density. As the signal passes through these variations it is partially reflected and transmitted. If the signal is orthogonal to the variations then there will be reflected scatter. Earlier VHF radars were able to create coherent scatter, but if the incident angle was incorrect the scattered

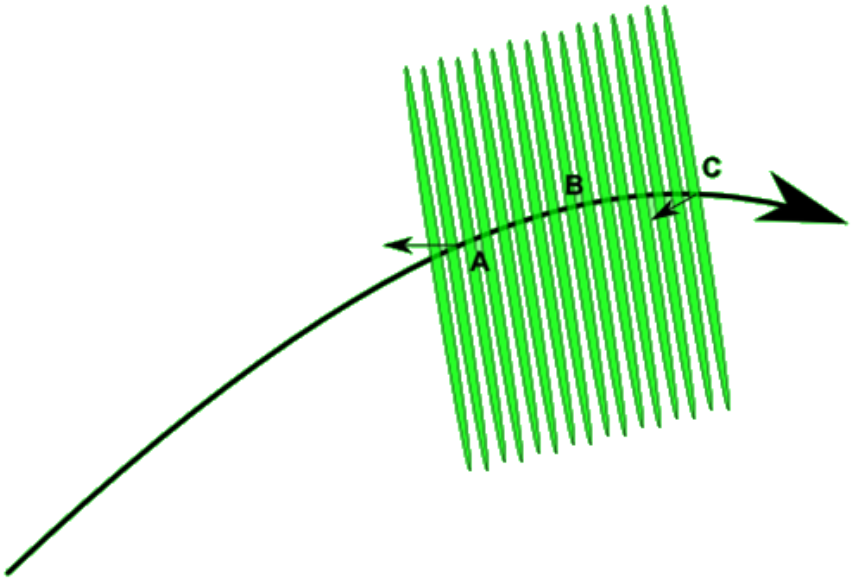

Figure 6.2: An HF ray path through the ionosphere. The signal is orthogonal at B but not A and C.

signal could be lost in space. HF signals are refracted in the ionosphere. Any signal that is reflected by the irregularities will follow the same path back to the transmitter as the path it followed while incident. Figure 6.1 shows the incident ray paths for both VHF and HF signals radiating two different parts of the ionosphere. The indicated ray path of the HF signal is refracted and eventually orthogonal to the ionospheric irregularities. The scattered signal follows the same path as the incident signal. In this example the VHF signal is lost.

The discussion in this thesis focuses on the pulsation signatures observed in the scatter and not on the cause of the irregularities themselves.

6.4 Radar operation

6.4.1 The system components

The basic radar system consists of a frequency synthesiser to create and receive the RF energy, a splitter to create 16 channels, a phasing matrix to phase the 16 signals relative to each other, 16 power amplifiers, 16 antennas in an array and a computer system to control the system and record the data.

Control

The system is controlled by two personal computers running the QNX real time operating system. The choice of QNX allows the precise timing required to create the pulse sequence that is ultimately used to create the auto-correlation functions for the received signal

Pulse synthesis

The SuperDARN radars are designed to operate between 8 and 20 MHz. Once the sounding frequency has been decided by the current control programme, the radar will synthesise a 300 μs pulse of RF energy at the desired frequency. The pulse is shaped to avoid harmonic distortion. The pulse then passes through a splitter that divides the signal into 16 channels.

Phasing matrix

The purpose of the phasing matrix is to change the phase of the 16 signals relative to each other so that when transmitted a narrow beam can be formed. For a given frequency, the beam that is formed is determined by the number of antennas in the array as well as the phase difference between the the signals transmitted by each antenna. The phase difference will determine the direction of the beam and the number of antennas that controls the beam width [38].

Inside the phasing matrix the signal passes through a set of switched delays. Each delay will retard the phase of the signal by a predetermined amount depending on the direction of the beam. At the output of the phasing matrix there are 16 channels with each signal suitably phased.

Each signal is then amplified and transmitted on its own antenna.

Receiver

Once a pulse has been transmitted, the system will switch into receive mode. The signal at the antenna is routed to the phasing matrix where the same phase that was used in transmission is subtracted from the signals. The 16 signals are then added together and routed to the receiver. The radar uses a superheterodyne receiver to mix the received signal via an intermediate frequency to a base band signal with the final stage of mixing producing the base band and a 90° phase shifted version of the base band. These two signals are referred to as the I and Q signals respectively.

Interferometer

If an interferometer is installed at the radar then a second receiver is necessary. The second receiver will sample the interferometer at the same time that the main receiver is sampling the main array. The difference in phase of the signals received on the two receivers can be used to determine the elevation angle of the signal received from the ionosphere.

6.5 Received signal processing

6.5.1 Transmitted signal

A radar works on the principle that the range of a target can be determined by measuring how long it takes for a radio pulse to travel from the transmitter to the target and back again. The transmitted signal $s(t)$ is a continuous wave (CW) modulation of a carrier. CW modulation can be thought of as an on-off keying of the carrier. In order to reduce harmonic distortion the carrier is in fact modulated with a Gaussian shaped pulse $p(t)$ and so the transmitted signal is a linear multiplication of the Gaussian pulse $p(t)$ with a carrier signal $\sin(2\pi f_0 t)$ or, in complex form $\exp[\imath 2\pi f_0 t]$, to create the following transmitted signal

$$s(t) = p(t)\exp[\imath 2\pi f_0 t].$$

6.5.2 The received signal

For radar applications the received signal $r(t)$ may be a superposition of several multi-path echoes (i.e. echoes which have travelled over various propagation paths between the transmitter and receiver) reflected at various ranges from various irregular features in the ionosphere. The received multi-path signal $r(t)$ which is an attenuated and time delayed (possibly multiple time delays) replica of the transmitted signal $s(t)$. It can be represented as,

$$r(t) = \sum_{i=1}^{P} a_i s(t - \tau_i)$$

or

$$r(t) = \sum_{i=1}^{P} a_i p(t - \tau_i)\exp[\imath 2\pi f_0 (t - \tau_i)], \tag{6.1}$$

where Σ shows that the P multi-path signals sum linearly at the receiving antenna, a_i is the amplitude of the ith multi-path component of the signal, and τ_i is the propagation delay associated with multi-path i. After removing the carrier, the modified $r(t)$, now represented by $r_1(t)$ becomes:

$$r_1(t) = \sum_{i=1}^{P} \alpha_i p(t - \tau_i),$$

where the carrier phase of each of the multi-path components is now represented by a complex amplitude α_i which carries along the RF phase term and $p = 1$ when $t = \tau$.

It is possible to make the same measurement over again, that is, to transmit the same frequency pulse more than once. If the received signals are coherent then the signals can be added to achieve a cleaner and more detectable signal. If $r_1(\tau)$ is the amplitude at $t = \tau$ of reflections from parts of the ionosphere $\frac{c\tau}{2}$ away and one were to transmit a second pulse at the same frequency, then under steady state conditions, one would obtain an identical $r_2(\tau)$ at the same time after the second pulse. If the target were moving, there would be a phase difference between r_1 and r_2 that would be determined by the velocity of the target and manifested as a Doppler shift in the signal.

6.5.3 The timing

The length of the transmitted pulse

In a standard radar, once the transmitter begins transmitting the receiver will saturate and so the transmitted pulse must be turned off before the first echoes are expected to arrive at the receiver. This determines the maximum length of the transmitted pulse. If a second pulse it to be transmitted for the purpose of determining the Doppler shift, then the transmitter should wait until the last possible echo has returned. This determines the pulse repetition rate of the radar.

This is not the case for a SuperDARN radar.

The intention of the radar is to record echoes from as far as 3555km away. This means that, in order not to contaminate echoes, the system should wait until the last possible echo has been received before it begins with the next pulse. This would mean that the system would have to wait $\frac{2d}{c}$ seconds where d is the range and c is the speed of light. This amounts to waiting 24 ms before transmitting the next pulse. Waiting this long means that you are only sampling the same region of ionosphere every 24 ms and subsequently according to Nyquist theory, can only resolve motions with a period of 21 Hz. At 12 MHz transmitted signal this translates into a maximum Doppler velocity of 263 m/s which is not suitable for polar ionospheric convection analysis.

To avoid this problem the SuperDARN radars will transmit pulses before the last expected pulse has returned. They achieve this by making use of a staggered pulse pattern with each pulse length being $300\,\mu s$ long and rely on the fact that, although there will be interference, the noise will decorrelate and be cancelled.

The staggered pulse pattern

The way the radar achieves a sampling rate high enough to resolve large Doppler velocities without having to wait for the echoes from the further ranges is to transmit pulses before the echoes from the farthermost ranges have returned. It achieves this by transmitting

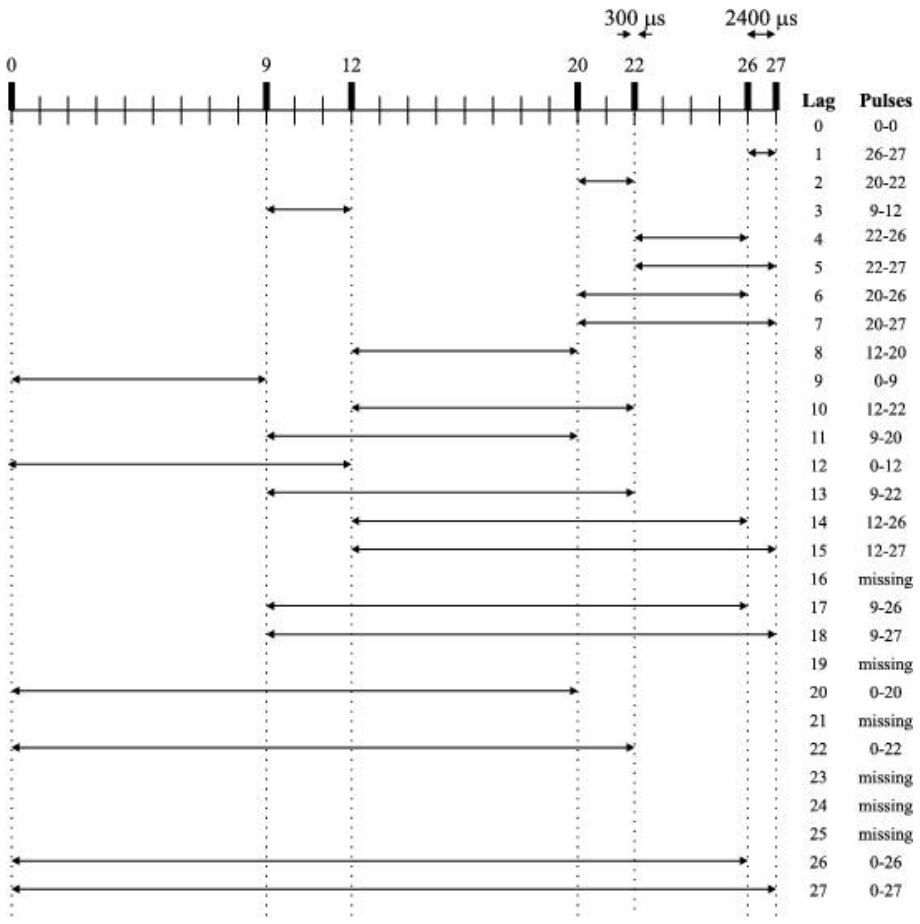

Figure 6.3: The staggered pulse pattern showing how the various ACF lags can be created from the seven pulses.

a staggered pulse pattern. An example of the staggered pulse pattern and its timing is shown in figure 6.3.

In this example the first pulse is transmitted at what is known as lag 0 where a lag time is 2.4 ms. 9 lags later 21.6 ms, a second pulse is transmitted. 3 lags later 7.2 ms, the next pulse is transmitted, then 8 lags (19.2 ms), then 2 lags (4.8 ms), then 4 lags (9.6 ms) and finally 1 lag later, that is 2.4 ms, the final pulse is transmitted.

Transmitting before the last echoes have returned means that at some point in time one may be receiving echoes from two different pulses, and from possibly two significantly different regions of the ionosphere. This is where the nature of the pulse pattern becomes significant. It is assumed that the region of ionosphere of interest will remain coherent for the duration of the pulse pattern. If this is the case then a correlation between two different samples made at the same time after a pulse was transmitted, will be high for reflections from the same region and low if the echo is from different regions.

After the first pulse was transmitted, the receiver starts to make samples every 300 μs and continues to do so until 24 ms after the last pulse. The 24ms is required for the last possible echo to return from 3555 km. This means that it takes approximately 90 ms to complete one pulse sequence. Once the pulse sequence has been completed, an auto correlation function is generated for each range [15]. The generation of the ACF is discussed in detail in appendix D.

6.6 Doppler velocity

If one were to look at a slab of ionosphere with thickness ds, then the time it would take for the phase front of an electromagnetic signal, perpendicular to the slab, to travel through the slab would be

$$\Delta t = \frac{ds}{v_p},$$

where v_p is the phase velocity of the signal.

The phase thickness of the slab is calculated from

$$ds = c\Delta t = c\frac{ds}{v_p} = \mu ds$$

with the phase refractive index (μ) given by the Appleton-Hartree equation. The phase range then is represented by

$$S = \int_0^{S_r} \mu ds$$

The rate of change of the phase range $\frac{dS}{dt}$ gives a velocity V and

$$V = \frac{dS}{dt} = \frac{d}{dt}\int_0^{S_r} \mu ds.$$

The rate of change of phase range is measured by observing the rate of change of phase of the successive pulses and is indicated by the Doppler shift of the signal. This velocity is then measured by the Doppler shift on the signal [26] as,

$$V = \frac{c\Delta f}{2f}, \tag{6.2}$$

where V is the Doppler velocity, c is the speed of light, Δf is the Doppler shift on the signal and f is the sounding frequency.

The Doppler velocity V is dependent on three terms [63], namely variations in the magnetic field and electron density and the motion of the ionosphere.

6.7 Angle of arrival

Each reflected signal can be characterised by a radio wave with propagation vector $\mathbf{k}$. The distance between the ionosphere and the receiver antenna array is much larger than the separation of the antennas and thus the reflected wave is considered a plane wave with the same $\mathbf{k}$. The direction of $\mathbf{k}$ is then the Angle of Arrival (AoA) of the reflection.

If one assumes a plane wave received at two antennas separated by $\mathbf{d}$, then the instantaneous phase difference between the two antennas is

$$\Delta\psi_{12} = \mathbf{k} \cdot \mathbf{d}$$

$$\Rightarrow \Delta\psi_{12} = \frac{2\pi}{\lambda}|\mathbf{d}|\cos\phi_{12}$$

$$\Rightarrow \Delta\psi_{12} = \frac{2\pi d \sin\theta_{12}}{\lambda}$$

resulting in

$$\sin\theta_{12} = \frac{\Delta\psi_{12}\lambda}{2\pi d}, \tag{6.3}$$

where $\Delta\psi_{12}$ is the phase difference between the signals received on antenna(1) and antenna(2) respectively, $|\mathbf{d}|$ is the separation between the two antennas, λ is the free space

wave-length of the signal and $\theta_{12} = (90° - \phi_{12})$ with ϕ_{12} being the angle between the wave vector **k** and **d**.

The ionospheric conditions mentioned above determine that the phase relationship between successive pulses received at separated antennas will be linear, i.e.

$$\varphi(t) = \omega_0 t + \phi.$$

The first term is the result of the Doppler velocity V while the second is the instantaneous phase constant introduced because of the separation of the antennas.

6.8 The radar sounding procedure

The field of view of each radar is divided into a grid with 16 beams each with 3° beam width and 75 range gates per beam, with 45 km separation for each range. When operating in the standard mode the radar will select a beam and begin with its staggered pulse sequence. Repeated pulse sequences are processed during what is known as the integration time and the result is a fitted ACF for each range. Once the integration time for sounding a beam has expired, the radar will move onto the next beam and repeat the process. Once all the beams have been sampled the radar will repeat the whole process.

This beam switching process means that a specific beam will only be re-sampled once all the other beams have been sampled. If the radar is operating in what is known as the slow-scan mode with an integration time of 7 seconds, each beam will be sampled every 16 x 7 = 112 seconds. Time must be allowed for the setup and processing of each beam, so the accepted sampling time is approximately 120 seconds for the slow-scan mode. To reduce the sampling period, a fast-scan mode was implemented with a 3.5 second integration period. This reduces the sampling period to approximately 60 seconds.

Other special modes exist where certain beams are over-sampled. Instead of the normal sequence of

1,2,3,4...,16,1,2,...

there may be a sequence of

1,3,**2**,7,**3**,11,**4**,3,**5**,7,**6**,11,**7**,3,**8**,7,...

Here the normal sequence (in bold) is interspersed with the beams 3, 7 and 11. These three beams will then have a higher sampling rate than the other beams. An example of a special mode used to study ULF pulsations is discussed in *Yeoman and Wright* [78]. The radar will continue its sounding for two hours. Thereafter the data are written to file and the process is repeated.

6.9 Radar data

The working data product of the radar is a two hour data set known as a FIT file. The term FIT comes from the fact that the data that are stored in this file are the parameters used to create the fitted function for the ACF for each range. The data in the FIT file are sectioned according to the beam number. For example, for a two hour period, one block of data, for say beam 0, will be a three dimensional array of power/velocity/spectral width/elevation (and their associated errors) with recording time on the x axis, range gate on the y axis and the associated parameter for that point.

It is important to note that the time axis is beam specific. As was noted in the previous section (6.8), the sampling period of the beams need not be uniform. This creates problems for merging instantaneous values from two radars as there is no guarantee that two common cells from the two radars will be sampled at the same time. This problem is covered in chapter 12.

An example of a summary plot is given in figure 6.4. The summary plot gives a good indication the of operation of the radar for a given day on a specific beam.

Although an ACF is generated for every range in a beam, the FITACF process will discard those ACF's that are deemed to be noise. This introduces data gaps in the FIT data. The white areas in the plots in figure 6.4 are where the FITACF process determined that the ACF for that range at that time was a noise ACF and so was not included in the FIT file.

6.10 Applicability

If a field line pulsation occurs on the magnetic field lines that pass through the ionosphere being monitored by the radar, then the associated pulsating $\mathbf{E}$ field will cause the local bulk ionosphere to move with an $\mathbf{E} \times \mathbf{B}$ drift. The irregularities inside the ionosphere will also experience this force and will move with the varying ionosphere. This movement is manifested as a periodic variation in the Doppler velocity recorded by the radar.

When operating in the standard mode, the radar will sample its field of view into a grid of samples. The size of each sample in the grid is determined by the azimuthal beam width and the range separation. These are in turn hardware controlled by the phasing matrix and the receiver sampling period. Any deviations from the designed specifications for these two hardware parameters can result in samples from incorrectly specified regions. *Walker* [73] calculated that the region over which a pulsation occurs is of the order of one degree. If the phasing matrix of a radar is incorrectly calibrated this could mean that the whole beam pattern could be out by the order of one beam width, rendering the radar incapable of sampling the correct area. This becomes even more significant when data from two different radars are merged to determine the resultant motion of the ionosphere. If fine

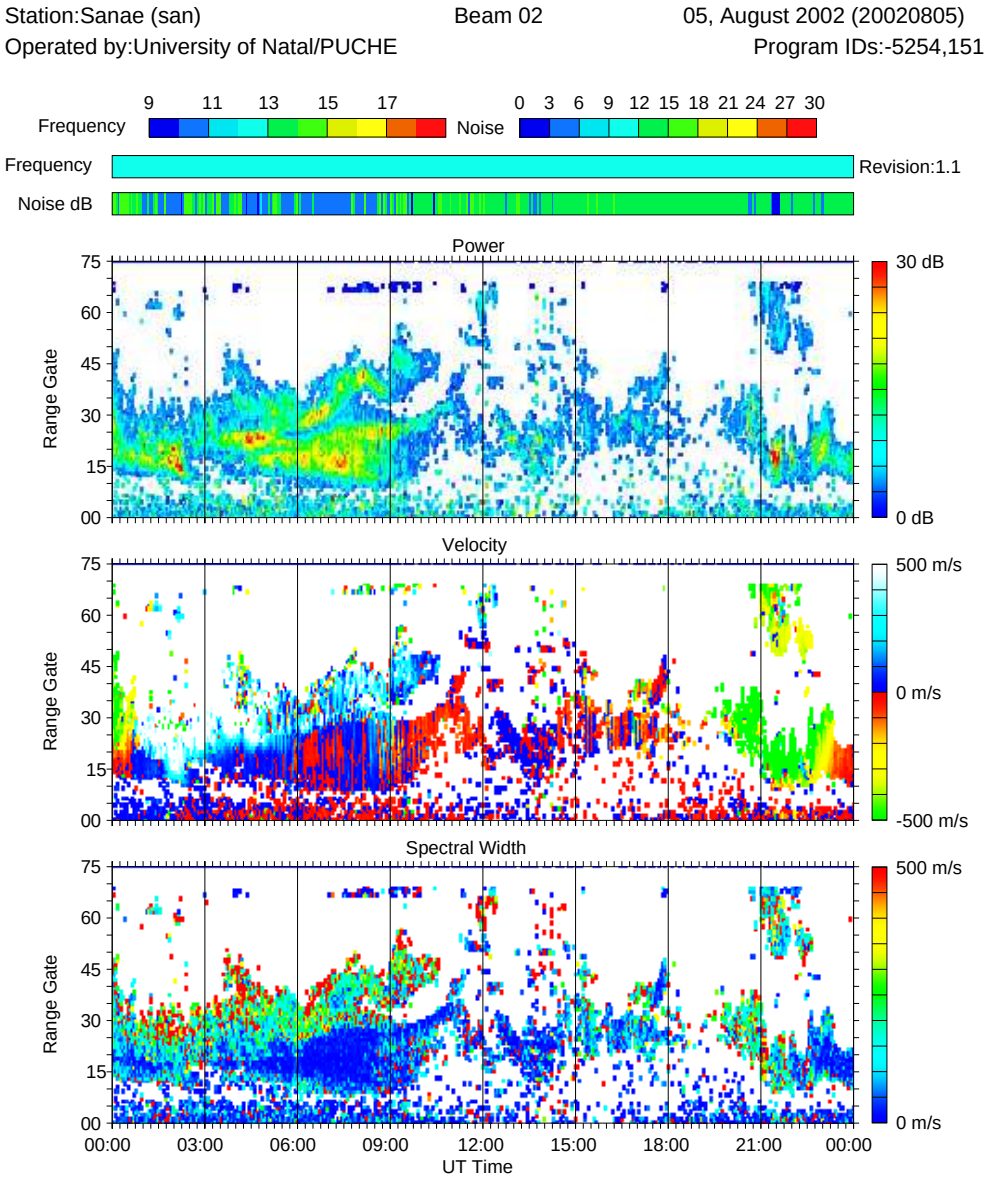

Figure 6.4: A 24 hour summary plot of the FIT data for SANAE radar, beam 2 on 5 August 2002. The panels show the transmit frequency, the measured sky noise and the FITACF power, velocity and spectral width each plotted as a function of beam range.

positional information is needed then one needs to ensure that the hardware is functioning correctly.

The second issue regarding the efficacy of the radar as a tool for measuring pulsations is the time lapse between successive samples of the same area. This is different from the receiver sampling period. In the slow scan mode the radar will sample the same region of the ionosphere every 120 seconds. This puts an upper limit (4.17 mHz) on the types of pulsations that can be observed. Faster scans are possible, but this reduces the integration time and results in poorer signal to noise ratios. Interspersed scans are also possible but they only sample a specific area in detail and for studies that require global information these fall short.

6.11 Summary

A SuperDARN HF radar uses ionospheric field aligned irregularities as its targets. In the polar ionosphere these irregularities may have a periodic structure. If the signal is orthogonal to this structure and its periodicity is such that the scatter is constructive, then sufficient signal will be reflected back to the transmitter. The time of flight of the signal is recorded to determine the range of the target. In order to determine the velocity of the targets, a staggered pulse pattern is transmitted and an autocorrelation function (ACF) is determined for each range. The ACF is fitted with a mathematical function and uses signal power, Doppler shift and spectral width as parameters. The parameters that yield the best fit are then stored as the received power, Doppler velocity and spectral width for that range. Pulsations are then evident as periodic variations in the Doppler velocity measured by the radar caused by the pulsating electric field in the ionosphere.

Chapter 7

Other instruments used in this analysis

Although the main focus of this thesis is to study pulsations observed in the SuperDARN data, the cause and nature of the pulsations can often be confirmed by correlating the data events seen in the radar data with other geophysical data sets. In this thesis use was made of various ground based magnetometer and space borne satellite systems.

7.1 Magnetometers

The original work into pulsation analysis were made using magnetometers [60, 53]. Although magnetometers are limited in their spatial resolution [34], they can still provide a mechanism for corroborating the occurrence of pulsation events as well as providing pulsation data when the radar systems do not have any pulsation scatter.

7.1.1 Southern Hemisphere

In the southern hemisphere, data was used exclusively from the British Antarctic Survey Low Power Magnetometer network, figure 7.1. The magnetometers have low resolution, about 1nT, but are able to confirm the presence of strong ground based pulsations.

7.2 Satellites

Satellite data was used to determine the state of the space environment for correlation with the measurements made on the ground. The Geocentric Solar Magnetospheric (GSM) coordinates system will be used for comparison. The x-axis of the GSM coordinate system is defined along the line connecting the centre of the Sun to the centre of the Earth. The origin is defined at the centre of the Earth, and is positive towards the Sun. The y-axis

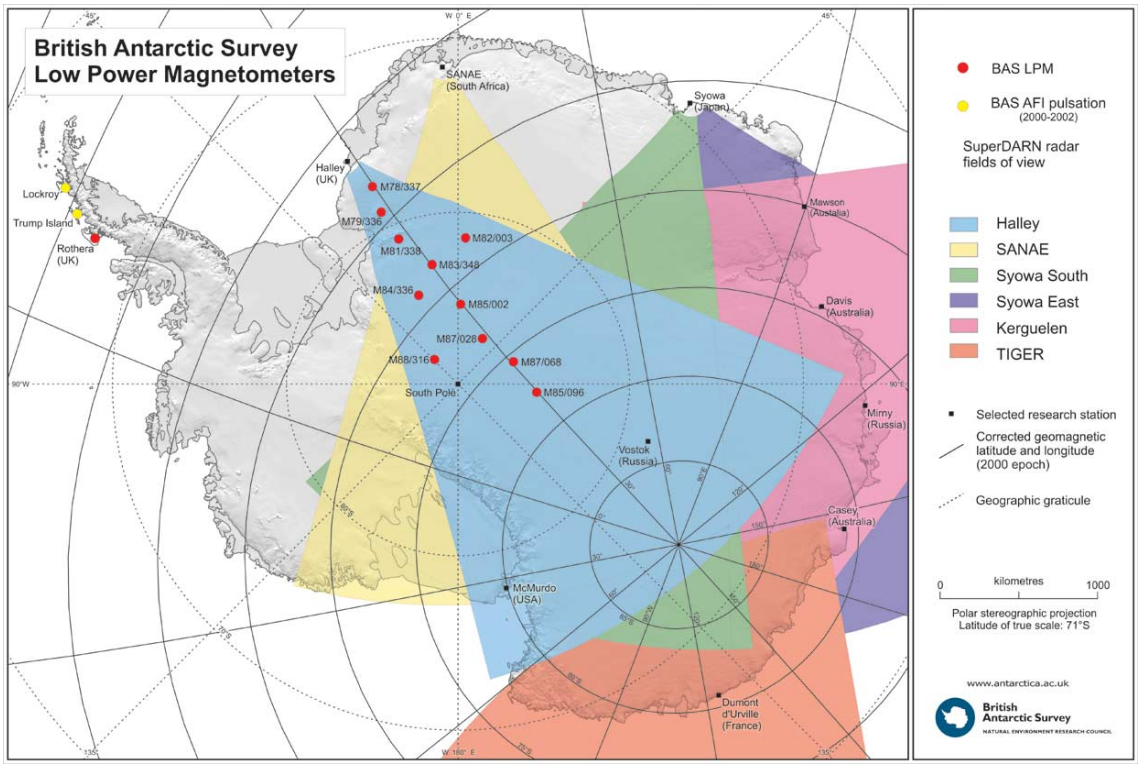

Figure 7.1: The BAS Low Power Magnetometer network (red dots) shown together with the SuperDARN radar's fields of view. [7]

is defined as the cross product of the GSM x-axis and the magnetic dipole axis; directed positive towards dusk. The z-axis is defined as the cross product of the x- and y-axes. The magnetic dipole axis lies within the xz plane.

7.2.1 Solar wind - ACE

To determine the state of the solar wind, use was made of the Advanced Composition Explorer (ACE) satellite data. ACE orbits the L1 libration point which is a point of Earth-Sun gravitational equilibrium about 250 r_e from Earth see figure 7.2.

The interplanetary magnetic field status was determined with level 2 data from the MAG Project [56] and to determine the plasma electron and ion fluxes, use was made of the SWEPAM Project [41] level 2 data.

7.2.2 Geostationary satellites

Use was made of the GOES 12 geostationary satellite [55] to make measurements of the dynamics of the field lines in the equatorial plane. GOES 12 is nominally located at 284°E longitude, see figure 7.3.

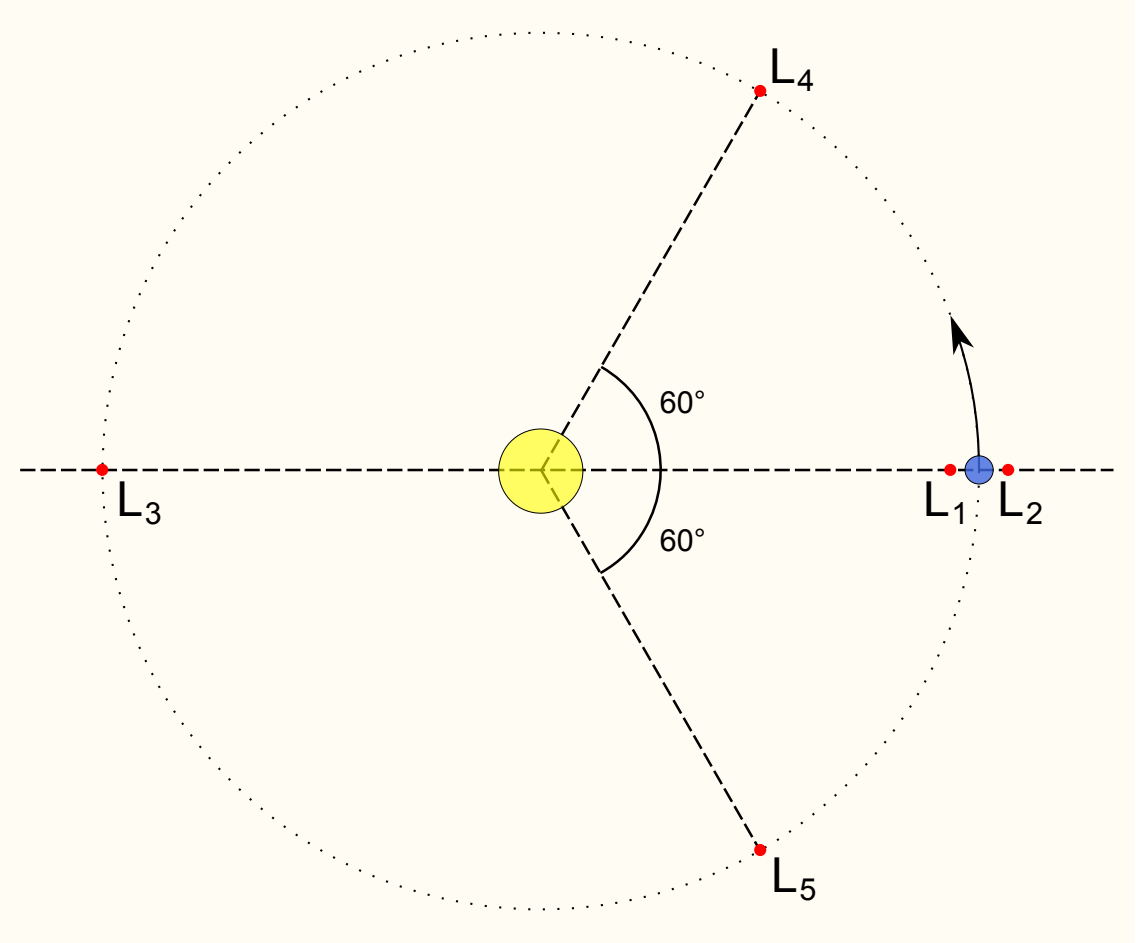

Figure 7.2: The Lagrange libration points. [8]

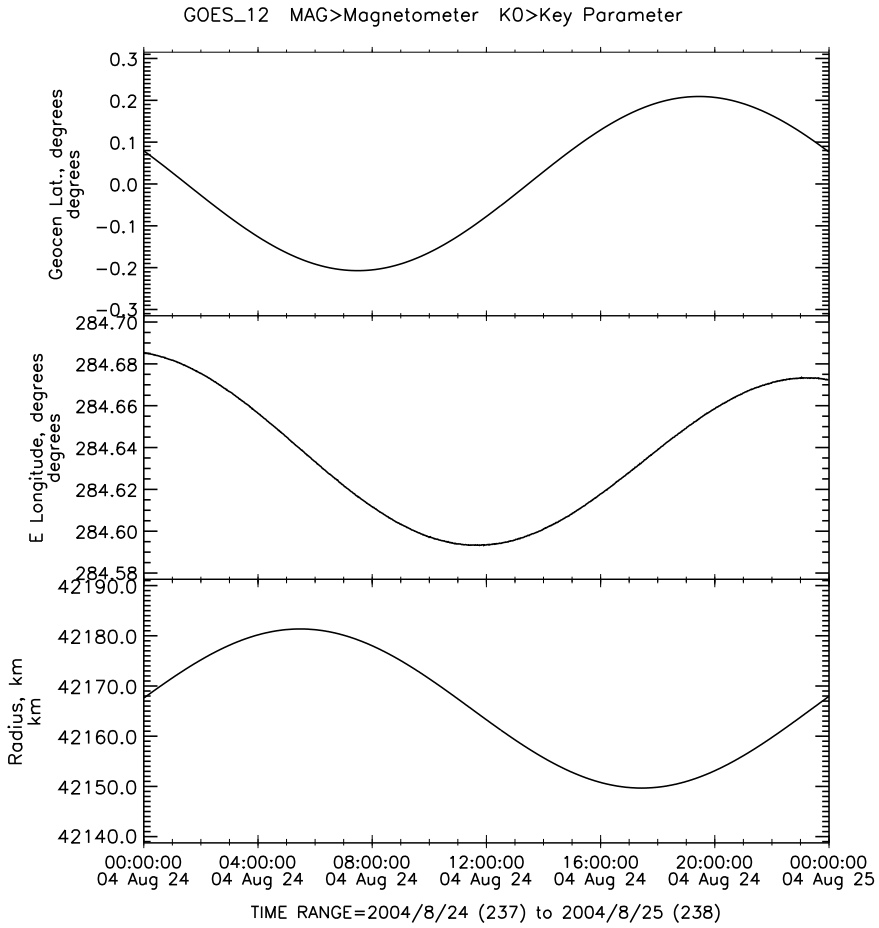

Figure 7.3: The position of GOES12 for 24 August 2004. [2]

7.3 On-line data sources

It is impossible for one signal facility to run, maintain and distribute data from all the instruments that are currently monitoring the space physics environment. To that end most facilities make their data available in a coordinated fashion on the Internet. Extensive used was made of the CDAWeb resource [2] to obtain multi-instrument data for the use of correlating it with the data obtained from the SuperDARN network.

7.4 Storage and analysis devices

A typical FIT file of SuperDARN data is between five and ten megabytes in size. The 2004 FIT data used in this analysis came to more than 300 gigabytes. If one were to store the data for more than one year, as well as the DAT files that contain the ACF data for each range, then the storage capabilities of a standard desktop system are insufficient. The HMO purchased and installed an inexpensive SAN [4] data storage system that provides four terabytes of storage capacity. This storage system is connected to 15 desktop workstations each running IDL. This system makes it possible to process larger quantities of data in a relatively short time which was critical to the analysis outlined in this thesis.

Chapter 8

Significance detectors

8.1 Introduction

Throughout the analysis parts of this thesis a significance detector has been used in various guises. The term significance detector is used to describe a routine that will process a set of data and then return those points that are either a significant part of a data group or not part of a group. In this chapter the discussion focuses on the noise filter used to remove noise from the data and the peak detector used to find peaks in frequency spectra.

8.2 Noise filter

8.2.1 The data

It is assumed that for the data of interest, the physical mechanism that creates the data is coherent. A time series of data points may, however, contain spurious values. These are data values are not correlated with the data. One can thus assume that given a coherent driver, there may still be some random variation in the data values. In this case it is assumed that the data values will be normally distributed around some mean. This is the target distribution of data values. Measured values that, for some reason not associated with the driver, fall outside the target distribution are know as outliers.

An example of the data and their corresponding distribution histograms are given in figure 8.1. This shows the SANAE radar FIT velocity data for beam 2 from 5th August 2002. The velocity is displayed in a waterfall format. The absolute values for the data are not significant so only the relative values are shown. Each line of the waterfall plot represents a range for that beam. The histograms show the number of data values that fall into a certain velocity bin. The velocity bins are shown on the x-axis where the bin size is 1.

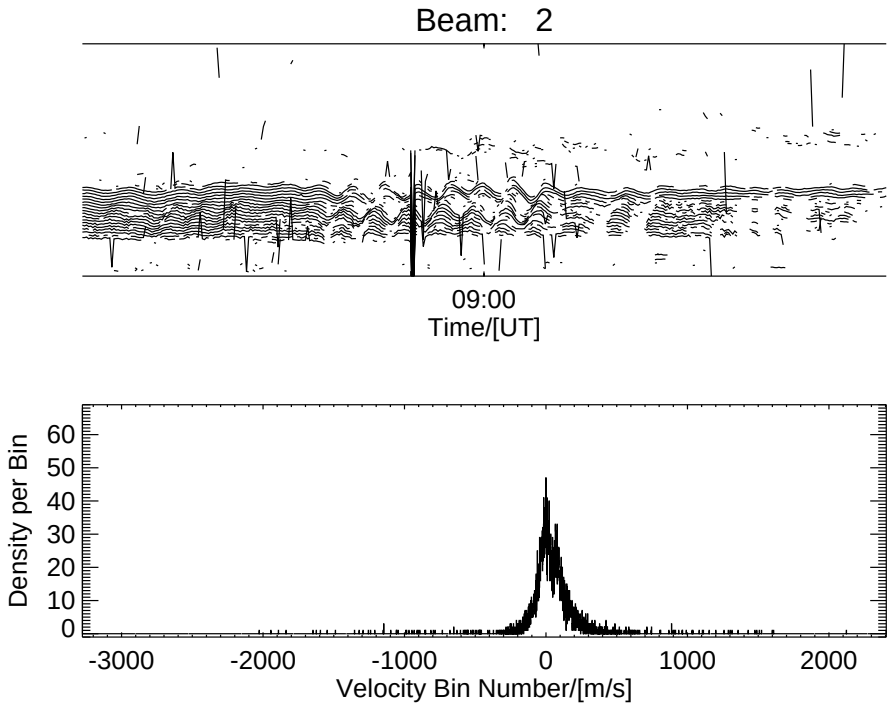

Figure 8.1: Data (top) and distribution histogram (bottom) for the uncleaned velocity data. The velocity data is plotted as a function of range and time. The cumulative distribution histogram is for all the velocity data in the specified beam.

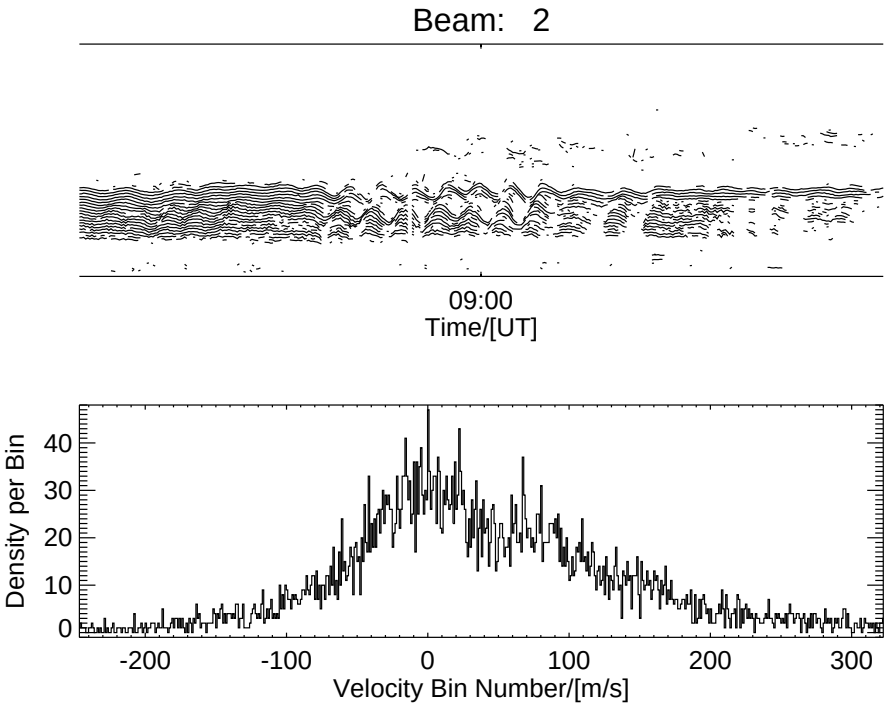

Figure 8.2: Data and distribution histogram for the cleaned velocity data. The format for the panels is the same as figure 8.1.

8.2.2 The method

In a discussion on the identification of multiple outliers [23] Davies and Gather discuss various ways to identify outliers. Based on this discussion, a multi-step process was chosen using the extreme studentized deviate method where given a set X of N values characterised by the mean μ and variance σ^2, the outliers, $x \in X$, are such that

$$|x - \mu| > z\sigma$$

where z is a constant multiplier.

8.2.3 The result

In order to remove the spurious data points, the average and the standard deviation were calculated for each beam. Using the studentized deviate method any velocity value that was greater or less that the average plus or minus three standard deviations was removed. This is a recursive process and was repeated until such time as there were no outliers in the data. The cleaned data can be seen in figure 8.2.

8.3 Peak detector

Samples of a time varying signal can be transformed into the frequency domain by using a variant of the the Discrete Fourier Transform such as the FFT. If the signal is monochromatic the resulting frequency spectrum will have a peak at the frequency of the signal. A real-world pulsation signal will be quasi-monochromatic meaning that it will exhibit both monochromatic as well as broadband or even noise like characteristics. An automated pulsation finder would need to be able to tag a record for analysis if the monochromatic part of the signal were significant.

The velocity data for a specific beam and range are a one dimensional time varying data set. A frequency spectrum can then be calculated for that data. In order to determine if there is a peak in the whole, or part of, the spectrum the mean and standard deviation of all the amplitude values within the window of interest must be calculated. The significance level was then set to be the average plus three standard deviations of the data. If there were any amplitude values in the window of interest that fall above the significance level then the frequency that corresponded to that amplitude was considered a significant monochromatic signal in the group.

An example output of the pulsation finder[1], which uses the peak detector, is shown in figure 8.3.

The two panel plot shows the data in the top panel and the spectrum in the bottom panel. The first panel contains:

1. the original FIT velocity data, with any outliers removed, plotted with the error bars. The errors are the *vel_err* parameter from the FIT process,
2. a filtered version of the original (black) and the re-sampled data (red).

A band-pass filter between 1 and 5 mHz was used for filtering. An alternative upper-limit of 4 mHz was used if the original sampling period was 120 s. The data were re-sampled such that there were 7200 samples in the two hour period (see section 12.2.2).

Both filtered data series were transformed using the FFT process. The significance level was calculated using the amplitude values between 1.0 and 5.0 mHz.

The second panel contains the plotted amplitude values with solid line for the re-sampled data and dotted line for the original data, together with the significance level (red horizontal line). The only value above the significance level in figure 8.3 is at a frequency between 4.0 mHz and 4.1 mHz. This corresponds to the quasi-monochromatic signal in the last part of the time series plot.

It is important to note in figure 8.3 that the spectra for the filtered original data and the filtered re-sampled data are the same. This means that the re-sampling of the original

[1]See chapter 10 for a description of the pulsation finder.

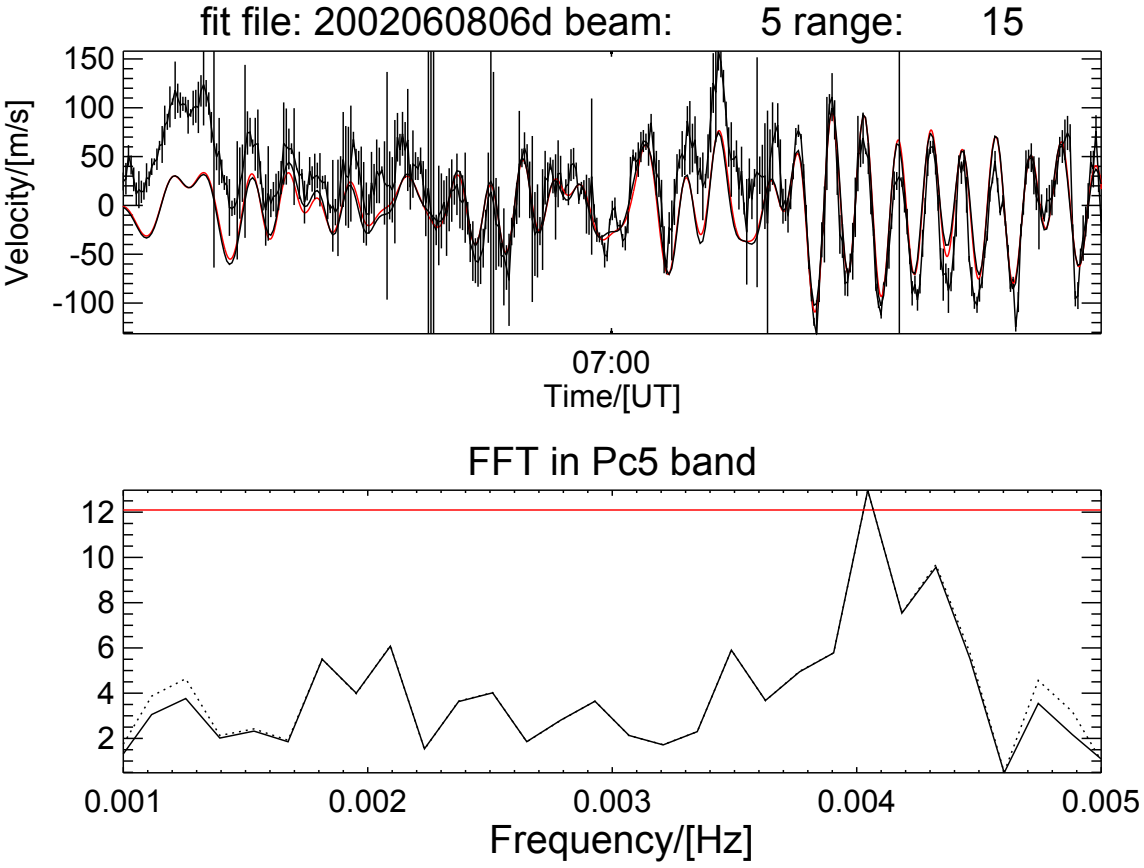

Figure 8.3: The output of the pulsation finder. The top panel shows the raw data and the bottom shows the corresponding spectrum and the significance limit level in red. The peak detector would record the peak between 4.0 and 4.1 mHz as significant.

series does not change the spectrum in our window of interest. This is because the upper limit of our window of interest falls below the Nyquist frequency of the original data.

8.4 Summary

The large data volume that makes up the SuperDARN data set needed to be first cleaned and then searched for pulsation events. In this project, use was made of a significance detector to remove outlying data points and then to detect peaks in the FFT spectra generated from the two hour FIT velocity data.

Chapter 9

Scatter analysis

9.1 Introduction

During the two hour scan period used to create a FIT file, the radar is sampling a region with a range of 3000km and an azimuthal spread of 52° [30]. Every time a beam is scanned an ACF is generated for each range. The FITACF process will then yield the parameters that best fit the ACF and store these in the FIT file. Two models are used to fit the data, the Gaussian and Exponential models (see appendix D). Each fit is tested using the FITACF algorithm to determine if the data for that range are ionospheric scatter, ground scatter or sky noise. If the ACF was determined to be noise, then no data are stored for that range in the FIT file. Thus the main problem in using the SuperDARN FIT data for pulsation studies are that the data contains many gaps. In summary, the gaps are due to that fact that:

1. the FITACF process will not record data for ranges that is has determined to be sky noise
2. the velocity data may contain outliers
3. the radar is observing the auroral regions which contain a significant number of open magnetic field lines. These data cannot be used to study pulsations that are occurring on closed field lines and so is discarded.

These points mean that of all the data that could be stored in the FIT file not all can be used in the pulsation analysis. The question then arose,

"how suitable are the SuperDARN FIT data for pulsation studies?".

To answer this question the data were first checked for cleanliness, where cleanliness is defined as velocity data where;

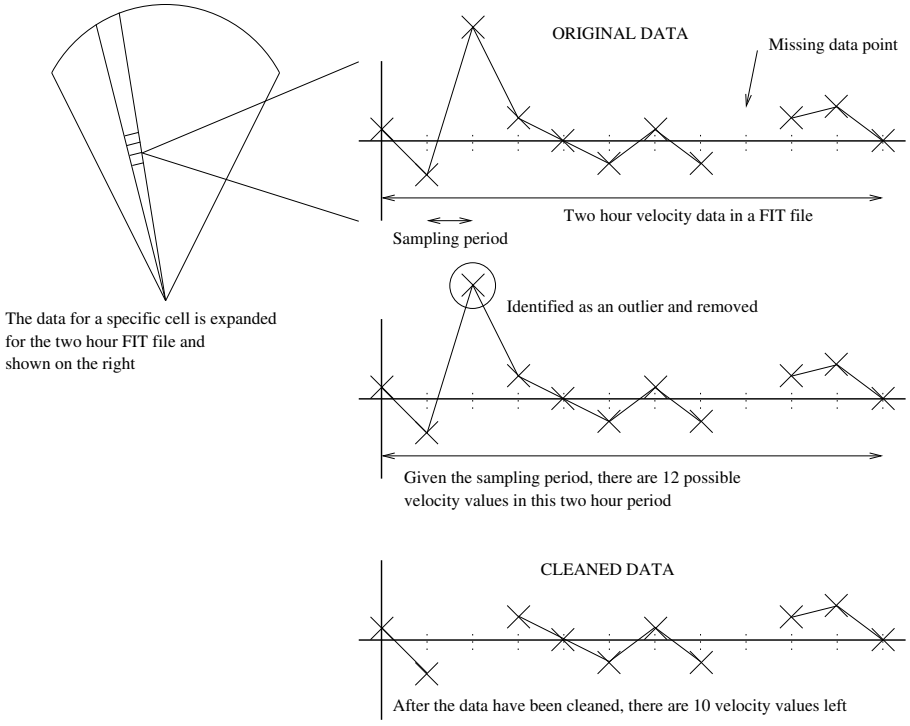

Figure 9.1: A description of what is meant by clean scatter percentage for a specific cell. The percentage is determined by the number of clean data points over the total possible data points in the series.

1. outliers have been removed,
2. echoes with a spectral width of greater than 150 m/s have been removed (see section 10.2.2 for the the choice of this limit)
3. the remaining velocity values fill more than 80% of the two hour cell record

Simply put, this analysis only concerns data that are suitable for the pulsation finder algorithm. The results of the scatter analysis for 2004[1] are presented in this chapter. This work differs from the work of Ruohoniemi and Greenwald, [49], as they looked at scatter that is primarily suited for convection studies.

9.2 The scatter in general

Clean data (see figure 9.1) are data that are not sky noise, are not outliers and have a spectral width of less than 150 km/s. The clean data percentage is then defined as the percentage of data for a specific cell that is suitable for the pulsation analysis. An example of clean scatter percentages is shown for all the radars in figure 9.2[2]. The colour

[1] 2004 data was used in this analysis as it was the first compete year of FIT data available on spinning disk at the HMO.

[2] For a detailed description of this type of plot see appendix E

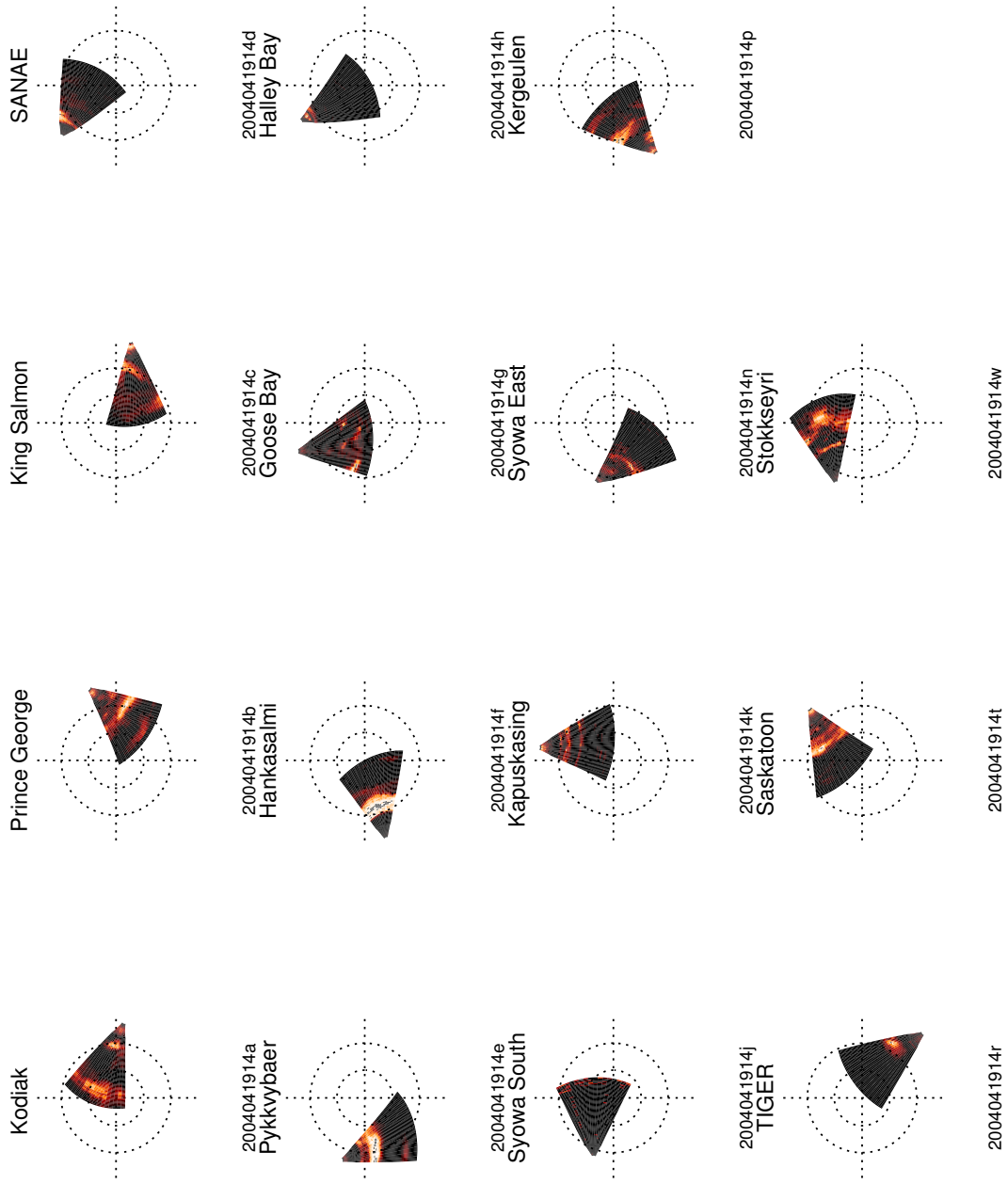

Figure 9.2: The percentage of the scatter considered clean for all the radars in the network between 14:00 UT and 15:59 UT on 19 April 2004. The brighter the colour, the cleaner the data.

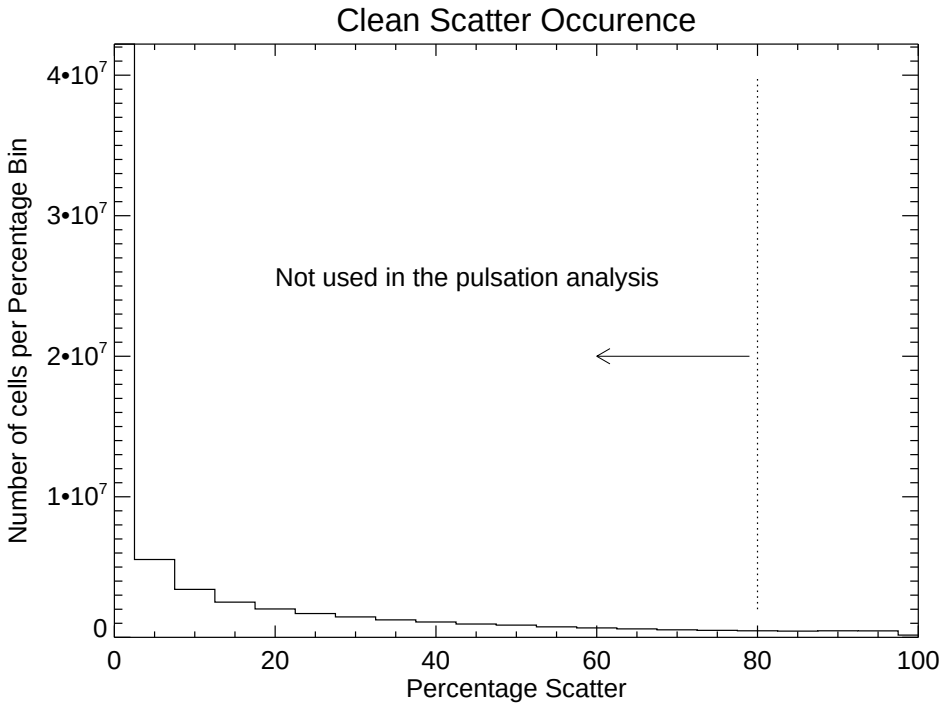

Figure 9.3: The percentage clean scatter occurrence for all the FIT data for 2004. The plot shows how many cells during the year that had a certain percentage of clean scatter. The pulsation finder will only process cells that have at least 80% clean data.

plot represents that percentage of each cell's velocity data that is considered clean for the two hour period. Here you can see that only a small portion of the radar's field of view contains what we call clean data, that is, only a small part of the plotted fields of view contain bright cells. It is reassuring to note that if two radars are observing the same region of the ionosphere that they yield similar scatter characteristics. As an example, the data from radars e and f (Pykkvybaer and Hankalsalmi) are well correlated and looking at the first three plots, radars a, b and c (Kodiak, Prince George and King Salmon), there is a patch of cleaner scatter at longitude 90° west and latitude 70°. Although not exactly conjugate, radar r (TIGER Tasmania) shows a patch of cleaner scatter at longitude 135° west and 70° latitude.

Figure 9.3 shows the distribution of clean scatter percentage out of the total possible scatter for 2004. Here you can see that most of the cells have no clean data with progressively less files having more and more data.

The pulsation finder will only work on cells that have at least 80% clean data. the remaining 20% missing data are interpolated using cubic spline interpolation. One can see that a large portion of the scatter data have been ignored in the analysis. This is a limitation of

	IMF B_x	IMF B_y	IMF B_z
correlation coefficient	-0.03	-0.03	0.32

Table 9.1: The Pearson linear correlation coefficient between the daily percentage clean radar scatter and the daily average of the magnetic component on the ACE spacecraft.

having to use Fourier transforms to determine the spectral characteristic of the data. The FFT approach will only work on data with no gaps. Gaps in the data are filled using a cubic spline interpolation. Other methods of spectral analysis are planned for the future that are able to work with data gaps.

9.3 Temporal variation

In order to determine if there were any temporal factors that governed the amount of clean scatter observed by the radar the clean scatter percentage was analysed through out the year.

9.3.1 Daily Variation

The daily count of cells with clean scatter greater that 80% is shown in figure 9.4 with the total scatter in top panel and the northern and southern hemisphere variations in the bottom two panels respectively. The smooth over plotted line is the output of a low pass filter of the data with an upper cutoff period of 60 days, i.e. only variations with periods longer than 60 days will be evident.

In order to characterise any cyclical behaviour in the data in figure 9.4 a spectrogram was created for the total scatter percentage, i.e. using the data from the top panel of figure 9.4. The spectrogram was created by taking a 128 days worth of data starting on day one. The average of the data was removed, i.e. the zero component of the spectrum. The data were then windowed using a Hanning window and the spectrum was determined using the Fourier transform. The 128 day window was moved on by a day and another spectrum was determined. This was continued for the whole year. The result is shown in figure 9.5 where the central date of the 128 day window is shown on the x axis and the frequency in cycles per day is shown on the y axis. The magnitude of the spectrum is colour plotted with brighter colours indicating a greater magnitude.

Baker *et al* [13] found a increase in Pc5 occurrence in magnetometer data with northward B_z and so to determine if the IMF controlled the amount of clean scatter observed, the scatter was compared to the ACE IMF magnetometer measurements.

The daily average of the various components is shown in figure 9.6. The Pearson linear correlation coefficient was determined between the number of cells that were more than 80% clean and the three IMF components and the results are shown in table 9.1.

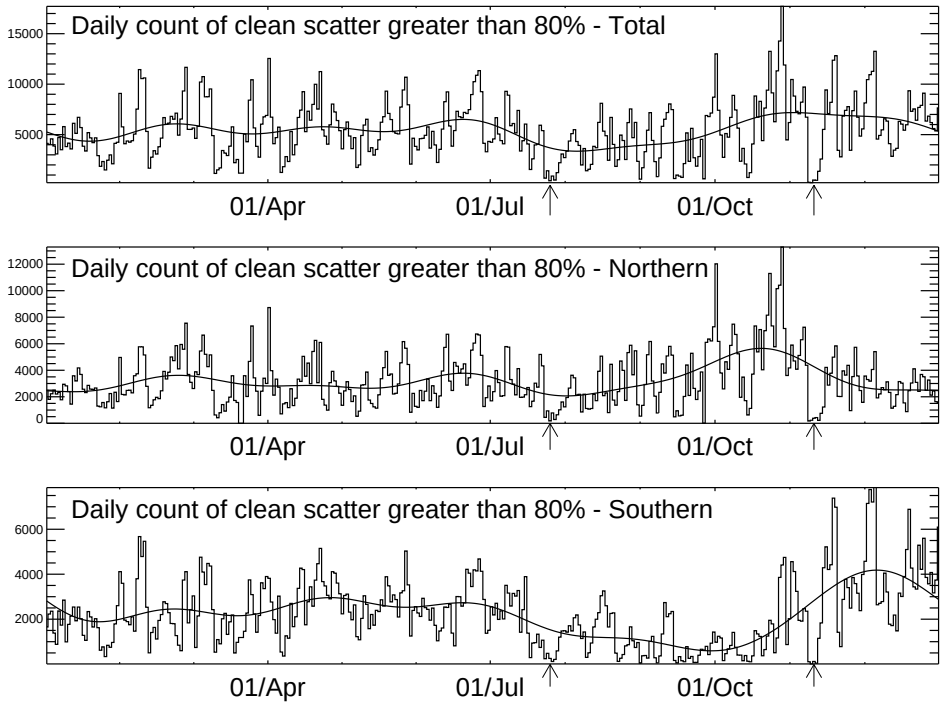

Figure 9.4: A daily count of the number of cells that had a clean scatter percentage of greater than 80% for 2004. The smoothed curve is a low pass filtered version of the data with a cutoff period of 60 days.

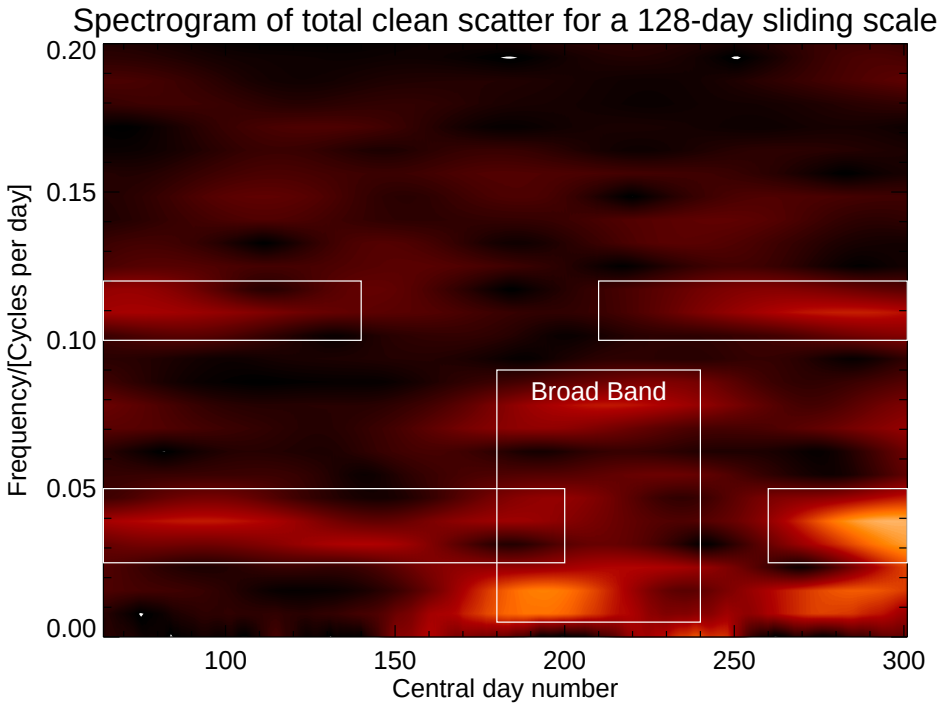

Figure 9.5: A spectrogram of the clean scatter occurrence for 2004.

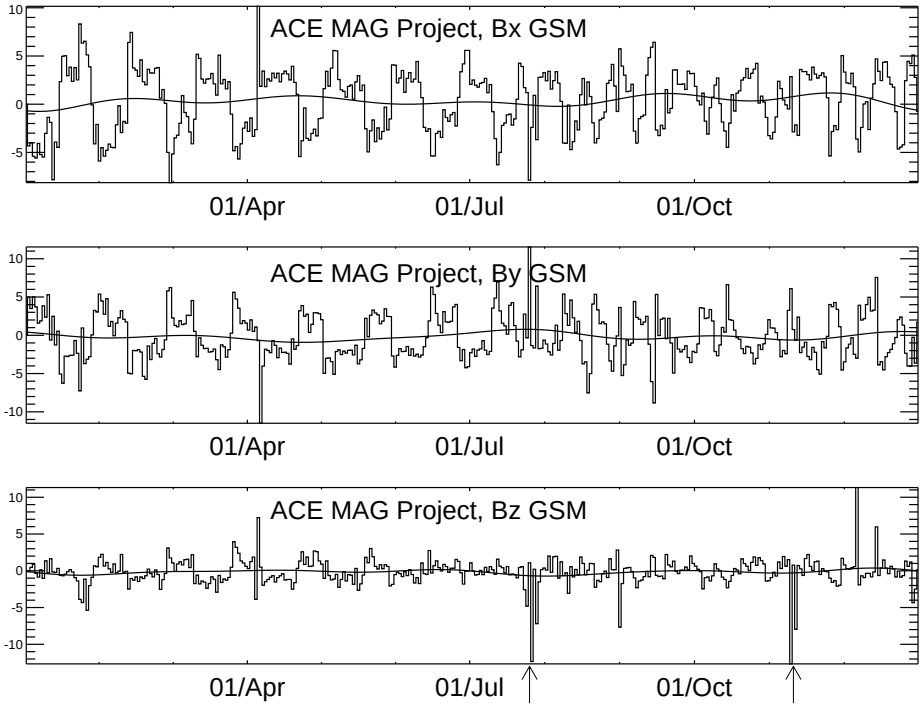

Figure 9.6: ACE IMF daily averages for the three GSM magnetic components. The arrows indicate strong B_z southward.

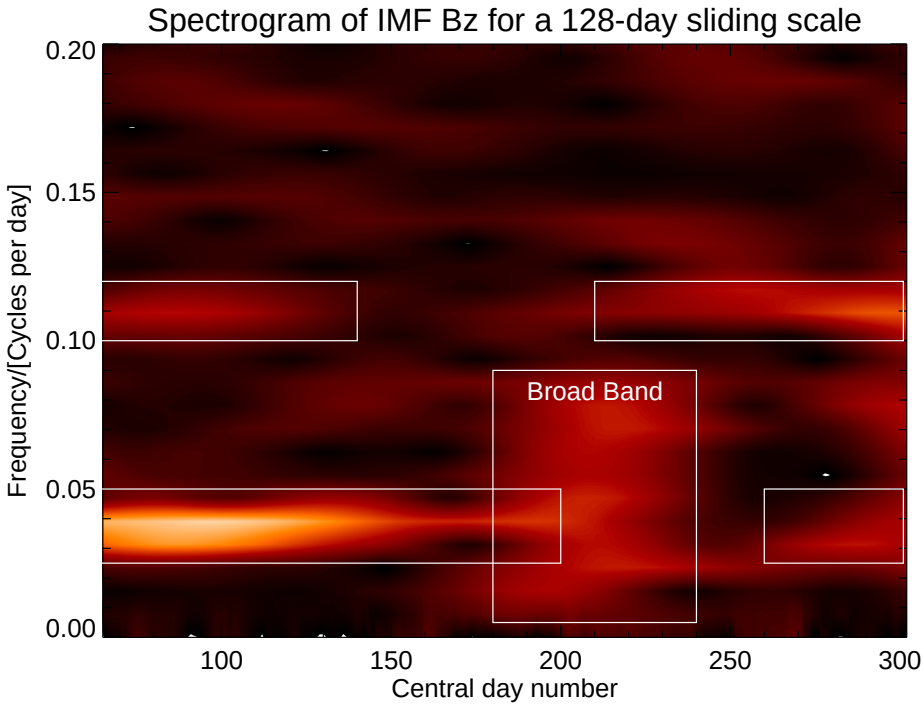

Figure 9.7: Spectrogram of the ACE IMF B_z component.

The best correlation was found to be with the B_z component and so a spectrogram similar to figure 9.5 was produced for the IMF B_z component and is shown in figure 9.7. The white areas are the same as the white boxes in figure 9.4.

Both spectrograms in figures 9.5 and 9.7 show similar characteristics. There is a peak in the spectrograms at 0.039 cycles per day. This corresponds to a period of 25.6 days, roughly equivalent to the solar rotational period. There is also a second peak at twice this frequency. The area labelled broad band in the B_z spectrogram overlaps the peaks in the same area in the scatter spectrogram.

9.4 Locational variation

The number of cells where the FIT velocity data was at least 80% full is shown as a function of radar station in figure 9.8. The antarctic triple (Halley, SANAE and Syowa South) show the least overall clean scatter, while the TIGER Tasmania radar shows the most clean scatter.

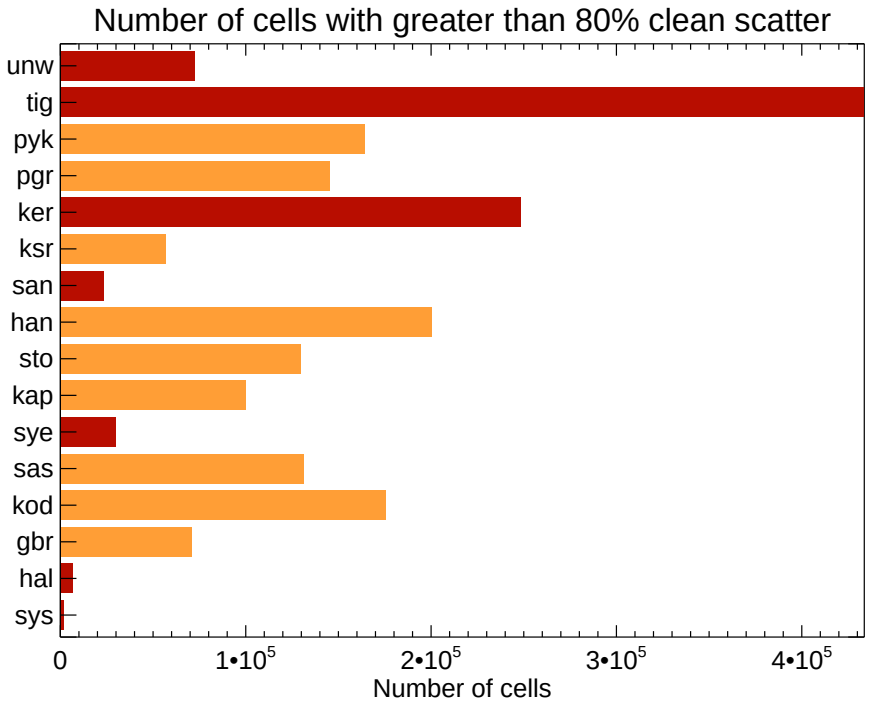

Figure 9.8: The amount of FIT data considered clean shown as a function of radar station. The stations are ordered according to |AACGM latitude| with Tiger Unwin (unw) being the most equatorward. Red are the southern stations and orange are the northern stations.

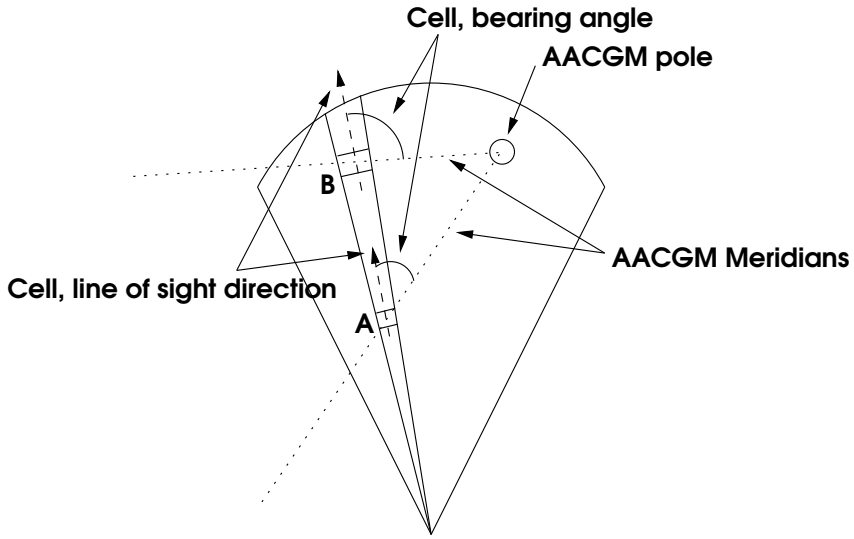

Figure 9.9: The bearing angle of two cells, A and B, in a radar beam given relative to the AACGM pole

9.5 Directional variation

The theory in chapter 5 shows that for driven field line resonant pulsations, the poloidal component of the electric field ($\mathcal{E}_\nu$) should be coupled with the toroidal component ($\mathcal{E}_\phi$) and if so $\mathcal{E}_\nu$ will have a maximum at a specific L-shell when the driven frequency matches the natural resonant frequency of that L-shell. The behaviour of $\mathcal{E}_\nu$ at this L-shell is singular and so it is expected that the amplitude of $\mathcal{E}_\nu$ will be much larger than $\mathcal{E}_\phi$.

In the ionosphere the variation of $\mathcal{E}_\nu$ in the presence of the background magnetic field ($\mathbf{B}$) causes the ionospheric plasma to $\mathbf{E} \times \mathbf{B}$ drift. The motion of the drift will be perpendicular to both $\mathcal{E}_\nu$ and $\mathbf{B}$ i.e. in the toroidal direction (ϕ). The resulting ionospheric plasma drifts cause the irregularities in the ionosphere to drift. The irregularities are the targets for the radar and so the drift will be manifested as a Doppler shift in the radar data.

Field line resonant pulsations will thus be more significant in radar data that is directed toroidally. An understanding of the directional characteristics of the scatter is thus important to determine if the distribution of the events are a consequence of the driving mechanism or just a result of the instrumental characteristics.

9.5.1 The network in general

As a reference, the bearing angle for every cell[3] was determined for all the radars in the network. Although cells may be in the same beam, their location may give sometimes quite different bearing angles. This can be seen in figure 9.9.

One can calculate the bearing angle for each cell in the SuperDARN network. The bearing angle occurrence for all these cells are shown in figure 9.10.

[3]See appendix F for a discussion on how the bearing angle is determined for a cell.

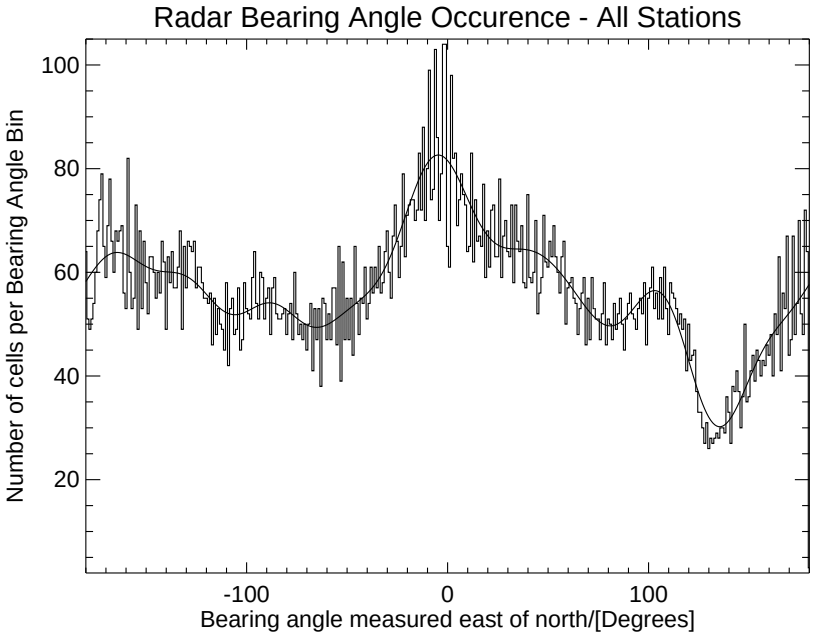

Figure 9.10: The variation in bearing angle for each cell in the network. The solid over-line is a smoothed version of the data.

This figure shows the total number of cells in the entire network with the specified bearing. Here you can see that there is a peak in the distribution at 0° AACGM, meaning there are more cells in the network that point north than any other direction. There is a similar lower peak at ±180°, this is due to the fact that there are less radars in the southern hemisphere than the northern hemisphere. The range of cells with bearing angles away from north and south is fairly constant with a dip between 140° and 150°.

The distribution of bearing angles as a function of hemisphere is shown in figures 9.11 and 9.12. These figures are similar to figure 9.10 except the northern and southern hemispheres are shown separated.

9.5.2 Clean scatter

In order to determine if there are any directions that yield more clean scatter, the distribution of clean scatter was calculated as a function of bearing angle for each cell. If you look at the scatter from the northern hemisphere radars only, see figure 9.13, it is clear that these radars have a preferred bearing angle of 0°, which means that the radar cells that are directed more towards AACGM north will expect to receive more clean scatter. The same is true for the radars in the southern hemisphere, see figure 9.14. Here the preferred bearing is ±180°, so cells directed towards AACGM south will also expect to receive more

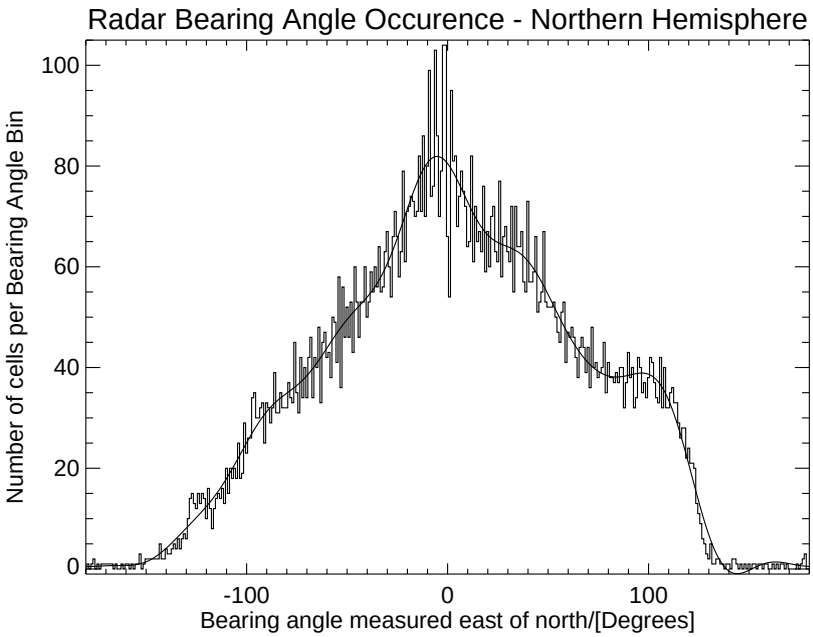

Figure 9.11: The bearing angle distribution for the Northern hemisphere.

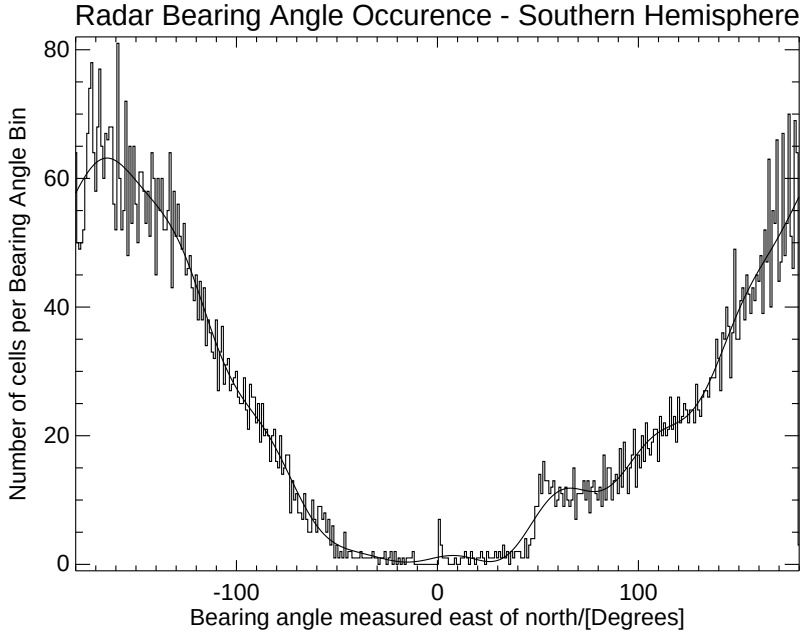

Figure 9.12: The bearing angle distribution for the Southern hemisphere.

clean scatter.

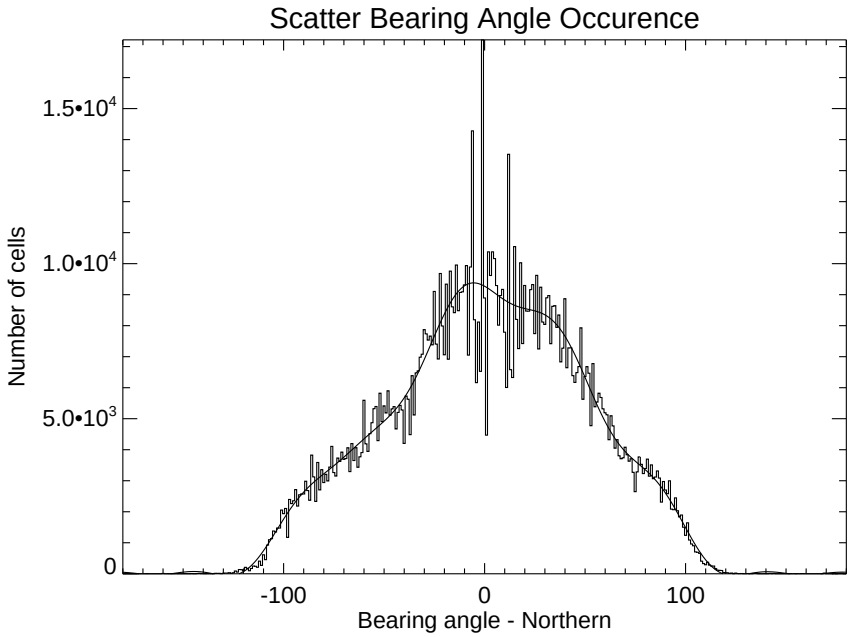

Figure 9.13: Number of cells with more than 80% clean scatter against bearing angle for the northern hemisphere radars.

The distributions in figures 9.11 and 9.13 were smoothed and normalised. The resulting distributions are plotted together in figure 9.15.

9.6 Conclusion for scatter analysis

The reasons for the observed variations in clean scatter have not been discussed in this thesis and will be left for further work. The variations themselves are, however, significant to this thesis because a radar will only be able to observe pulsations if there is clean scatter. A good knowledge of the scatter variations is thus necessary for pulsation event studies to establish if the variations observed in the pulsation events are due to variations in the pulsation driving mechanism or if the variations are caused by the variations in the scatter.

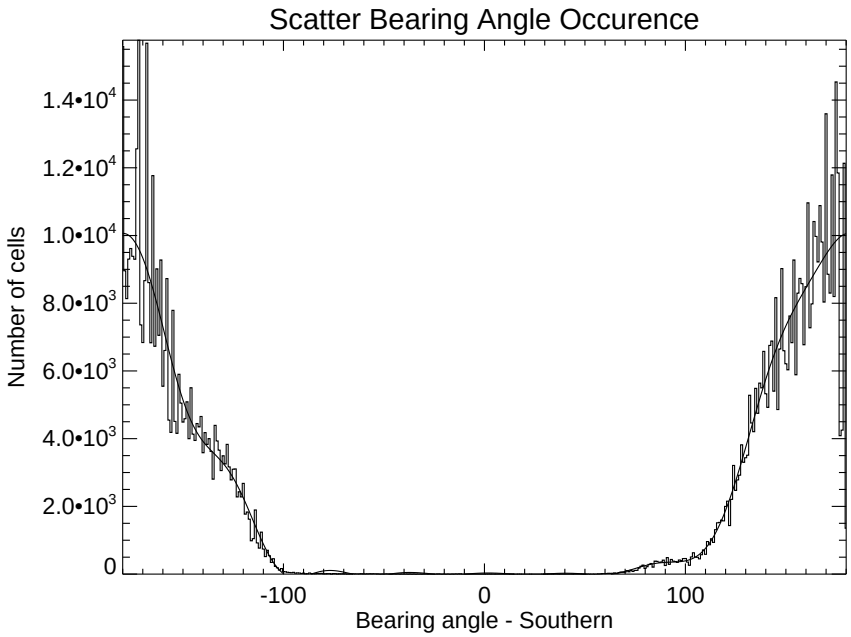

Figure 9.14: Number of cells with more than 80% clean scatter against bearing angle for the Southern hemisphere radars.

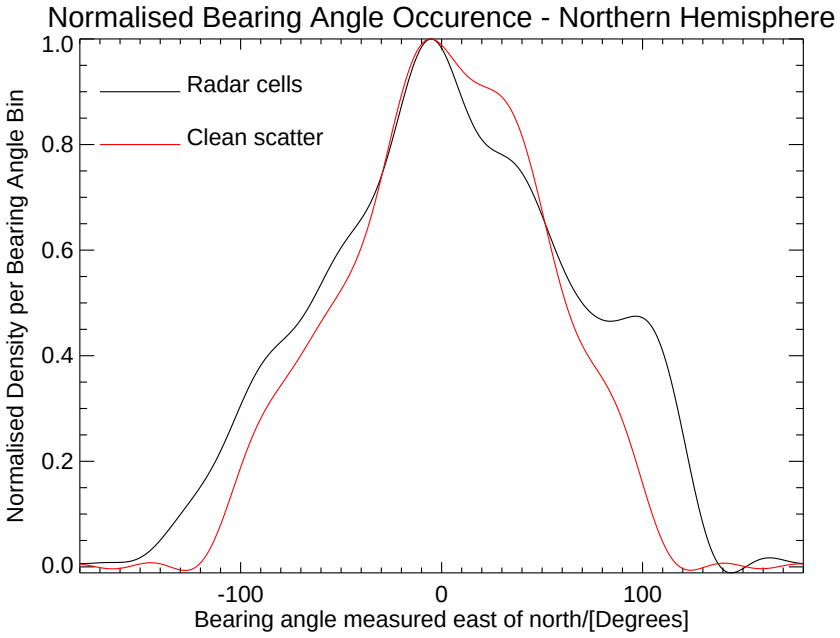

Figure 9.15: Smoothed and normalised versions of the data in figures 9.11 and 9.13. The red curves are the data from figure 9.11.

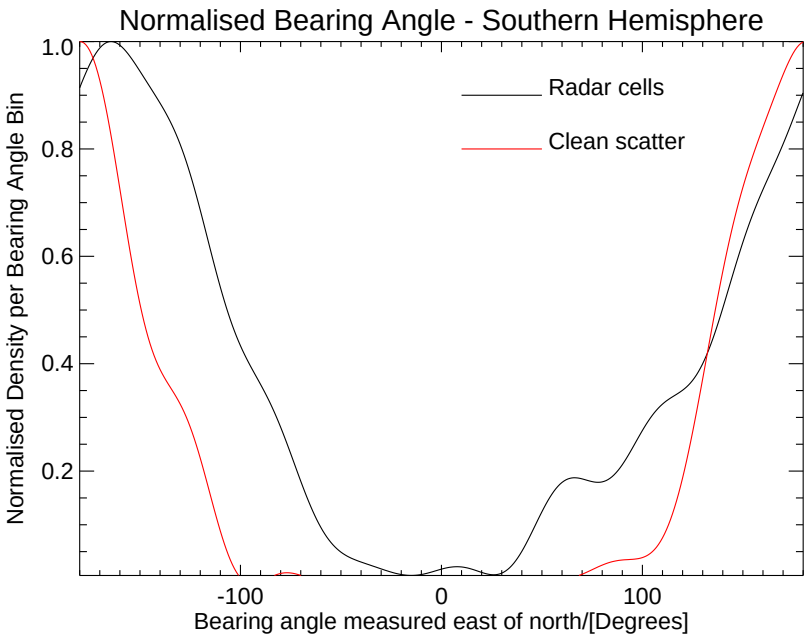

Figure 9.16: Smoothed and normalised versions of the data in figures 9.12 and 9.14. The red curves are the data from figure 9.11.

Chapter 10

The pulsation finder

10.1 Introduction

The SuperDARN radars observe ionospheric motions due to electric fields in the ionosphere. Pc5 pulsations have a zero order node of electric fields in an infinitely conducting ionosphere and so the radars would not be able to observe the pulsations. The ionosphere is not infinitely conductive with the result that there is a first order correction to the electric field perturbations such that there are measurable pulsation electric field in the ionosphere. These pulsation electric fields will cause the ionosphere to $\mathbf{E} \times \mathbf{B}$ drift. These drifts are manifested in the radar data as perturbations in the measured Doppler shift velocities. An example of a pulsation event measured by the SANAE SuperDARN radar is shown in figure 10.1. In this figure one can see how for a specific range the velocity data, panel 2, varies sinusoidally with time.

The challenge for any pulsation analysis of the SuperDARN data is to locate these events. The SuperDARN FIT data[1] is used as the primary data source for this analysis. The focus of this chapter is the automated pulsation finder that is used to locate pulsation events in the SuperDARN data. The data is first cleaned then the finder algorithm is applied to the data.

10.2 Data cleaning

The data cleaning is a two step process. First noise is removed from the data then all non-suitable radar scatter is removed.

[1] For a description of the FITACF process see appendix D.

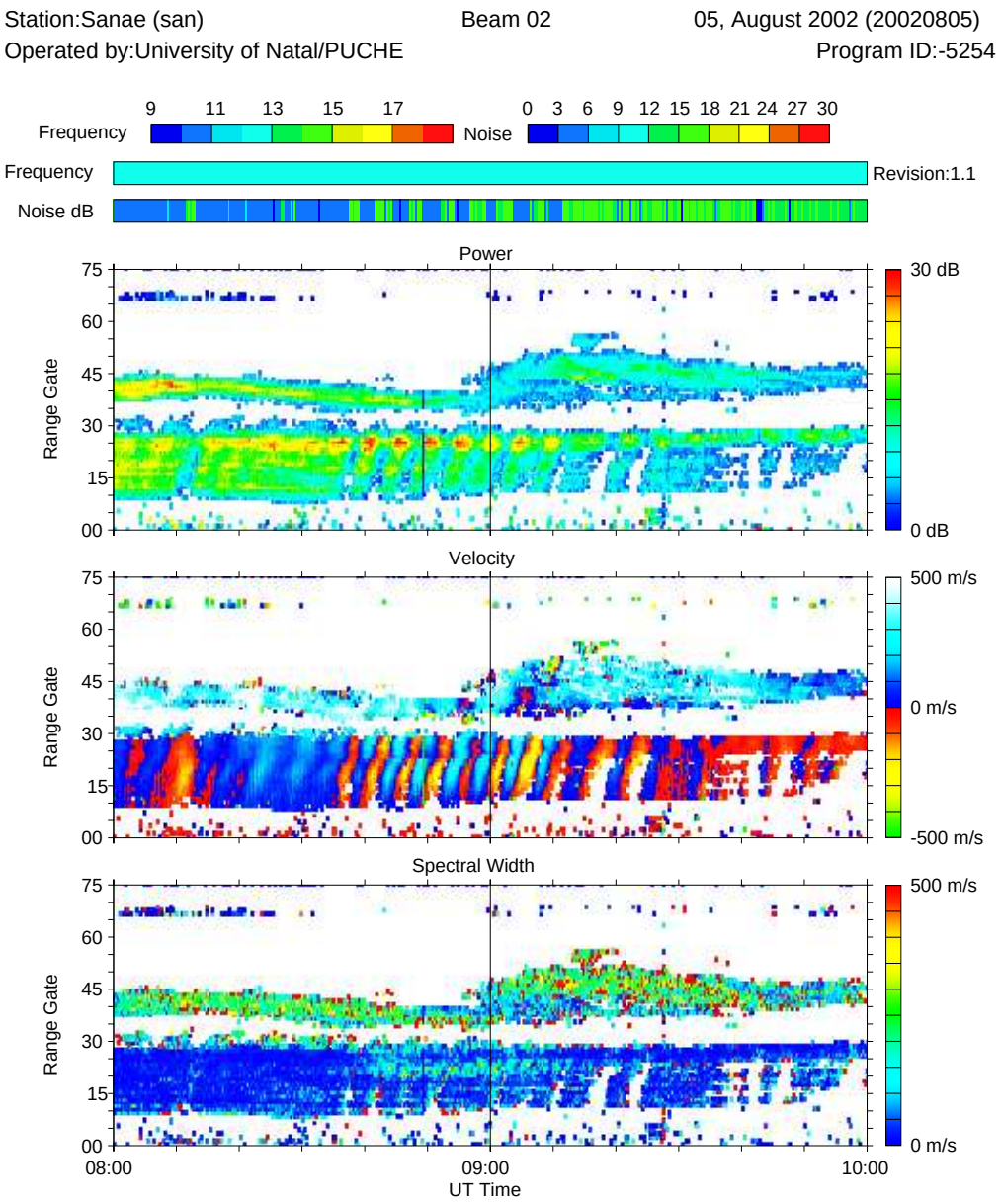

Figure 10.1: An example of Pc5 pulsations observed in the radar data. The measured electric fields are manifested as the velocity perturbations seen in the second panel. [6]

10.2.1 Noise

A noise filter (see section 8.2) was used to remove spurious data points. The noise limit was determined by taking the average of all the data points ± three standard deviations. If a value was greater or less than the noise limit it was discarded. The process was repeated until there were no outliers.

10.2.2 Closed field lines

As was seen in theory sections, the field lines of interest for pulsation studies must be closed. Work has been done [20] using the SuperDARN Spectral Width parameter to determine the location of the boundary that separates open and closed field lines. A spectral width of typically less that 150 m/s can be used to indicate that the radar scatter is coming from irregularities that are on closed field lines. Since the radar data is being used to study pulsations, records with a spectral width of greater that 150 m/s were excluded from the analysis.

10.2.3 Ground scatter

Ground or sea scatter was *not* excluded from the analysis as it has been shown that pulsations may be visible in such scatter [45].

10.3 Pulsation finder

The radar produces a FIT file every two hours, that means every two hours there are $16 \times 75 = 1200$ possible two hour data series that may contain a pulsation event. In order to objectively analyse each data series an automated pulsation finder was developed. The algorithm works as follows

1. Clean the data
2. Check how full the data series is. (See figure 9.1 for a description of how the percentage scatter is calculated.)
3. If the data series is less that 80% full then move onto the next data series.
4. For each series that is 80% full, interpolate the missing points using cubic spline interpolation.
5. Re sample the data series so that there are 7200 points in the two hour interval. See section 12.2.2 for the rational behind the choice of 7200.

6. Filter the re sampled between 1mHz and 6mHz data using a windowed filter based on the Kaiser's window [43, Sec 7.4.3].
7. Create a spectrum of the filtered data using the IDL FFT routine.
8. Use the peak-detector described in section 8.3 to determine is there are any significant peaks in the spectrum in the band of interest.
9. If there is a significant peak;
   (a) create a log entry in the log file,
   (b) generate a Postscript plot of the data and the spectrum
   (c) move onto the next data cell and repeat.

This process can be left to run on historical FIT data sets. The pulsation finder log file contains the following;

1. The FIT file name
2. The radar beam number
3. The radar range cell number
4. The AACGM magnetic local time for the range cell
5. The AACGM latitude for the range cell
6. The frequency of the peak in the spectrum
7. The amplitude of the peak in the spectrum
8. A flag to identify contiguous cells

The pulsation events used in this analysis were chosen based on the fact that the pulsation finder tagged contiguous ranges and beams. Events with only one range or non contiguous ranges or beams were ignored. This was done in order to limit the analysis to events where the spatial variation of the event could be mapped. Single records do not allow for the determination of the spatial characteristics of the driver required to identify a pulsation as field line resonant.

10.4 Summary

Due to the shear volume of data produced by the SuperDARN radar network an automated pulsation finder algorithm was created to search through the SuperDARN FIT velocity data to identify pulsation events. Not every velocity data point measured by the radar is

valid and this introduced gaps into the data series. The FFT approach that was used to calculate the spectra of the data requires that the data series contains no gaps. Data that was less that 80% full was thus excluded from the analysis while data that was greater that 80% full was interpolated and analysed using FFT time series techniques. Spectra that contained significant peaks were tagged as pulsation events.

Chapter 11

Pulsation finder results

The pulsation finder discussed in section 10.3 was used to process all the cleaned FIT data for 2004, and the overall pulsation occurrence statistics are shown. The pulsation occurrence statistics are then compared with the scatter analysis to determine if any of the significance in the pulsation occurrence is a result of the pulsation driving mechanism or simply instrumental characteristics.

The FIT data for 2004 was loaded onto the SAN data archiving system at the HMO taking up 270 gigabytes of storage. An IDL finder program was run on twelve individual workstations linked to the SAN. With the workstations running concurrently it took took 3 days to process all the data.

The pulsation finder would load a specific FIT file and process each beam individually. The FIT file contains the output of the FITACF routine for a two hour period. For a specific beam there are 75 ranges and the number of data points for each range is determined by the integration time of the ACF as well as the radar scanning program.

11.1 Global pulsation analysis

The longitudinal and latitudinal spread of Pc5 pulsations are varied. Smaller structured field line resonance pulsations can occupy a few degrees of latitude ([72], [67], [73] and [51]) while other Pc5 pulsations can be observed at almost all latitudes ([65] and [39]). Pulsations have also been observed across large spans of magnetic local time ([54] and [13]). The global analysis served to confirm if the radar network was suitable for characterising the longitudinal and latitudinal spread of Pc5 pulsations.

For events to be considered in the global analysis, they must first be selected by the pulsation finder. For a specific beam this involved taking the time series from each range and applying the algorithm from section 10.3 to determine if there were any significant Pc5 band frequencies present in the time series. If there was a significant peak then that range is classed as having an event. Only events which were in contiguous range cells

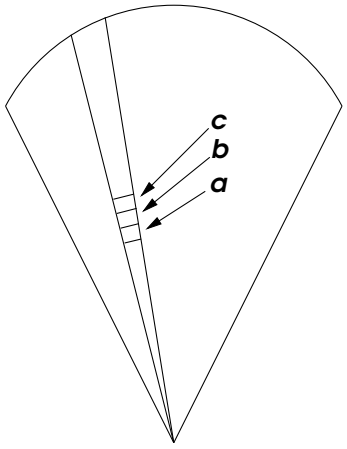

Figure 11.1: Contiguous range cells in a specific beam used to identify pulsation events.

for a specific radar beam were used in the statistical analysis. Figure 11.1 shows three contiguous ranges for an arbitrary beam. The pulsation finder would have processed each range in the beam. If the finder found events in ranges a and c then the events were ignored. If the finder found events in ranges a and b or b and c then they would have been included in the analysis. The reason for this selection criterion was to only target events that could be used to give the spatial variation of the pulsation event. Single range cells can provide information about the location of the pulsation but cannot be used to determine longitudinal or latitudinal variations in the pulsation characteristics.

Given the possible spread in latitudinal and longitudinal manifestations of Pc5 pulsations, together with the variation in magnetic bearings of the various radar beams, there is no physical reason for a pulsation to be so extremely localised that it appears in adjacent beams but does not appear in contiguous ranges.

11.1.1 Discussion

The number of contiguous cells per FIT file were counted and the distribution is shown in figure 11.2. The plot was clipped at 130 on the y-axis to highlight the lower end as there were more that 1600 files with only one set of contiguous cells. It is clear from this figure that there are only a few files with many contiguous cells. All the files that had more than 20 sets of contiguous cells (36 in total) were visually inspected and those that showed good latitudinal spread are listed in table 11.1. The maximum number of contiguous cells in one FIT file is 67 out of a possible 1200 cells. This is only 5.6% of the total radar coverage area. The 20 contiguous cells limit chosen here gives only 1.7% coverage.

11.1.2 Conclusion

The pulsation finder, as it currently exists, was not able to identify enough events that have the large spatial coverage needed to instantaneously map the latitudinal and longitudinal

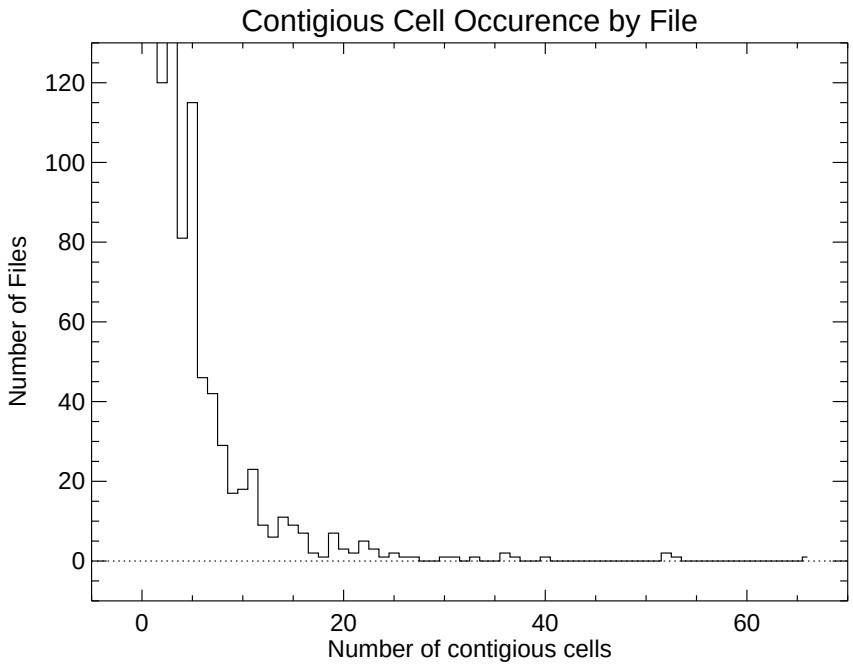

Figure 11.2: The number of FIT files with the corresponding number of contiguous cells in the file.

File Name	Number of contiguous cells
2004042310p	67
2004062508n	54
2004040220d	27
2004093008c	25
2004012206f	21
2004120114w	21
2004120512a	20

Table 11.1: Files that have the most contiguous cells and good latitudinal coverage.

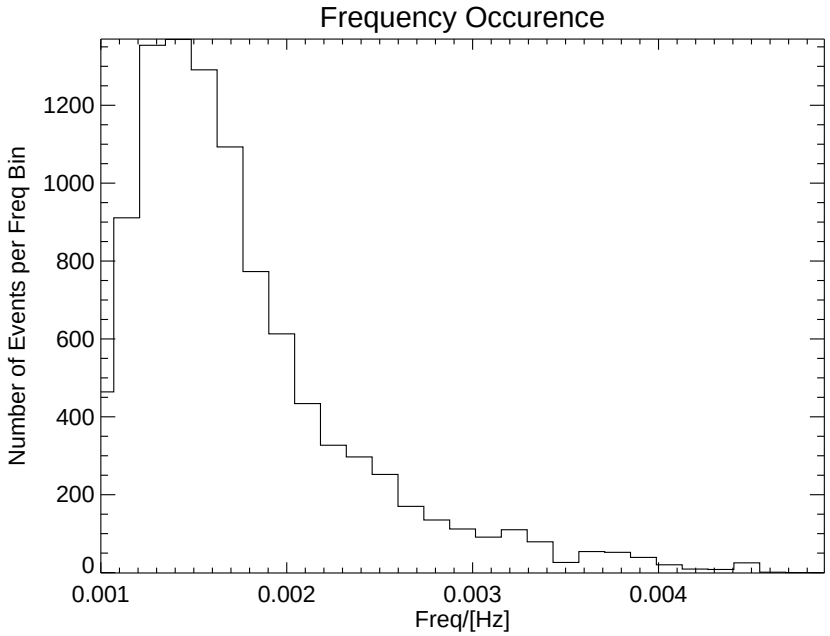

Figure 11.3: The distribution of frequency occurrence for the events in 2004.

phase and amplitude variations. These are the variations that would be needed to better understand the source and propagation characteristics of the pulsation energy. Events that had the most spatial extent, i.e. those with more than 20 contiguous cells, were often isolated in time and space. It was thus rare to observe a large number of pulsation events in different radars at a given time or at sequential times in the same radar.

The SuperDARN network was chosen for this analysis because of its large spatial coverage but such low pulsation coverage made it difficult to infer global dynamics. It was thus felt that the events identified by the pulsation finder should be analysed in isolation rather that trying to determine global spatial pulsation dynamics.

11.2 Frequency distribution

In order to determine if there were any dominant frequencies occurring during the year, a frequency occurrence plot is shown in figure 11.3. This plot shows the number of events that occurred during the year for each frequency band. The plot shows a peak at 1.4mHz and no other significant peaks. The plot follows a typical $1/f$ distribution with the low frequency roll off caused by the Pc5 band pass filter.

The individual daily frequency occurrence could differ from the total behaviour shown in figure 11.3. This was seen, for example, by taking the frequency distribution for day

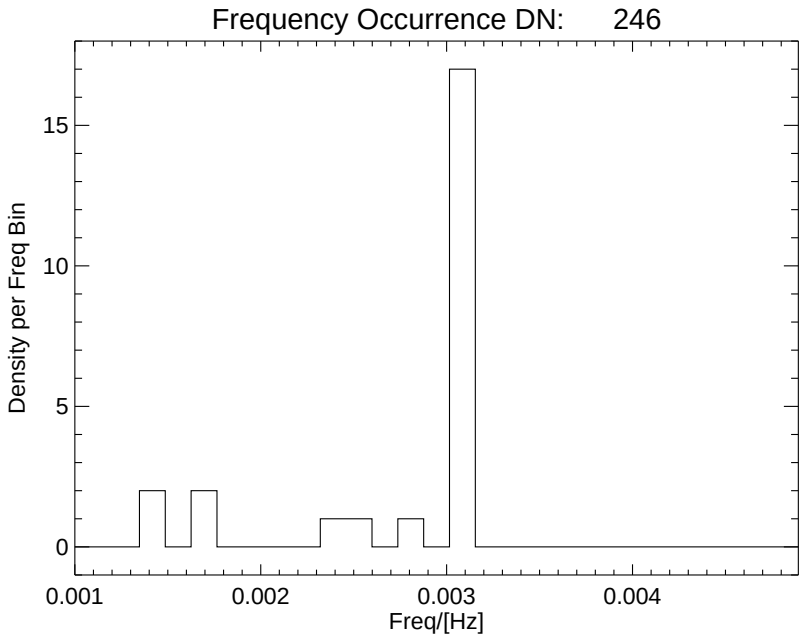

Figure 11.4: The frequency distribution for day number 246 (2 September 2004).

number 246, and is shown in figure 11.4. It was clear that there were a number of event occurrences at 3.1mHz. In order to account for this difference, the frequency distribution was calculated for each day in 2004. The daily occurrence was then averaged over the year and the average and the standard deviation are shown in figure 11.5. Again this plot shows the $1/f$ behaviour with the low frequency roll off, but the standard deviation does not vary smoothly. A plot of the standard deviation on its own, as in figure 11.6, shows there are clear peaks in the underlying distribution. The peaks in frequency occur just below the set of "magic" frequencies given by Samson *et al* [52].

11.2.1 Discussion

The variations in the frequency distribution show that although on average there are no distinct preferred frequencies, there are however certain bands where there is an increased occurrence in that band at some time during the year. This led to the larger standard deviation for those bands. In order to investigate the significance of these peaks they were isolated by first taking the data from figure 11.6 and removing the $1/f$ trend. 6 peaks were identified at 1.3 1.7, 2.5, 3.2, 3.8 and 4.5 mHz. The 1.3 mHz peak is attributed to the low pass cutoff and was not investigated. Table 11.2 shows the details of the remaining peaks. The columns of table 11.2 are arranged as follows:

1. The peak in the standard deviation plot of figure 11.6.

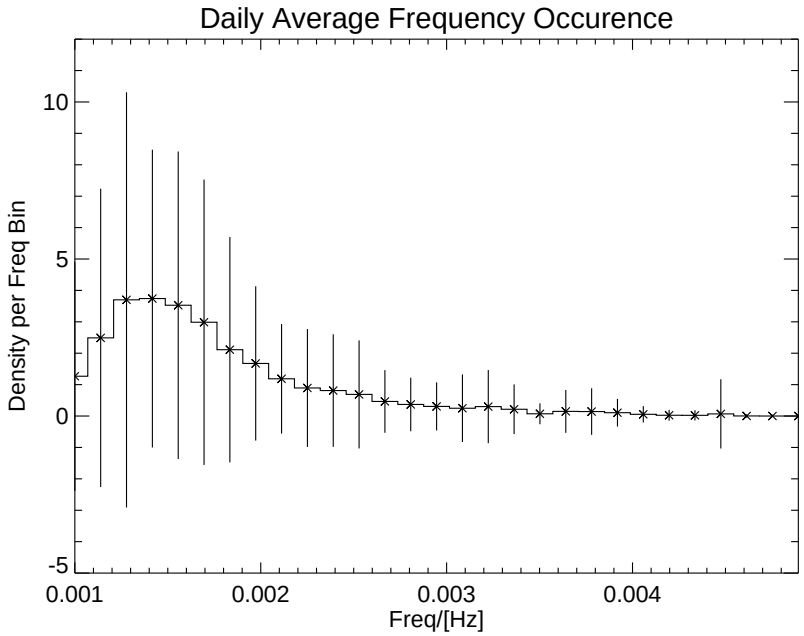

Figure 11.5: The average of the daily frequency distributions for 2004.

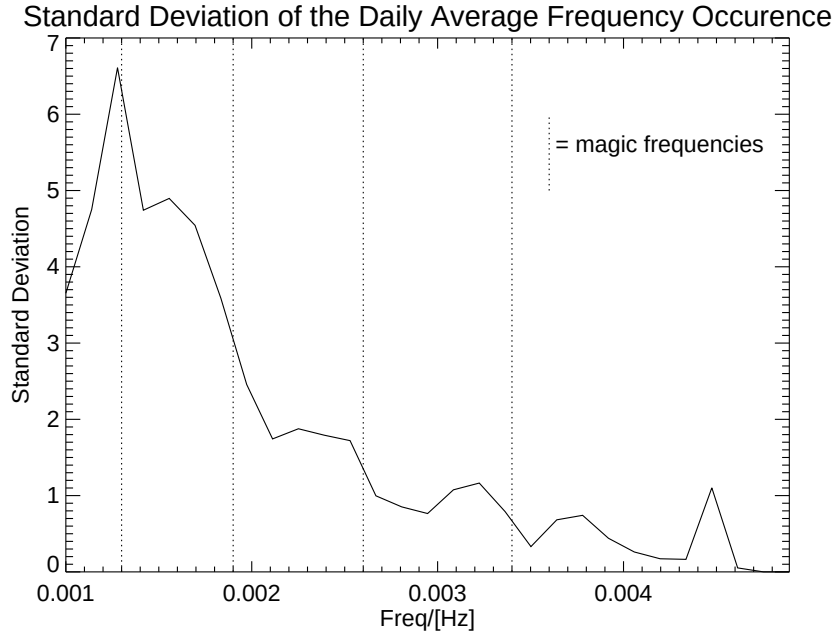

Figure 11.6: The standard deviation of the average of the daily frequency distribution. The location of the "magic" frequencies (1.3, 1.9, 2.6 and 3.4mHz) are also shown[52].

Freq Band/[mHz] (1)	Number of events (2)	Number of files (3)	File name (4)
1.7	1093	10	2004042310p
2.5	252	2	2004120114w
3.2	110	1	2004120512a
3.8	52	0	2004040500t
4.5	25	1	2004012206f

Table 11.2: Details of the peaks in the standard deviation plot of figure 11.6. The columns are numbered and are discussed in the text.

2. The number of events in the entire pulsation event set that fell in that band.

3. The number of files in the band that contained more than 20 contiguous cells. There are, in total, 14 files in these bands. This accounts for 39% of all the files that contain more than 20 contiguous cells. It has been shown in section 11.1.1 that files with more that 20 contiguous cells are rare. With 39% of the files falling in these 5 bands and the remaining 61% falling in the remaining 50 frequency bands there is a ratio of 6.5:1 for these bands to contain files with a large number of contiguous cells. This means that there is a 6.5:1 chance that a file with a large number of contiguous cells will be in one of these bands.

4. The file that contained the most contiguous cells in that band. All files are also listed in table 11.1 apart from the file with the 3.8 mHz pulsation. This is due to the fact that in this band the largest number of contiguous cells was 13 and is below the 20 cutoff for table 11.1.

11.2.2 Conclusion

There exists a $1/f$ distribution of pulsation frequencies similar to that found in Plaschke et al [44] with no distinct peaks also found by Baker et al [13]. The standard deviation of the daily average did show peaks. From the analysis of column 3 of table 11.1 we conclude that the peaks in figure 11.6 are due to the fact that the events that fall into these bands are often from times with a large number of contiguous cells. There is a 6.5:1 chance that a file with more than 20 contiguous cells will be in one of the bands outlined in table 11.1. When a daily average is taken for the year, these highly contiguous events are significantly different from the rest of the distribution and thus result in the peaks in the standard deviation.

11.3 Temporal variations

A five day running mean of the occurrence of events as a function of day number is shown in figure 11.7. The three panels show the total occurrence, the northern hemisphere occurrence and the southern hemisphere occurrence. There are two days (see the arrows)

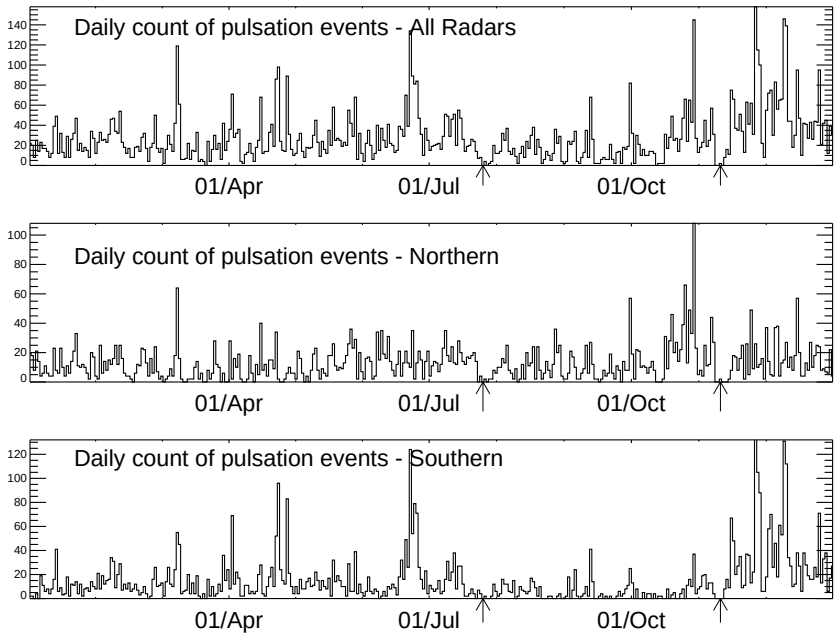

Figure 11.7: The occurrence of events as a function of day number. The arrows indicate days that are discussed in the text.

where there were no occurrence events at all in both hemispheres namely the 25th of July and the 10th of November.

11.3.1 Discussion

In order to determine if the amount of clean scatter limited the number of pulsations observed, the clean scatter was correlated with the daily pulsation occurrence and figure 11.8 shows that the higher the number of clean cells that is observed by the radar, the higher the number of pulsations observed in a day. A scatter plot, figure 11.9 , showed that the best straight line fit had a slope of 0.691 ± 0.043 indicating a shallower than unity slope. The shallower slope indicates that that as scatter decreases so the number of observed pulsations decrease faster.

It has been reported in Baker et al [13] that there were an increased occurrence of Pc5 pulsations in magnetometer data with northward B_z. If one has a look at the ACE on board magnetometer in GSM coordinates you can see in figure 11.10 that the times of low occurrence in figure 11.7 correspond to times of southward directed IMF as well as times of low clean scatter in figure 9.4. This indicates that southward directed B_z yield less pulsations possibly confirming that non-north B_z yields less pulsations.

The Pearson correlation coefficient was calculated for a correlation between the number of

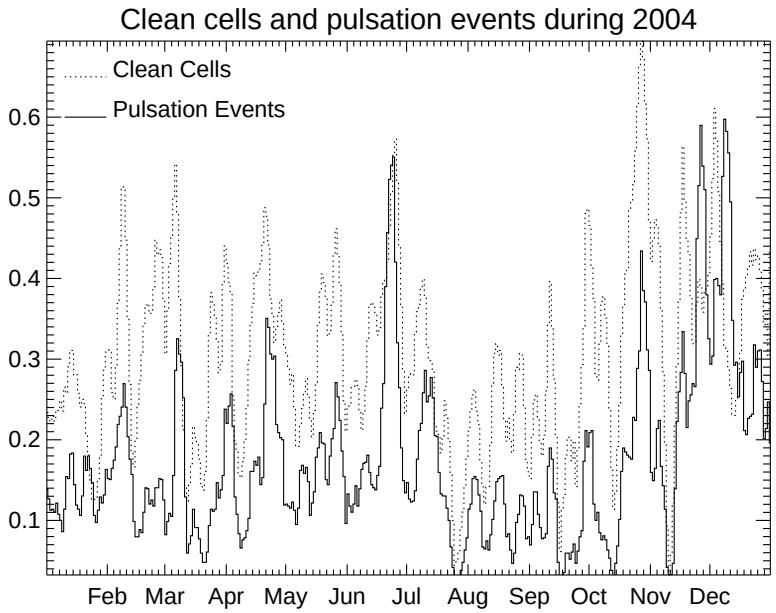

Figure 11.8: Correlation between the amount of clean scatter on a day to the number of pulsation events on that day.

clean cells and the 3 IMF components. There was a larger correlation between the clean scatter and the B_z component than any of the other two components, see table 9.1. This correlation indicates the amount of clean scatter is influenced by B_z, with southward B_z yielding less clean scatter. It follows then that in this case variations in the pulsation characteristics are actually a consequence of the scatter variations and are not directly IMF driven.

An attempt to remove the temporal scatter characteristics from the pulsation characteristics by deconvolving the scatter from the pulsations yielded a data set with no discernible characteristics and is thus not included.

11.3.2 Conclusion

It has been shown that the temporal variation in the pulsation characteristics followed the amount of clean scatter. The shallower slope of the best fit line also indicated that as scatter decreased so the number of observed pulsations decreased faster. Similarities between the pulsation characteristics and IMF magnetic field characteristics were attributed to scatter variations rather than a direct driving of the pulsation. Attempts to remove the scatter characteristics from the pulsation data were not useful. A temporal analysis of the pulsation events only indicated times where there were a large number of events in

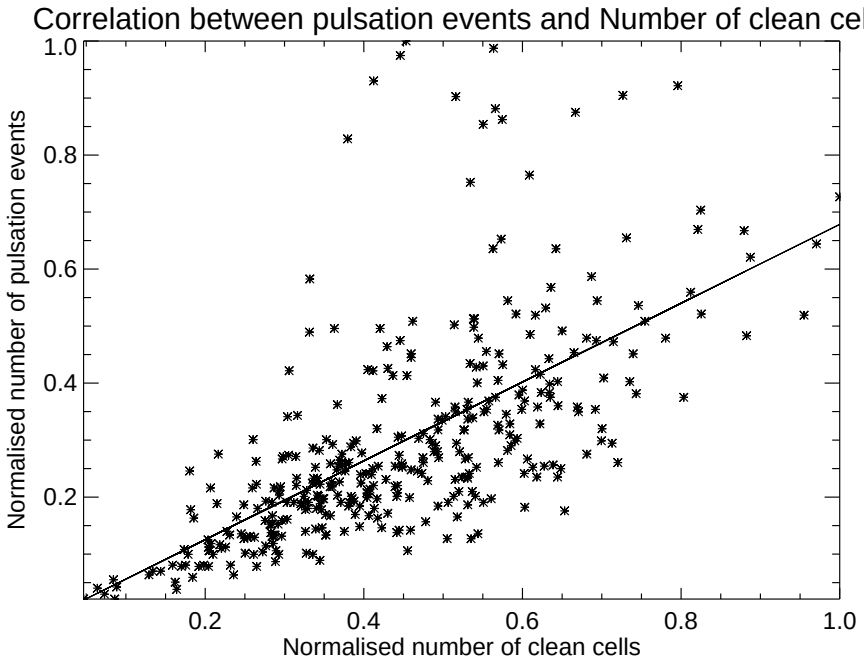

Figure 11.9: Correlation between the daily normalised number of clean cells and the normalised number of pulsation events. The line is a best fit between the two with a slope of 0.691 ± 0.043.

the network. This could be used to identify events to be studied in isolation.

11.4 Directional variations

The amount of pulsation events observed was compared to the bearing angles of the cells to determine if there was a preferred direction that yielded more pulsation events. The normalised distributions are shown in figure 11.11. Theses figures show two peaks, one at 0° in (a) and the other at ±180° AACGM in (b). These correspond to the radars in the northern and southern hemispheres respectively. One can then compare the pulsation distribution with the clean scatter distribution to see if the pulsation occurrence follows the scatter occurrence.

11.4.1 Discussion

The black curves for the pulsations, in figure 11.11, show peaks in the same direction as the clean scatter curves indicating that the pulsations observed by the radar are a function of the bearing of the radar cells and the amount of clean scatter in that direction.

If the output of an instrument (y) could be thought of as the convolution of the parameter

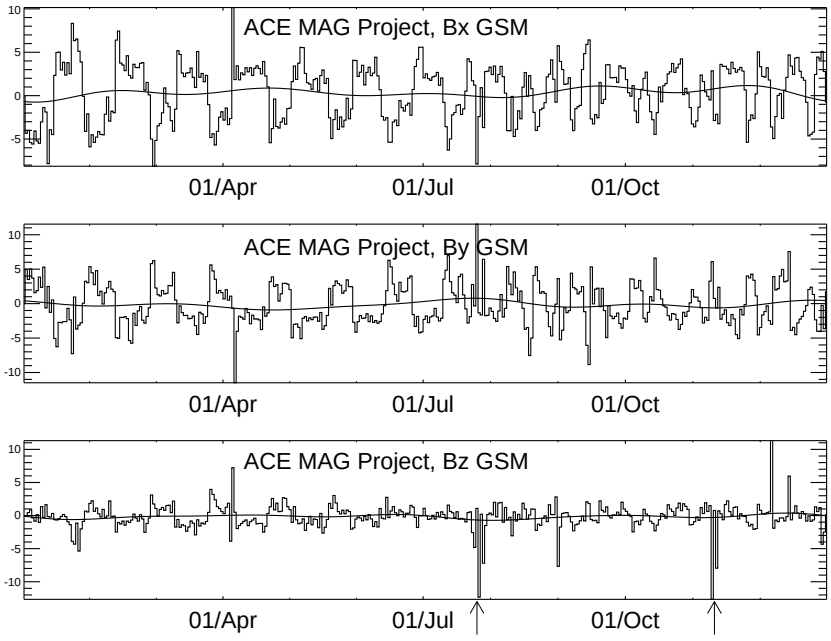

Figure 11.10: The ACE on board magnetometer showing the status of the interplanetary magnetic field in GSM coordinates. The arrows correspond to the arrows of figure 11.7.

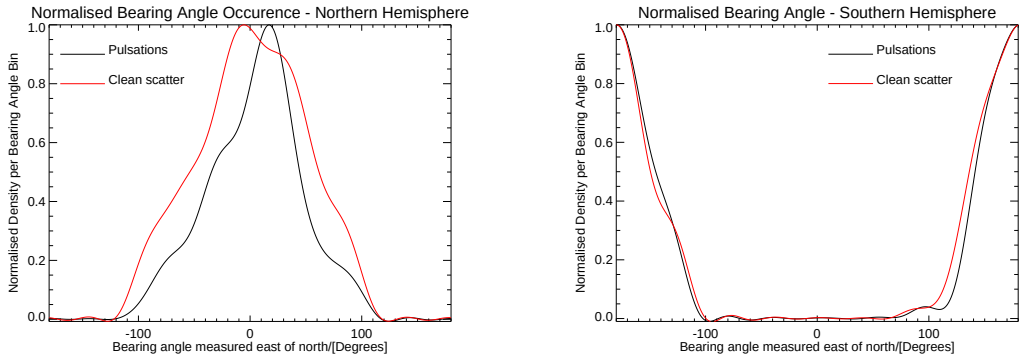

Figure 11.11: Smoothed and normalised versions of the number of clean cells (red) in a particular direction plotted with the number of pulsation events in a particular direction (black).

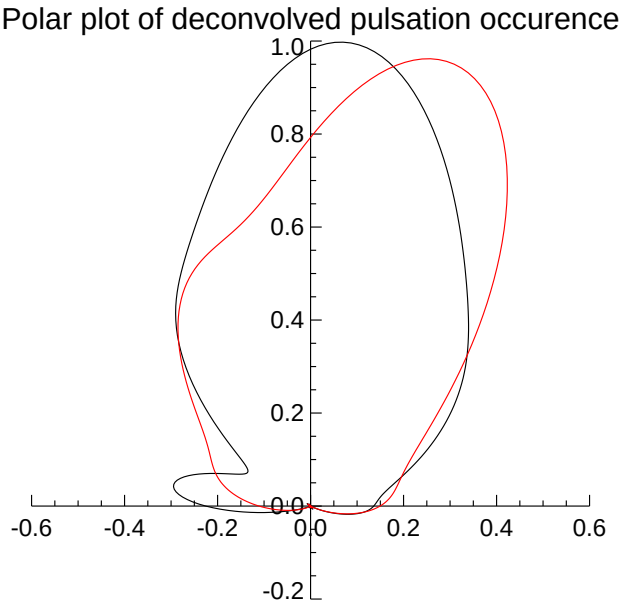

Figure 11.12: Polar plot of the direction of the northern hemisphere measured pulsation occurrence (red) and the deconvolved pulsation occurrence (black).

you were trying to observe (x) and the response of the instrument (h) then

$$y = h \star x.$$

In order to obtain the actual parameter characteristics one would need to deconvolve the instrument response from the output. This could be done by transforming the parameters into the frequency domain, performing a division, then transforming back, as;

$$X = \frac{Y}{H}$$

where X, Y and H are the Fourier transforms of x, y and h.

Using the scatter characteristics as a proxy for h and the observed pulsation characteristics as y we were able to obtain x, the actual pulsation characteristics as a function of direction. The results of the deconvolution are shown as a polar plot in figure 11.12 . In this figure the red trace is a polar plot of the northern hemisphere black line in figure 11.11. There were no corresponding significant peaks in the deconvolution of the southern hemisphere distribution and is thus not presented. In figure 11.12 you can see the peak of the pulsation occurrence curve (red) is slightly east of north similar to the peak in figure 11.11. The deconvolved pattern (black) now had a smaller peak in a westerly direction between $-60°$

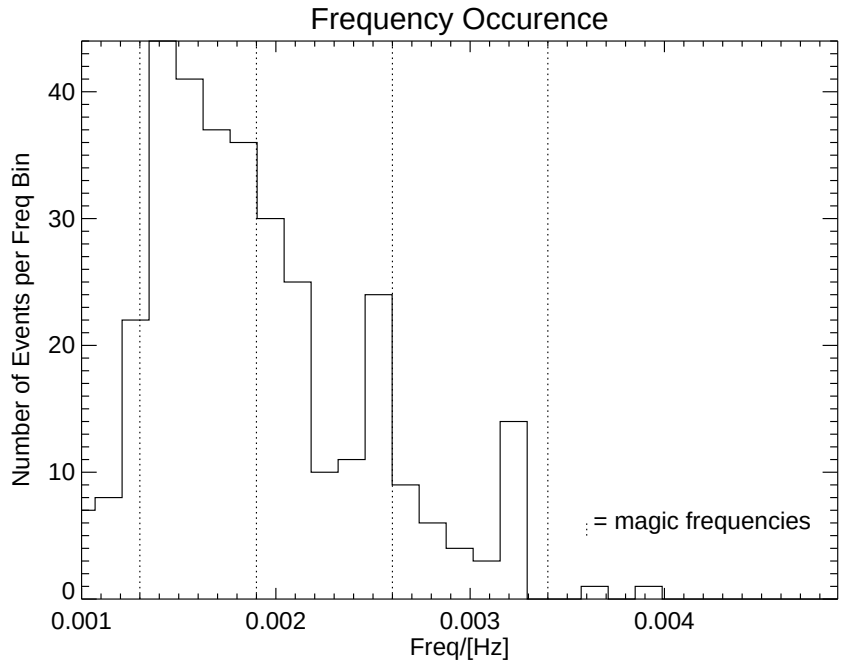

Figure 11.13: Frequency distribution of pulsation events with a bearing range of $-60°$ to $-100°$.

and $-100°$. Both traces were normalised.

We extracted all pulsations that occurred in cells with a bearing of $-60°$ to $-100°$ and the new frequency distribution is shown in figure 11.13 . Significant in this figure were the two peaks at 2.5 and 3.2 mHz. The 2.5 mHz peak was contributed mostly by 2004120114w. The other peak was a combination of a number of events rather than just one event. The Stokkseyri radar contributed over 210 events to this set which was not surprising as it is radar with the most cells with this bearing range.

11.4.2 Conclusion

Equations 5.3 and 5.4 showed that there is a maximum perturbation in the electric field in the ν direction (poloidal in the ionosphere) and in the ϕ direction (toroidal) for the magnetic field perturbation. If the radar is observing a motion in the ionosphere driven by the $\mathcal{E}_\nu$ perturbation, this will result in an $\mathbf{E} \times \mathbf{B}$ drift in the toroidal direction. The radar, however, observes more pulsation events in the poloidal direction contrary to the theory outlined in chapter 5.

The pulsation directional characteristics are strongly modulated by the clean scatter characteristics but it is possible to deconvolve the result and track the actual pulsation dynamics. It was found that there was a peak in the number of pulsations occurring in cells

with a bearing of between $-60°$ and $-100°$. The radar that has the most cells in this direction is the Stokkseyri radar and should be monitored for pulsations.

It is interesting to note that the deconvolution process yielded results in the toroidal direction which is best suited for observing FLR pulsations.

Work has been done, [51], [28] and [80], to use single radars to determine the direction of the pulsating irregularities by fitting amplitude and phase measurements with the assumption that the velocity observed by the radar is given by

$$V_r = V\cos(\alpha - \theta)$$

where V_r is measured by the radar, V is the velocity of the irregularities, α is the bearing of the cell and θ is the direction of the motion of the irregularities. It must be remembered that a FLR pulsation will have a latitudinal amplitude and phase relationship as well. So we now have;

$$V_r = V(amp, \phi)\cos(\alpha - \theta)$$

where amp and ϕ are the amplitude and phase behaviour of the FLR. Ponomarenko et al [46] was able to partially model this behaviour with a single radar but these two relationships can only be correctly identified if there are two independent collocated measurements of the pulsation. This is the subject of chapter 12.

11.5 Occurrence by station

The number of events identified per station is shown in figure 11.14. The Tasmainian part of TIGER and Syowa South show a significantly large and small number of events respectively. This matches the results from figure 9.8 where these two radars showed both large and small percentages of clean scatter respectively.

The Unwin part of TIGER has only a few pulsation events compared to the Tasmanian part of TIGER as the radar only came on-line towards the end of 2004.

Goose Bay differs in that although there was a significant percentage of clean scatter, there were only a few pulsation events. The radar paired with Goose Bay, Stokkseyri, although viewing the same area, showed more clean scatter in figure 11.14.

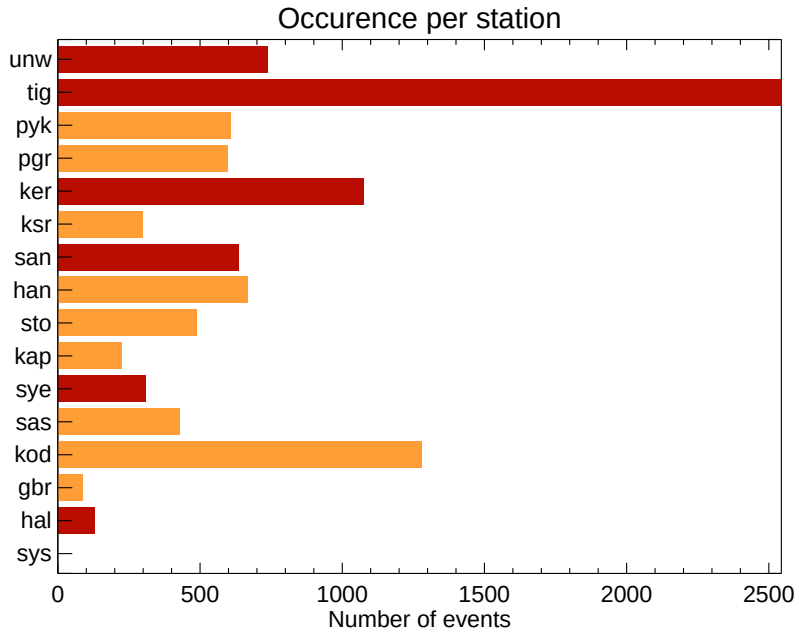

Figure 11.14: The number of events identified at each station.

Chapter 12

Merging the radars fields of view

12.1 Introduction

The SuperDARN network has been designed so that the fields of view of at least two radars overlap. This is to allow the calculation of the bulk velocity vector of the convection polar ionosphere [30]. The process used to merge the data from two overlapping radars in convection analysis, [31], is insufficient for pulsation studies as the data are time averaged and thus filter out the pulsation events and ground scatter is excluded. This chapter uses data from an event in 2002 to illustrate the techniques that can be used to merge data from two overlapping radars for pulsation studies. The Halley Bay (61.68°S, 28.92°E AACGM magnetic [16]) and SANAE (61.52°S, 43.18°E AACGM magnetic) radars together with their fields of view are shown in figure 12.1.

First we describe how the data are prepared for merging, then follows a description of the merge process and finally the products of the merge process are presented.

12.2 Preparing high resolution data

Merging high time resolution data for pulsation studies require simultaneous data for both stations. There are two problems with SuperDARN data in this regard. The first being that although the radars are measuring the same area, the scatter conditions may be different for the two radars resulting in there being data for one radar but not the other. The second problem is that although the radars sounding schedule is coordinated, it is not possible to measure all the overlapping cells for the two radars at exactly the same time.

12.2.1 Filling the data gaps

SuperDARN FIT data often contains gaps. Here I will explain the process that I used to fill in the missing gaps.

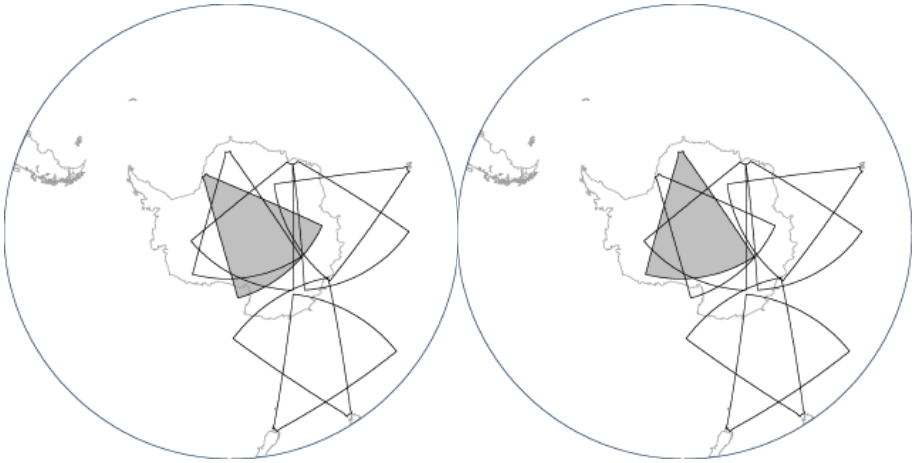

Figure 12.1: The Antarctic network of SuperDARN radars with the fields of view of the Halley Bay (a) and SANAE (b) radars highlighted.

The pulsation finder processed individual data series, that is, how the velocity parameter varied with time for a specific cell or location. Pulsation signatures in the ionosphere should be visible across a number of locations. The manner in which the pulsation signatures vary with space and time that helps one determine the possible cause of the pulsation. Instead of looking at a data event as being a single one dimensional time series, we looked at the data for the whole beam. Now the interpolation can be done in both space and time. In figure 12.2 you can see the raw FIT velocity data. This data is cleaned using an automated process outlined above (see section 8.2). The resulting cleaned data is shown in figure 12.3. Here it is clear that the pulsation event occurred across a number of ranges and for a long duration of time. To interpolate each range would ignore the fact that the process driving this event is responsible for all the ranges. It would be better to interpolate in two dimensions rather that just the one.

Multidimensional interpolation is often used in imaging systems. A survey paper by Amidror [11], reviewed the different techniques for interpolating scattered data. Scattered data is data that does not fill the regular grid such as the data in figure 12.3.

The radial basis method of interpolation is a method works well in terms of fitting ability and visual smoothness. It is computationally intensive though, as it is a global method requiring the solution n equations with n coefficients for n data values. The computational intensity can be reduced by making the method more local. Here, instead of solving equations for the whole system, the problem is divided into smaller local regions. The IDL routine GRIDDATA was used for the interpolation with the /RADIAL_BASIS_FUNCTION method. In order to localise the routine an array was created describing the connectivity of the input points. This was done using Delaunay triangulation which creates a set of triangles such that no original data point is inside the circumcircle of any triangle. In figure 12.4 the original data (in black) is plotted together with the Delaunay triangulation (filled triangles) and the interpolated data (in blue). The Delaunay triangulation is included for illustrative purposes, here each triangle is filled with the average of the values

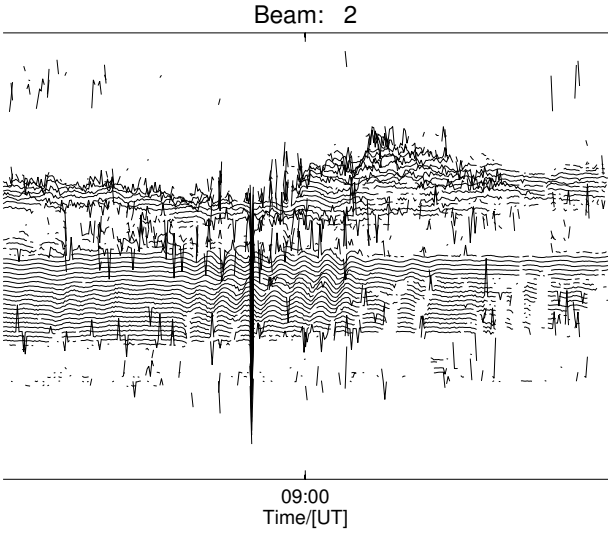

Figure 12.2: The raw FIT velocity data for beam 5 on the 5th of August 2002.

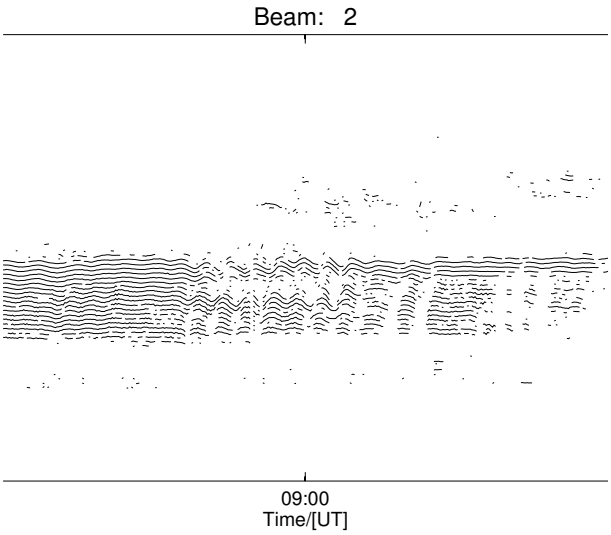

Figure 12.3: Cleaned data ready for interpolation.

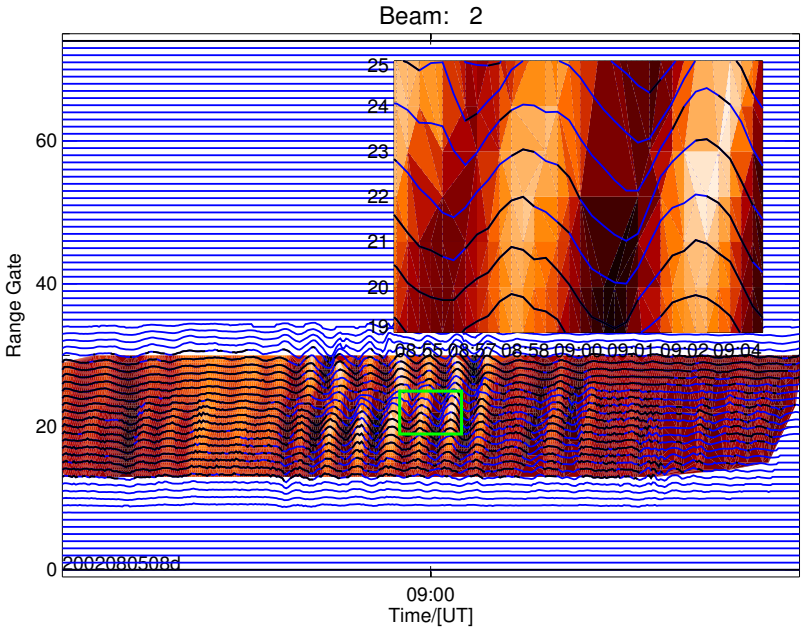

Figure 12.4: The data from figure 12.3 interpolated using two dimensional interpolation. The insert is an enlargement of the indicated rectangular area.

at its vertices's. You can see that there is a good correlation between the filled triangles and the original data. An enlargement of part of the data is included for clarity.

12.2.2 Time Differences

In order to merge the velocity data from two different radars, the values need to be recorded at the same instant. The merge process outlined by Hanuise et al [31] requires the velocity values to be time averaged. This is not suitable for pulsation analysis as the time averaging may smooth out higher frequency pulsations. Although the data from the different radars are following a coordinated sounding program there is no guarantee that the cell of interest will be sampled at the same instant. It reality, it is possible for cells to be sampled with differences of up to the half the normal radar sampling period. In figure 12.5 the plot shows the difference in starting times of the records for the overlapping cells. The maximum difference in starting time is 113 seconds. This in itself is not significant because if the sampling period is a half multiple of 113 seconds then the data values for the two records will match, apart form the first few or last few. The colour contour shows that there are a variety of different starting times so it is quite possible for two records to start 60 seconds apart. With a sampling period of 120 seconds (typical for slow scan modes) there could be a 60 second shift between the two data sets. Data from two cells recorded 60 seconds apart will have a phase difference of 77° if the pulsation frequency is 3.6mHz, so you could be merging two points that are almost 90° out of phase with each other.

Various methods were examined to cope with this problem.

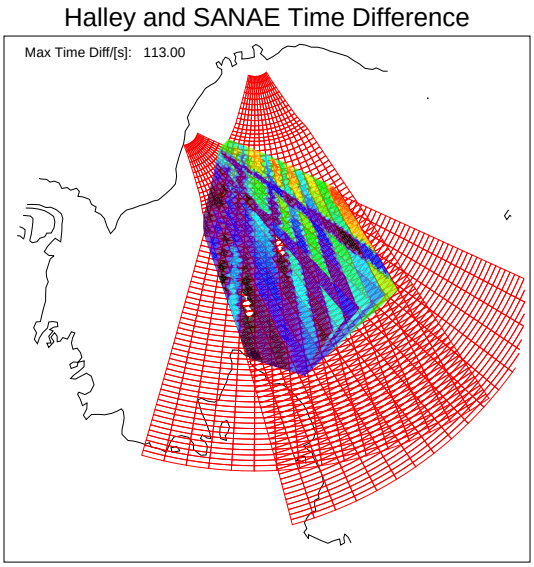

Figure 12.5: The time difference in starting times for records from co-located cells in the Halley and SANAE data.

Simultaneous events

The first method is to only merge the two records if the time difference in the records is small enough. This presents its own problems. If we look at an example of merging Halley and SANAE data, on the 5th of August 2002 for the 08:00UT FIT file. A lat-long point of $-68.5°S$, $25°E$ AACGM gives the Halley cell as beam-3 range-15 and SANAE as beam-1 range-27, see figure 12.6. The SANAE data was sampled with a 74.9 second resolution while the Halley data was sampled with a 99.4 second resolution. It follows that there are more samples in the SANAE data (96 against 73). The difference in sampling period means that there will be times in the two hour record when the data points are close in time and others when they are far.

Using a method that relies on the time difference between the samples means that some of the data will be discarded. A more elegant method would be to re-sample the data at a higher resolution in both records.

Re-sampling - Frequency Domain

Sutcliffe [61] proposed a method to reduce the sampling interval by transforming the original time series into the frequency domain, padding the spectrum with zeros and then transforming back to the time domain. This method works because if the data has been sampled according to the Nyquist criteria then one is not changing the spectral content at a frequency below this cutoff. Although this method is the most elegant, it was not used

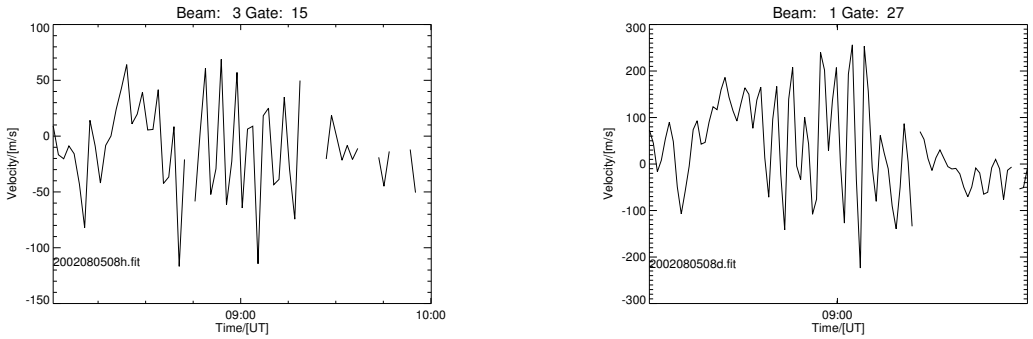

(a) Halley Bay (b) SANAE

Figure 12.6: Velocity data for co-located cells on the 5th of August 2002.

as the resulting high resolution time series was shifted with respect to the original time series.

Re-sampling -Time Domain

Cubic convolution is an interpolation method that closely approximates the theoretically optimum sync interpolation function using cubic polynomials. If the original signal, f, is a band-limited signal, with no frequency component larger than ω_0, and f is sampled with spacing less than or equal to $1/\omega_0$, then f can be reconstructed by convolving with a sync function [1]. The data were re-sampled using the IDL CONGRID function with the cubic option. The data were re-sampled so that there were 7200 samples between the first and last samples of a two hour record. The value of 7200 was chosen so that there would be at most 1 second between the re-sampled data points in the two records. The Halley data from figure 12.6 is shown in figure 12.7.

12.3 The merge process

The configuration of the SuperDARN radar's fields of view is such that each radar is paired with at least one other radar. The radars will record the line of sight velocity of the irregularities in its field of view, meaning the velocity that is stored for a cell in its field of view is the component of the total velocity in the direction of the beam. If two radars record data for the same region then the data from the two cells can be merged to give the direction of the actual motion of the irregularities. In order to better understand the source of the energy of the pulsation, it is necessary to know the components of the field line pulsation in the magnetic poloidal (North-South) and toroidal (East-West) directions.

The process of merging two or more radars to find the bulk motion of the ionosphere for polar ionospheric convection studies cannot be used to find the poloidal and toroidal

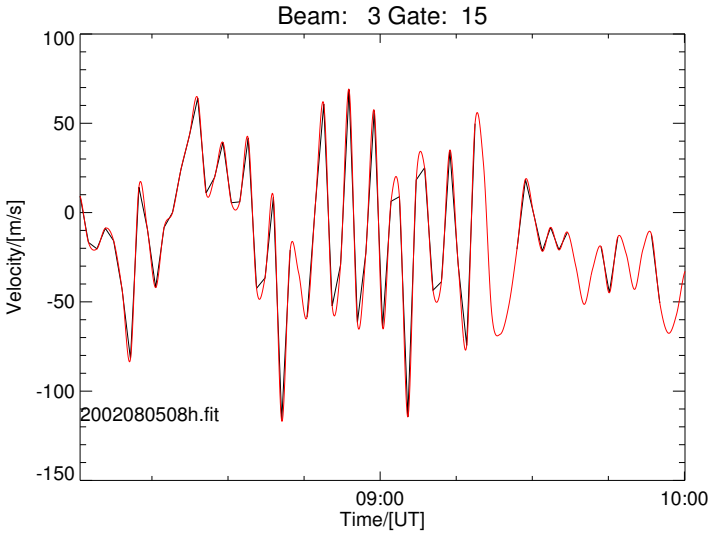

Figure 12.7: Re-sampled Halley data from figure 12.6 (a).

components of a pulsation. The convection-merging technique is interested in the time and space averaged behaviour of the bulk motion [50], whereas pulsation studies require the instantaneous values of the poloidal and toroidal components. To find these components, the fields of view of the Halley and SANAE radars were sectioned with a wedge going from $-80°$ to $-65°$ south (AACGM), from $0°$ to $60°$ east and then divided into a $0.5°$ grid of magnetic latitude and longitude. This is the green wedge in figure 12.8. For each grid point the corresponding Halley and SANAE cell beam number, range gate and magnetic bearing were recorded as is shown in figure 12.8. The figure shows the corresponding Halley and SANAE cells in filled green for the magnetic latitude $-68.5°$ and longitude $25°$ AACGM. The blue lines represent the lines of longitude and latitude. The magnetic bearing is determined by calculating the magnetic azimuth of a line pointing in the direction of the beam centre. The magnetic bearing for the green cells in figure 12.8 is shown in the top left hand corner of the plot and are given as east of north.

Given a bulk periodic motion in the ionosphere moving in a direction relative to AACGM north, the radars will measure the component of the motion in their line of sight directions as is shown in figure F.2. In order to determine the bulk motion, these velocities need to be merged to yield the poloidal and toroidal components.

The motion observed by a radar can be used to calculate the poloidal and toroidal components (see Appendix F):

$$v_{tor} = \frac{\cos\theta_{\hat{S}} v_H - \cos\theta_{\hat{H}} v_S}{\sin\left(\theta_{\hat{H}} - \theta_{\hat{S}}\right)} \tag{12.1}$$

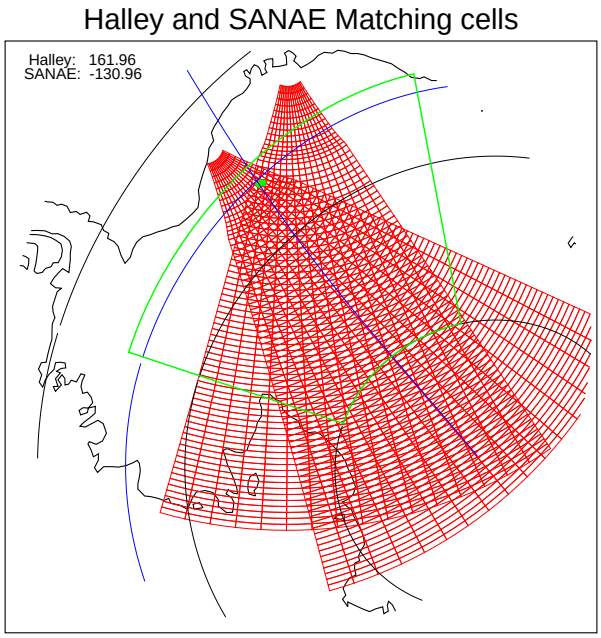

Figure 12.8: The Halley and SANAE fields of view overlaid with the AACGM coordinates (black), merging area (green wedge), co-located cells (filled green box), final coordinates (blue) and bearing angles (top left corner).

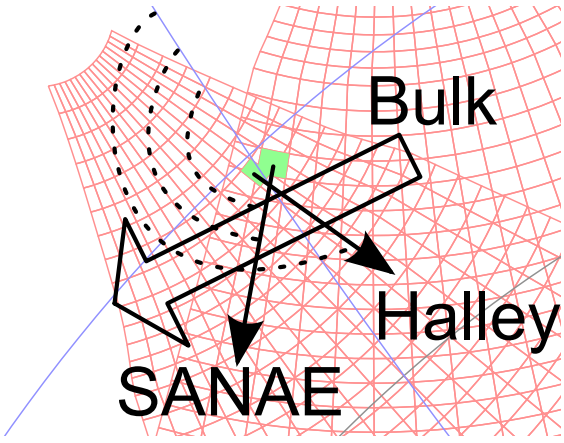

Figure 12.9: The Halley and SANAE co-located cells showing the bearing angles for each cell with respect to AACGM north as well as the bearing angle for the bulk ionospheric motion.

$$v_{pol} = -\frac{\sin\theta_{\hat{S}} v_H - \sin\theta_{\hat{H}} v_S}{\sin\left(\theta_{\hat{H}} - \theta_{\hat{S}}\right)}, \tag{12.2}$$

where v_S and v_H are the velocities measured by the SANAE and Halley radars, $\theta_{\hat{S}}$ and $\theta_{\hat{H}}$ are the bearing angles respectively and v_{pol} and v_{tor} are the poloidal and toroidal components. The amplitude and direction of the bulk motion will then be represented by

$$|v_b| = \sqrt{v_{pol}^2 + v_{tor}^2}$$

and

$$\theta_{\hat{b}} = 90^\circ - \tan^{-1}\frac{v_{pol}}{v_{tor}}.$$

The factor of 90° is due to the fact that the bearing is measured east of north and not north of east as is the case with polar angles in Cartesian geometry.

12.4 Data description

A field line resonant pulsation will have distinct amplitude and phase profile as a function of latitude and longitude. [73] The amplitude and phase profiles can be found by creating an analytic signal for the original data. A general signal $f(t)$ is given by;

$$f(t) = A(t)\cos(\omega t + \phi(t)),$$

$A(t)$ is the time varying amplitude of the pulsation and $(\omega t + \phi(t))$ is the time varying phase.

12.4.1 Complex demodulation

A monochromatic signal similar to the one in figure 12.10 can be complex demodulated in order to obtain the instantaneous amplitude and phase of the signal. Complex demodulation involves multiplying the signal

$$f(t) = A(t)\cos(\omega t + \phi(t))$$

with a unit amplitude sine of exactly the same frequency

$$\sin(\omega t)$$

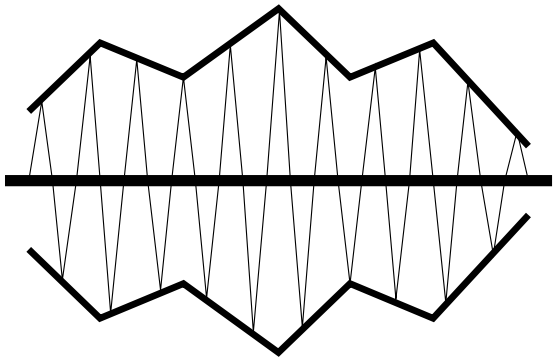

Figure 12.10: An example of a pulsation showing the frequency and the amplitude of the pulsation.

resulting in two signals. One at twice the frequency and one at zero hertz. The data can be low pass filtered leaving the base band signal

$$f(t) = A(t)e^{\imath\phi(t)}.$$

In order for complex demodulation to work, the pulsation frequency is needed before hand.

12.4.2 Analytic Signal

An analytic signal, $f(t)$, represents the instantaneous amplitude and phase of a quasi-monochromatic wave $F(t)$ and can be calculated from:

$$f(t) = F(t) - iH(t)$$

where $F(t)$ is the quasi-monochromatic signal and $H(t)$ is the Hilbert transform of $F(t)$.

If $F(t)$ is monochromatic then $f(t)$ is given by

$$f(t) = A(t)e^{\imath(\omega t+\phi)}$$

The rate of change of phase with time, $d(\omega t+\phi)/dt$, is then the frequency of the monochromatic signal, ω, and an instantaneous difference of phase recorded at two different locations will yield the phase difference ($\phi_1 - \phi_2$) between the signals at those two locations.

The advantage to this method is that there is no prior knowledge of the pulsation required, the disadvantage is that if the signal is not monochromatic then there may be contamination due to other frequency components.

The analytical signal of the data in figure 12.7 is shown in figure 12.11.

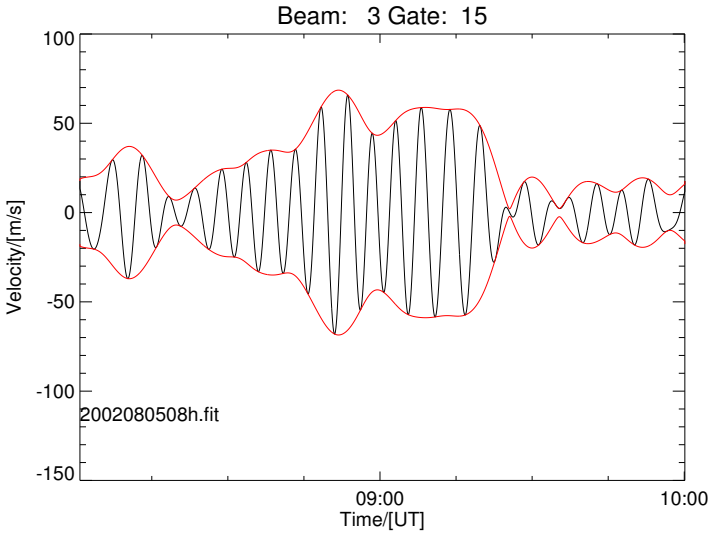

Figure 12.11: The analytical signal for range gate 15 in beam 3 for the Halley Bay radar on 5 August 2002. This data corresponds to the data shown in figure 12.7.

12.5 Polarisation characteristics

Once the amplitude and phase of components were determined, the ellipticity and polarisation angle [48] can be calculated for each grid location as a function of time.

12.6 Summary

The poloidal and toroidal components of a pulsation event can be calculated from the line of sight velocity of two radars observing the same region of the ionosphere. A look-up file has been created for each radar pair in the SuperDARN network. The file gives the co-located cells of the two radars for a 0.5°AACGM grid under the field of view of the radars. This can then be used to merge the data from the two radars.

Chapter 13

Lorem ipsum

Lorem ipsum [9] dolor sit amet, consectetur adipisicing elit, sed do eiusmod tempor incididunt ut labore et dolore magna aliqua. Ut enim ad minim veniam, quis nostrud exercitation ullamco laboris nisi ut aliquip ex ea commodo consequat. Duis aute irure dolor in reprehenderit in voluptate velit esse cillum dolore eu fugiat nulla pariatur. Excepteur sint occaecat cupidatat non proident, sunt in culpa qui officia deserunt mollit anim id est laborum.[1]

[1] An attempt to avoid the number 13.

Chapter 14

Some events in detail

This investigation focused on Pc5 pulsations as these are the pulsations most frequently observed at the radar latitudes [13]. As is evident in figure 11.3 thousands of events are identified by the pulsation finder, however, chapter 11 concluded that there are a limited number of events that have the requisite spatial and temporal coverage to study global pulsation dynamics. The pulsation finder should rather be used as an identifier for significant pulsation events. An analysis of each individual event is beyond the scope of this thesis and so a few events were chosen to illustrate the kind of observations that can be made and the limitations that exist when working with radar data.

The first two events show interesting pulsation characteristics where in the first there are two different pulsation frequencies that are measured by the radar and satellite data and only the lower frequency was observed on the ground. The second shows a rare event where pulsation data were measured in two collocated radars allowing a full component analysis of the event.

The next two events were included as an indication of how radar pulsation data are a consequence of the setup of the radar sounding schedule as well as the pulsation dynamics. The first shows how a higher frequency pulsation might go unnoticed in the radar data due to undersampling and aliasing. The second shows how a schedule with changing sounding frequencies can distort pulsation observations.

14.1 Multiple frequencies on 2 September 2004

The frequency distribution histogram in figure 11.3 shows that on average higher frequency pulsations are less probable. The daily histogram on 2 September 2004 in figure 14.1 shows a large count of pulsation events at 3.1 mHz. The histogram in figure 14.1 includes data from all the radars in the SuperDARN network. Figure 14.2 shows SANAE had the most pulsation events on this day and that the events occurred at 18:00 UT. On closer inspection

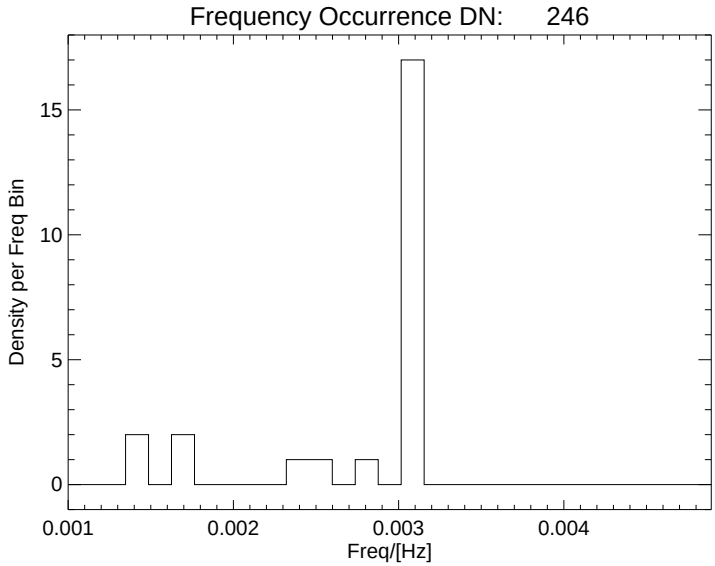

Figure 14.1: Pulsation occurrence histogram for 2 September 2004.

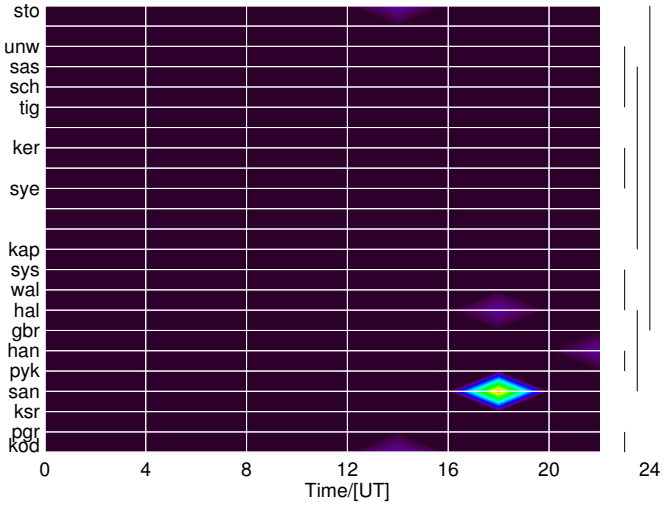

Figure 14.2: Plot used to identify the time and location of a pulsation event. A brightness in intensity indicates more pulsation events. In this case the pulsation detector identified a number of events at SANAE at 18:00 UT.

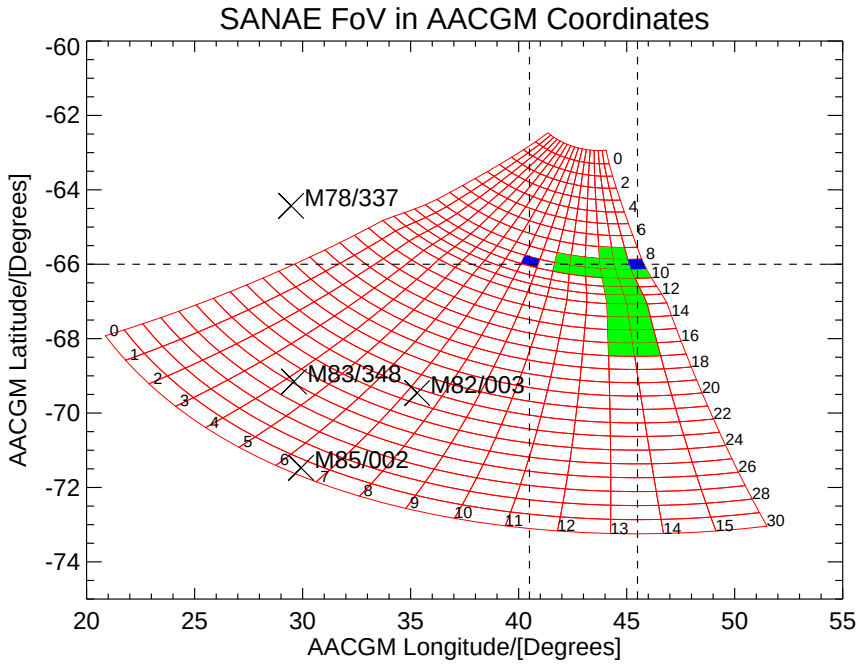

Figure 14.3: The first 31 ranges of the SANAE field of view plotted in AACGM coordinates are shown as red boxes. The green shading indicates cells that fall on lines of near constant latitude (range 9 and 10) and longitude (beam 13 and 14). The blue cells are used to determine the m number of the higher frequency pulsation.

of the data it was found that a pulsation outside the Pc5 band were also present. This pulsation had a higher frequency of between 7 and 10 mHz.

14.1.1 The extent of the pulsations

The field of view region of the SANAE radar was expanded and is shown in figure 14.3. It was found that this event spanned 4 hours of universal time. The most western extent of the event was 30° AACGM longitude with the eastern most extent being 50° AACGM. The magnetic local time of 30° at 16:00 UT is 13:00 MLT and 50° at 20:00 UT is 18:45 MLT indicating that the event is in the magnetic local time afternoon sector. The green shaded cells are lines of near constant latitude and longitude. The two blue cells are used to determine the m number of the higher frequency pulsation. Also shown are the BAS LPM stations near the event.

14.1.2 The pulsations

The pulsation characteristics for constant longitude are shown in figure 14.4. The pulsation in range gate 10 for beams 10 to 15 are shown in figure 14.5. There are two distinct

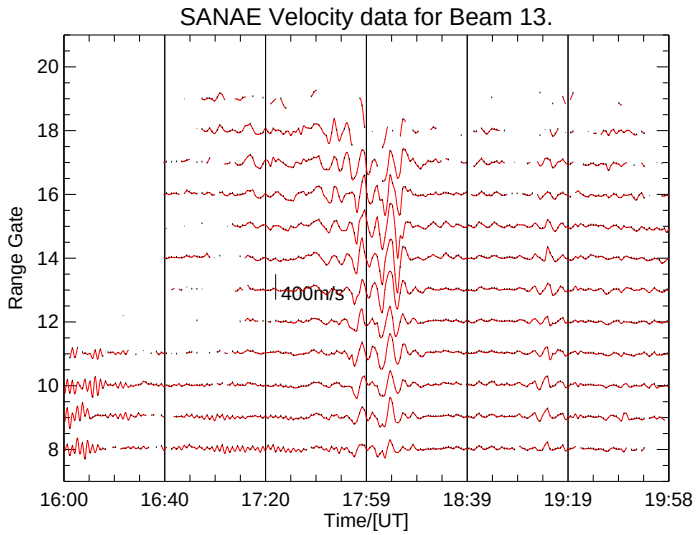

Figure 14.4: Pulsations for 2 September 2004 at SANAE. The plot shows the pulsations occurring simultaneously in different ranges for beam 13. Beam 13 was chosen as it is almost a line of constant AACGM longitude (see figure 14.3).

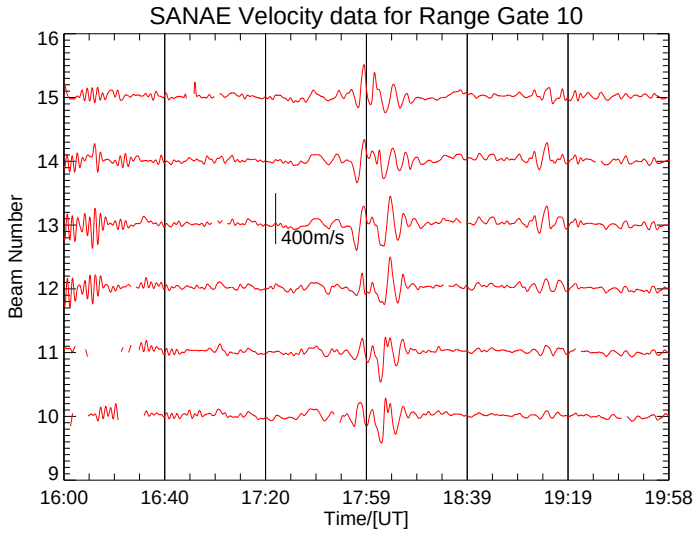

Figure 14.5: Pulsations for 2 September 2004 at SANAE. The plots correspond to range gate 10 in figure 14.3 and are plotted for beams 10 through 15 showing the pulsations as a function of constant AACGM latitude.

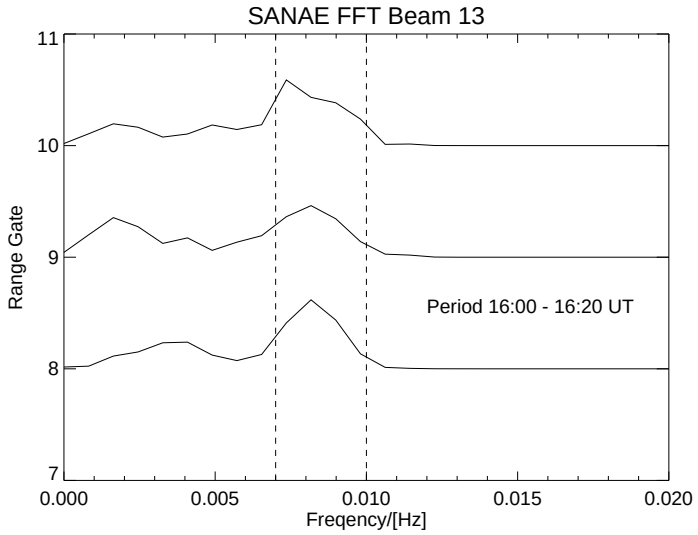

Figure 14.6: Spectra for the higher frequency pulsations from 2 September 2004.

pulsation regions in these data, one with a high frequency but limited extent and the other at a much lower frequency across more cells. The area (both spatially and temporally) dominated by the higher frequency pulsation contains a significant number of data gaps making it difficult to study the pulsation dynamics.

Higher frequency pulsation between 16:00 and 16:20 UT

The spectra of the cells for beam 13 range gates 8 to 10 are shown in figure 14.6. The spectra show a broad peak between 7 mHz and 10 mHz. The low spectral resolution is due to the limited time span of the data.

Lower frequency pulsation between 17:20 and 18:40 UT

The spectra of the cells for beam 13 range gates 8 to 16 are shown in figure 14.7. The spectra show peaks between 2 mHz and 4 mHz.

14.1.3 Discussion

The pulsations in this event show two pulsation frequencies that are observable in the ionosphere. The fact that they are observable in the ionosphere indicates that the Pedersen conductivity is sufficiently low for the first order electric fields to be present in the ionosphere and produce the $\mathbf{E} \times \mathbf{B}$ drifts that are observed by the radar.

The two frequencies are roughly three times apart, possibly indicating that the higher frequency pulsation is a higher harmonic of the lower one. In order to test this hypothesis

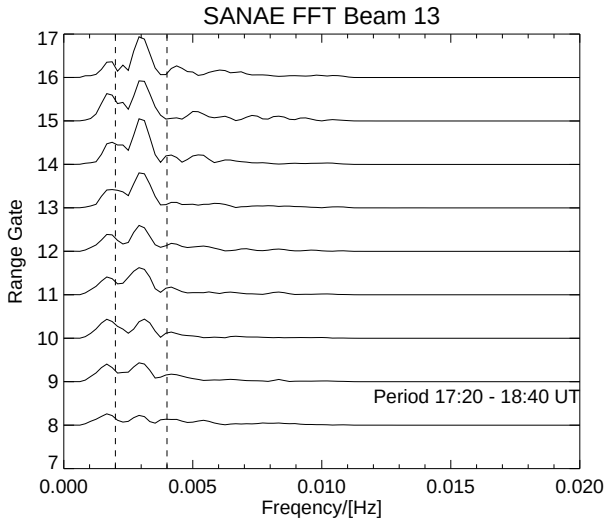

Figure 14.7: Spectra for the lower frequency pulsations from 2 September 2004.

data were extracted from ground-based magnetometers and magnetometers on board the geostationary GOES 12 satellite.

The ground-based data from the BAS low power magnetometer M85/002 (figure 14.8) shows pulsations at the same time as the lower frequency pulsations and with the same frequency. There is no evidence of the higher frequency pulsations in the magnetometer data.

The Tsyganenko magnetosphere model [66] was used to trace the magnetic field line that passes through the point 67°S and 45°E AACGM (the centre of the green cells in figure 14.3) into the GSM $x-y$ plane. The points during the four hours of interest are shown as the black curve in figure 14.9. Figure 14.9 also shows the GOES 12 position at the same time in red. The GOES 12 data in figure 14.10 show both the lower frequency pulsation and the higher frequency pulsation. The higher frequency pulsation, just below 8 mHz in this plot due to aliasing, occurred from 17:00 UT till just after 18:00 UT. This is the same time as the radar's lower frequency pulsations. These lower frequency pulsations are also visible in the GOES data.

If the lower frequency is the fundamental ($n = 1$) and the higher frequency data are indeed the third harmonic ($n = 3$) then one would expect nodes in b at the equator to mean that the geostationary magnetometer would not observe the pulsations. The fact that the pulsation is being observed by the radar indicates that the conductivity in the ionosphere is sufficient for the first order correction electric and magnetic fields to be present. The event is close to the equinox meaning that the two polar ionospheres would have comparable conductivities needed for first order standing waves.

The box model of figure 3.2 shows that the first order corrections are 90° out of phase

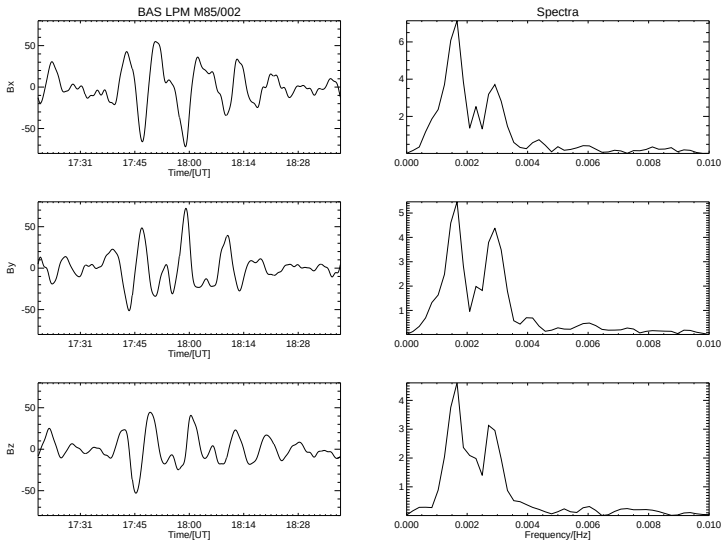

Figure 14.8: BAS LPM data for 2 September 2004. The spectra of the components are shown on the right.

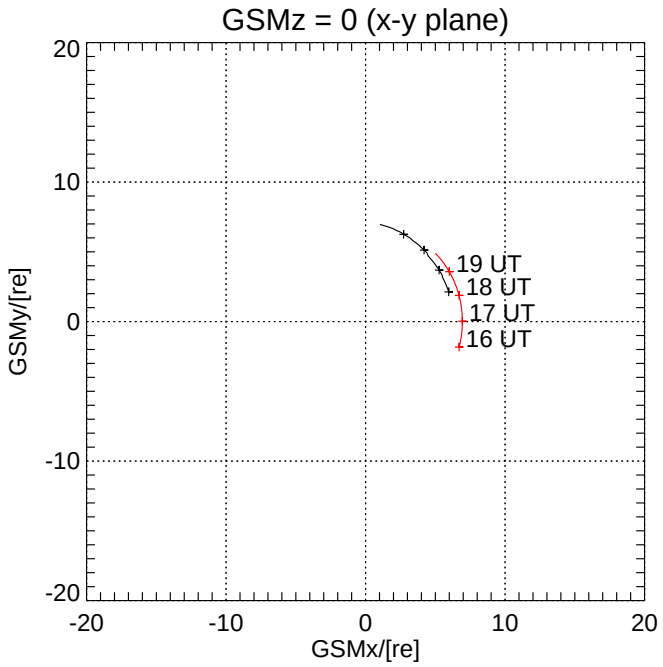

Figure 14.9: GSM $x - y$ plane. The black line is the location of the point $67°$S and $45°$E AACGM in the ionosphere traced along a field line into the $x - y$ plane. The red line shows the position of GOES 12.

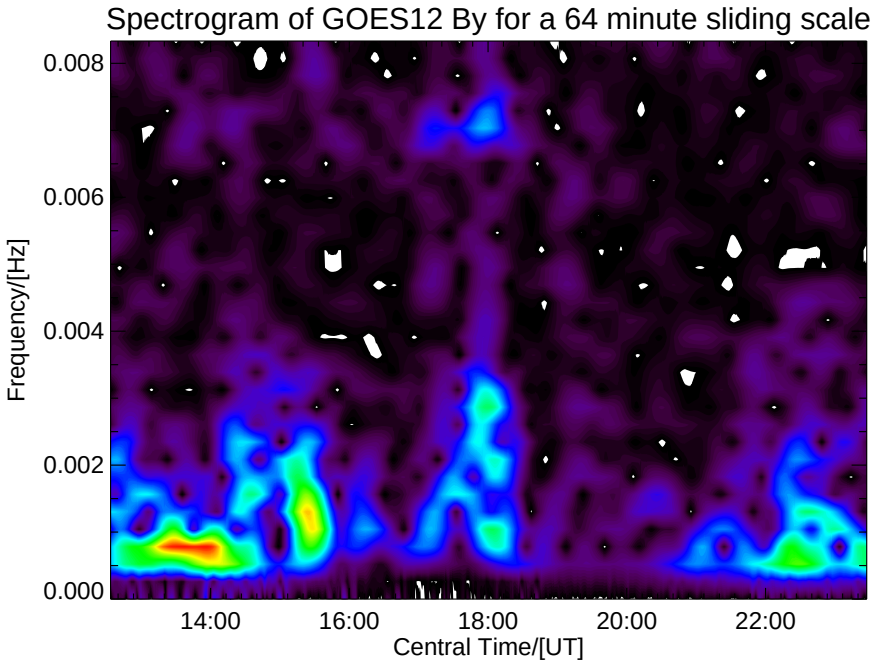

Figure 14.10: GOES 12 magnetometer B_y data for 2 September 2004. The spectra are generated with a 64 minute sliding scale.

with the zero order standing waves and would thus result in observable magnetic fields in the equatorial plane for the fundamental and third harmonic pulsations. A numerical calculation of equations 5.3 and 5.4, using the dipole model of chapter 5, starting with $\mathcal{B}_\phi = 1+\imath 1$ and $\mathcal{E}_\nu = 0+\imath 1$ in the ionosphere and mapped towards the equatorial plane are shown for the fundamental mode standing wave in figure 14.11. This shows that there will be a non-zero value for the imaginary (first order correction) part of $\mathcal{B}_\phi$ in the equatorial plane which can be measured by GOES.

If the fundamental has a frequency of 3 mHz then one would expect the third harmonic to be 9 mHz. The radar and GOES 12 data are sampled at 60 s intervals giving a Nyquist frequency of 8 mHz. This would mean that the high frequency pulsations would be aliased to 7 mHz. This is the frequency seen strongly in the GOES B_y data of figure 14.10. The radar data in figure 14.4 has too low a resolution to accurately resolve the peak as the pulsations were only observable for twenty minutes.

The higher frequency velocity data for 10 minutes in the two blue cells of figure 14.3 is shown in figure 14.12 with the more eastward cell in red. A fit to the unwrapped phase of the analytical signal for the two pulsations gave a phase difference of 73.2° giving an m number of 14.6. The red curve leads the black curve indicating that the phase is propagating in a westerly direction. The event is in the afternoon MLT sector indicating that the phase is propagating in a sun-wards direction.

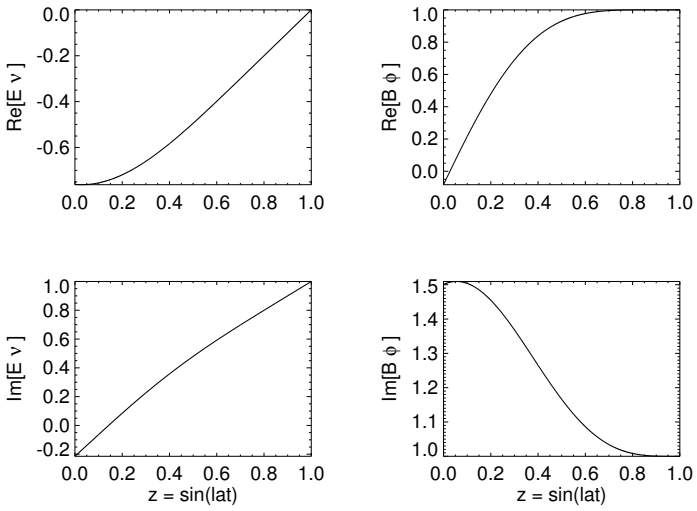

Figure 14.11: Numerical calculations of $\mathcal{B}_\phi$ and $\mathcal{E}_\nu$ starting in the ionosphere and mapping towards the equatorial plane.

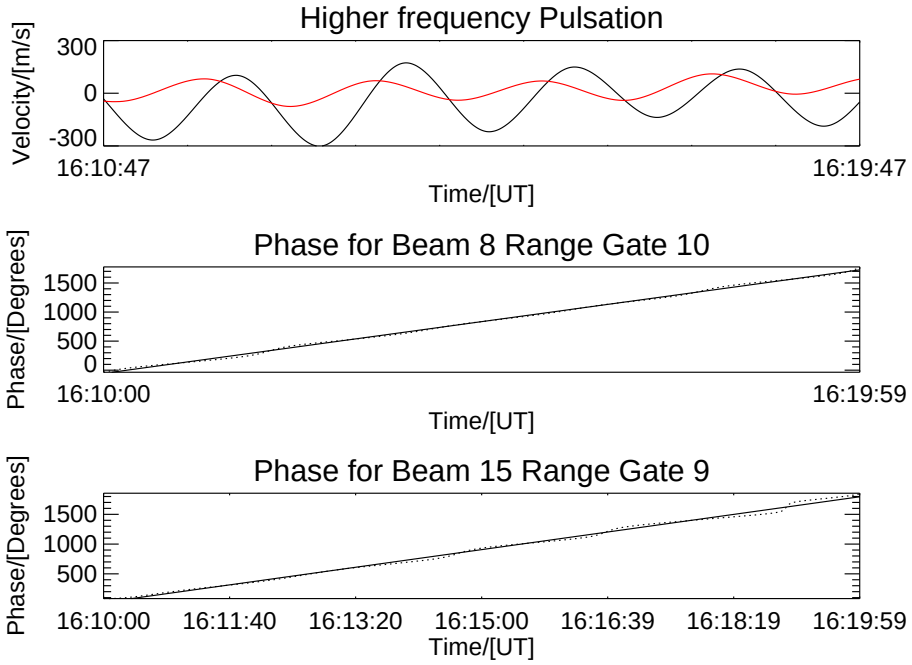

Figure 14.12: The top panel shows the higher frequency pulsation from the two blue cells of figure 14.3. The red trace is for the cell in beam 15 and the black for beam 8. The bottom two panels show the unwrapped phase of the analytical signal of each pulsation.

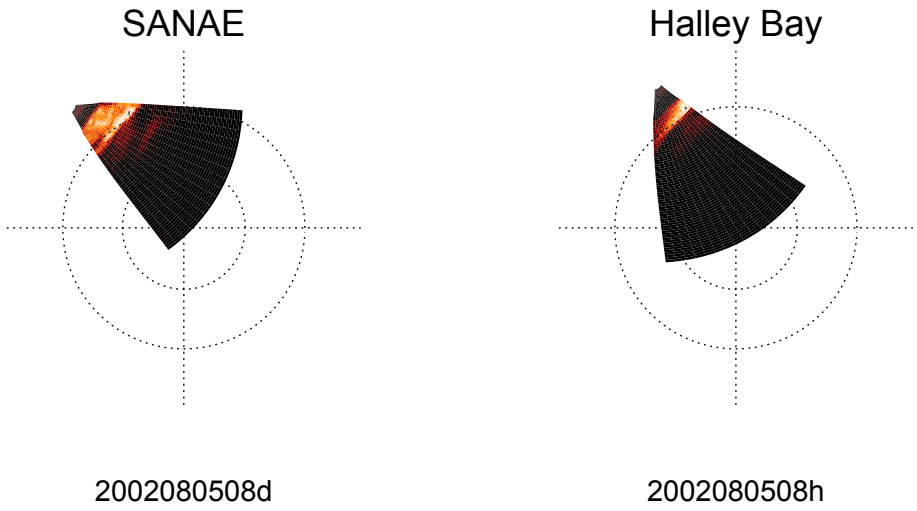

Figure 14.13: Percentage clean scatter for SANAE and Halley Bay on 5 August 2002. The brighter the cell, the greater the percentage clean scatter.

Higher order standing waves translate into a higher k_z. In section 4.5 it was shown that below the ionosphere the pulsation is actually an evanescent electromagnetic wave of which the attenuation is proportional to k_z, explaining why the higher frequency pulsation is not observed in the ground data.

14.1.4 Conclusion

There are clearly two different pulsation signatures in the radar data. The higher frequency pulsation in the radar is approximately 3 times the lower frequency and occurs primarily before 18:00UT. There are similar pulsations present in the GOES12 B_y component although the higher frequency pulsation does not stop before 18:00UT. The higher frequency pulsation is not observed by collocated magnetometers on the ground possibly due to filtering because of a large k_z. The full spatial characteristics of the higher frequency pulsation cannot be determined as there are often large gaps in the data. The phase characteristics between two cells shows a sun-ward propagating phase with an m number of 14.6. The higher frequency and the m characteristics indicate that the pulsation is possibly of magnetospheric origin possibly a wave-particle interaction [77].

The limited spatial and temporal data available for the higher frequency makes it difficult to fully discuss its nature, save to say that this again illustrates why the radar network has limitations for making observations of pulsations across large areas and time scales.

14.2 Merged data on 5 August 2002

Day number 217 in 2002 showed that there were significant clean scatter from overlapping cells in the Halley Bay and SANAE radars as is indicated in figure 14.13. The pulsation

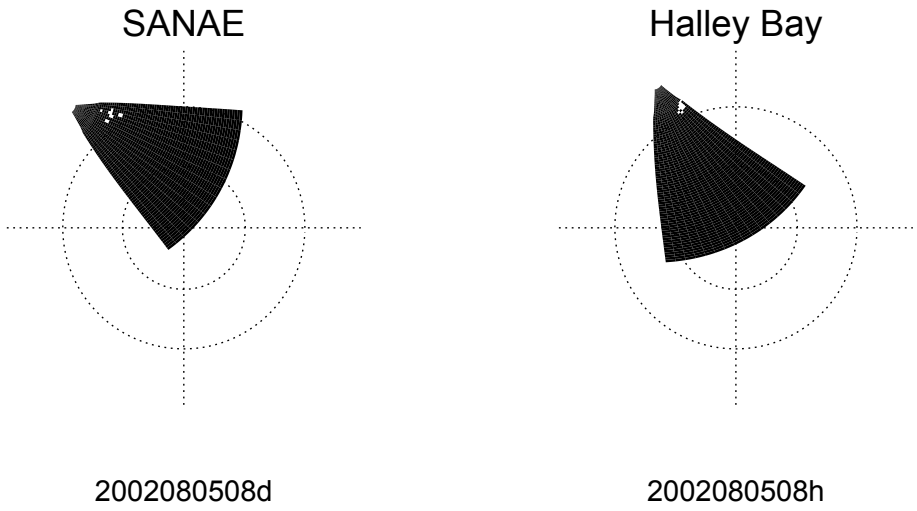

Figure 14.14: Locations of pulsation events in SANAE and Halley Bay data for 5 August 2002.

finder located pulsation events in both radars and the location of pulsation events is shown in figure 14.14. This data were then used in the merging process outlined in chapter 12 and the results are shown below. It should be noted that this event is from 2002 and does not form part of the 2004 data set that was processed as reported in chapter 11. There were no events in 2004 that showed a significant number of pulsations occurring in overlapping cells. This event is included to illustrate what can be done with merge events and how it differs from the single radar processing reported so far [28], [80] and [46].

14.2.1 Single radar observations

Each radar in the SuperDARN network is able to measure the line-of-sight velocity of the irregularities in the beam. The velocity of the radar is given as

$$V_r = V_i \cdot \mathbf{r} = V_i \cos(\theta_i - \theta_r) \tag{14.1}$$

where V_r is the velocity measured by the radar, V_i is the velocity of ionospheric irregularities, $\mathbf{r}$ is a unit vector in the direction of the bearing of the line-of-sight of the radar cell measured east-of-north where θ_r is the bearing angle of the radar cell and θ_i is the direction of the irregularity motion.

If the radar measures a uniform motion across its field of view then the measured velocities in each cell will vary according to the cell bearing. Some authors, [51] and [28], have tried to model this variation from single radar measurements but did not include any possible amplitude and phase variation of the irregularity motion when making the fit. Ponomarenko et al, [46], took a typical field line resonant behaviour, i.e., a peak in amplitude and a 180° phase change across the resonance, and tried to fit a single radar set of observations to his model. They were able to improve on the uniform motion fit using equation 14.1 and model the main features observed in the data but there were still

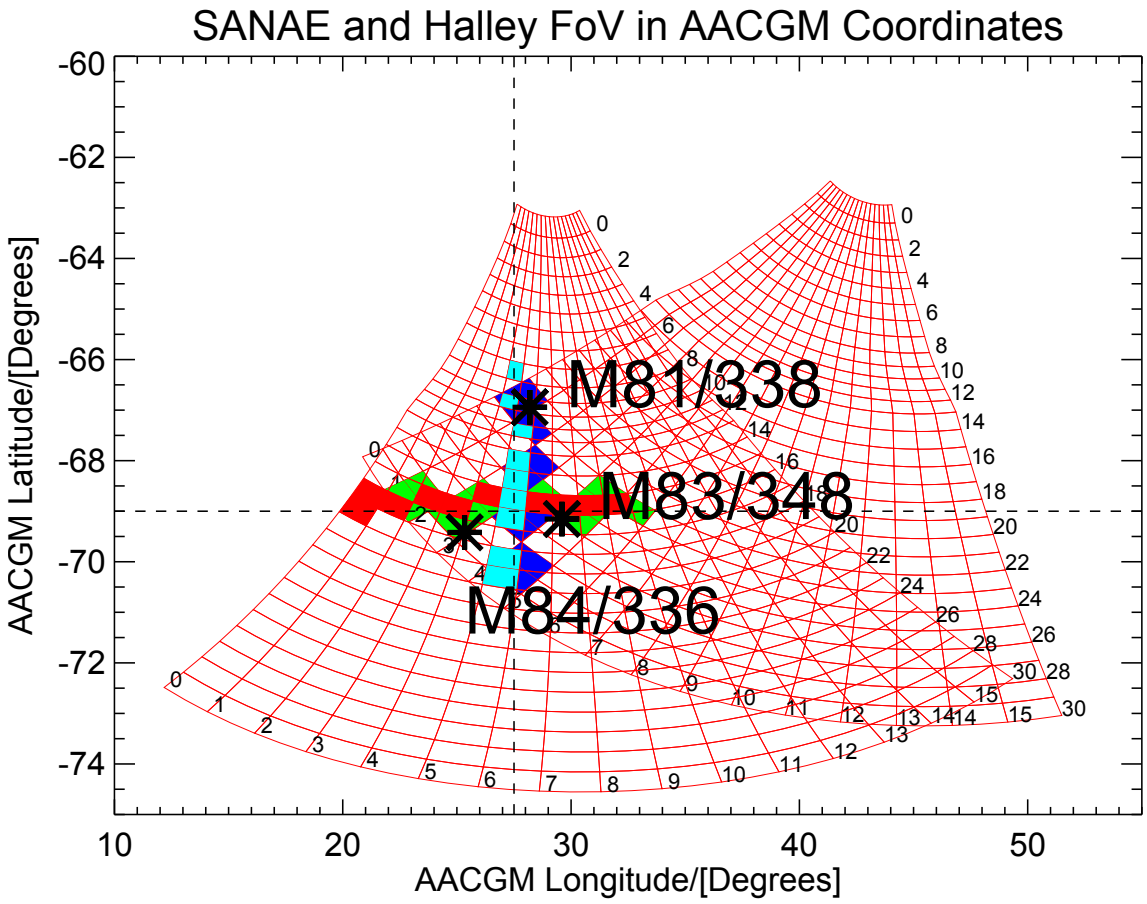

Figure 14.15: SANAE and Halley Bay radar field of view in AACGM coordinates. The high lighted cells from the two radars correspond to lines of constant longitude and latitude. Also shown are the local BAS LPM sites.

differences between the model and the data.

A latitude and longitude cross of overlapping radar cells in the Halley and SANAE radar was chosen along lines of 27.5° AACGM longitude and −69.5° AACGM latitude. The cross with the cells from each radar is shown in figure 14.15.

A electric field of field line resonant pulsation will vary along a line of longitude as is outlined in section 5.3.2. The radar will be able to measure the $\mathbf{E} \times \mathbf{B}$ drift from these electric fields. A radar cell that is directed poleward will observe the $\mathcal{E}_\phi$ perturbation which is indicative of the fast mode while toroidal directed cells will observe the $\mathcal{E}_\nu$ perturbation that is associated with the Alfvèn field line resonant pulsation.

Longitude line

A contour map of the pulsations that occurred in each radar for the longitude line is shown in figure 14.16. The bearing angles for each of the cells of the longitude line are shown in figure 14.17

Figure 14.16 shows that both Halley and SANAE have peaks as a function of latitude with

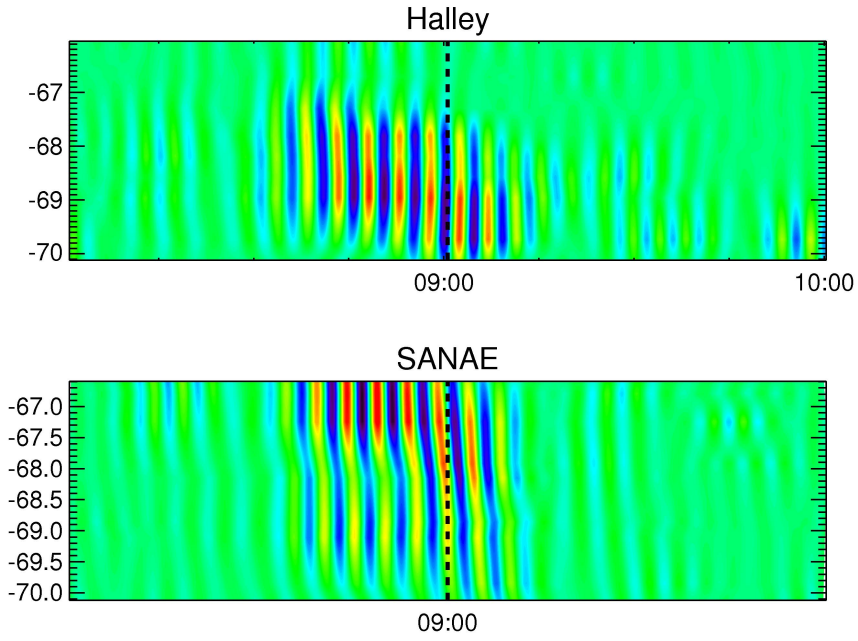

Figure 14.16: Pulsations from cells along a line of constant longitude for Halley Bay and SANAE as a function of time.

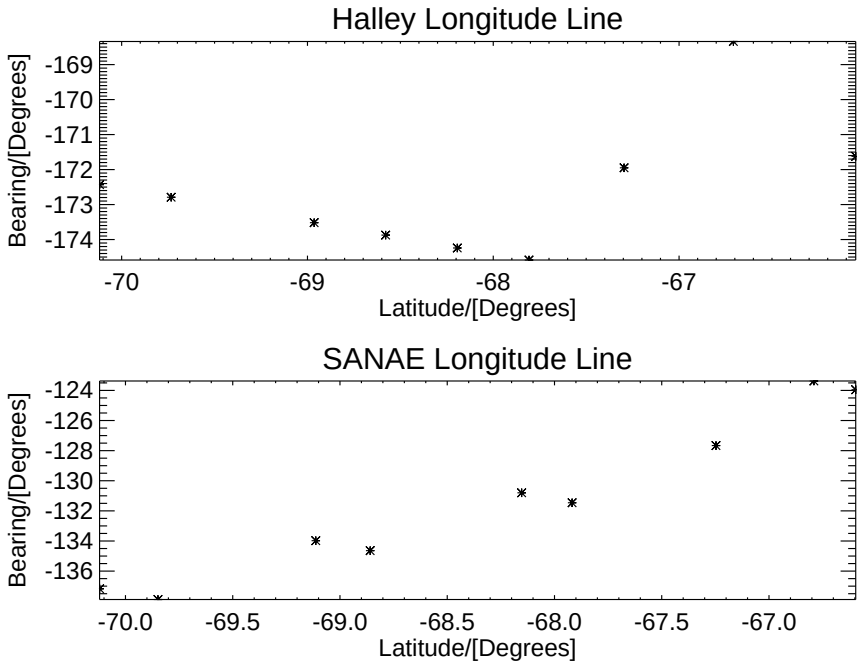

Figure 14.17: The bearing angles for the cells in the Halley Bay and SANAE longitude line.

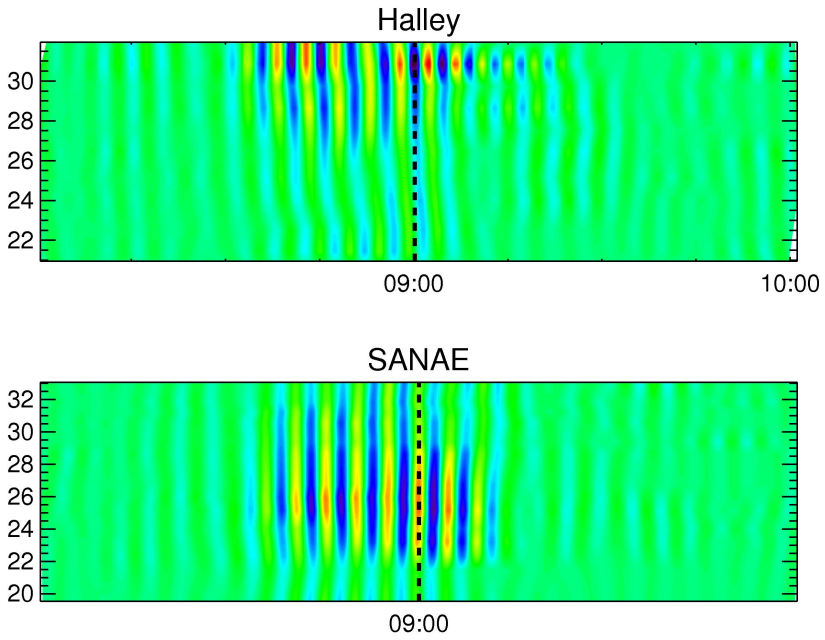

Figure 14.18: Pulsations from cells along a line of constant latitude for Halley Bay and SANAE as a function of time.

the peaks occurring at different latitudes The dip in figure 14.16 of the SANAE pulsation at $-68.5°$, which is from cells with a bearing of approximately $-130°$, indicate that these cells are directed orthogonal to the irregularity motion. From this the irregularity motion has a bearing of $140°$. The Halley pulsation has a bearing between $-168°$ and $-175°$ and the amplitude of the pulsation peaks in more eastward directed cells that is, the cells are close to poleward. This indicates that the irregularity motion is east of south similar to the SANAE results.

The dotted line at 9 UT in figure 14.16 indicates phase change as a function of latitude. There is no marked change in phase in the data. This is attributed to the fact that the cells are directed poleward thus they are not observing the motion due to $\mathcal{E}_\nu$. The SANAE data, however, does indicate a phase change. This is due to the fact that the cells are more toroidally directed, that is between $-123°$ and $-137°$ and have a greater toroidal component. associated with field line resonance.

Latitude line

A contour map of the pulsations that occurred in each radar for the latitude line is shown in figure 14.18. The bearing angles for each of the cells of the latitude line are shown in figure 14.19.

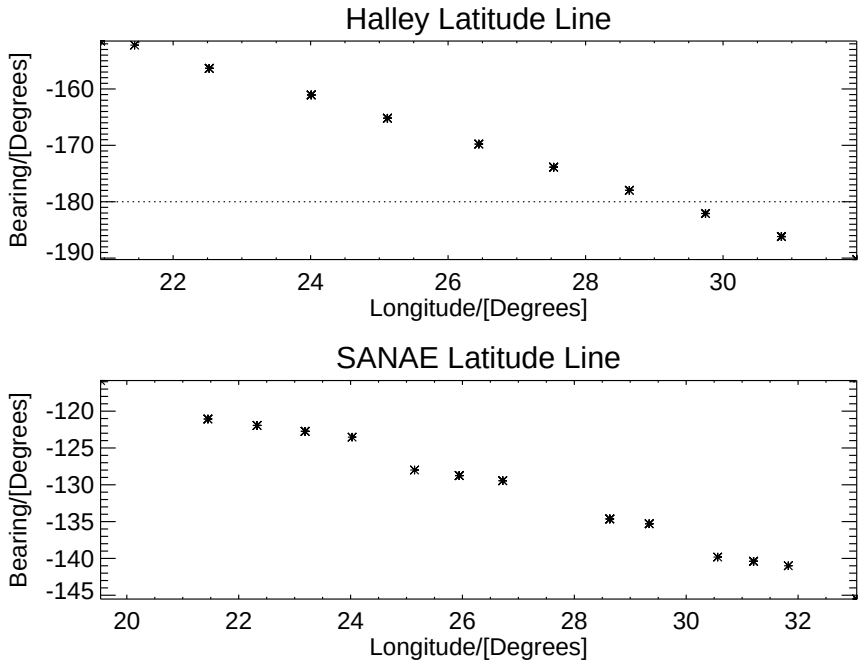

Figure 14.19: The bearing angles for the cells in the Halley Bay and SANAE latitude line.

The Halley bearings in figure 14.19 have been unwrapped to show the trend. The dotted line indicating the poleward direction. The pulsation amplitude for the Halley measurements falls off the more westward the cells are directed similar to the longitude line analysis but the SANAE pulsation shows a peak at 26° longitude which is in a direction of approximately $-130°$ which is in contrast with the findings of the longitude line analysis.

A full two dimensional pattern of the irregularity velocities are needed to resolve these differences. Single radars are unable to account for all the variations as was found in the fitting done by Ponomarenko et al [46]. The merge process of chapter 12 makes no assumption of the motion of the irregularities but rather removes the radar's directional characteristics from the data. The resulting merged data are then only a function of the irregularity velocity dynamics.

14.2.2 Merged radar data

The data for the overlapping cells were preprocessed using the method of section 12.2. The resulting per second data could be used in equations 12.1 and 12.2 to give the toroidal and poloidal components. Using these orthogonal components you can calculate the pulsation polarisation characteristics [48]. The angle of the major axis and the ellipticity indicate the relative difference in amplitude of the two components and the phase difference between the components respectively. In figure 14.20 , the two components that make up the

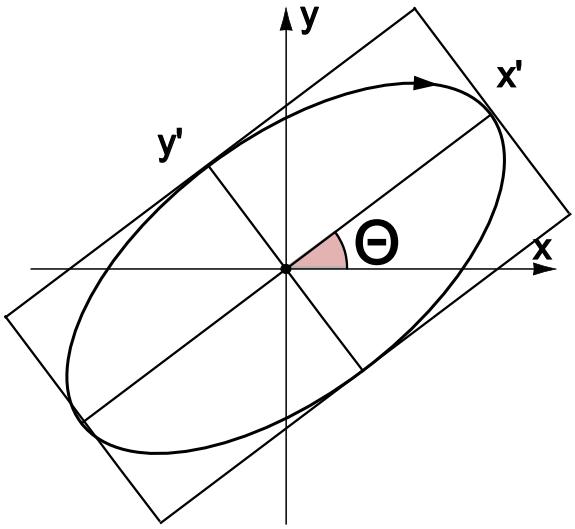

Figure 14.20: Polarisation ellipse angle of the major axis given by θ and the amplitudes of the major and minor axis given by y' and x'.

hodogram can be represented by

$$\begin{aligned} tor &= T\exp[-\imath(\omega t - \phi_t)] \\ pol &= P\exp[-\imath(\omega t - \phi_p)] \end{aligned}$$

where *tor* and *pol* are the toroidal and poloidal components, T and P and the amplitudes of the components, ω is the pulsation frequency and ϕ_t and ϕ_p are the phase constants of each of the components. The ratio of T to P will determine θ and $\phi_t - \phi_p$ will determine the ellipticity (y'/x'). The direction of the major axis is also the direction of the motion of the irregularities.

14.2.3 Characteristics of events

Polarisation

The toroidal and poloidal pulsations from the same longitude and latitude lines from figure 14.15 and shown in figures 14.21 and 14.22.

The data shown in figure 14.25 shows the hodograms for 27.5° longitude and latitude varying from 66.5° S to 72.0° S AACGM.

The average ellipticity for the period 08:30 to 09:00 UT is shown in figure 14.20. The closer the ellipticity is to 0 the greater the toroidal component is compared to the poloidal. The maximum value is ±0.5 which indicates the poloidal component is at most half the toroidal component. 55% of the points in the plot lie in the range [-0.15:0.15].

The angle of the major axis is shown in figure 14.24 where 77% of the values lie in the

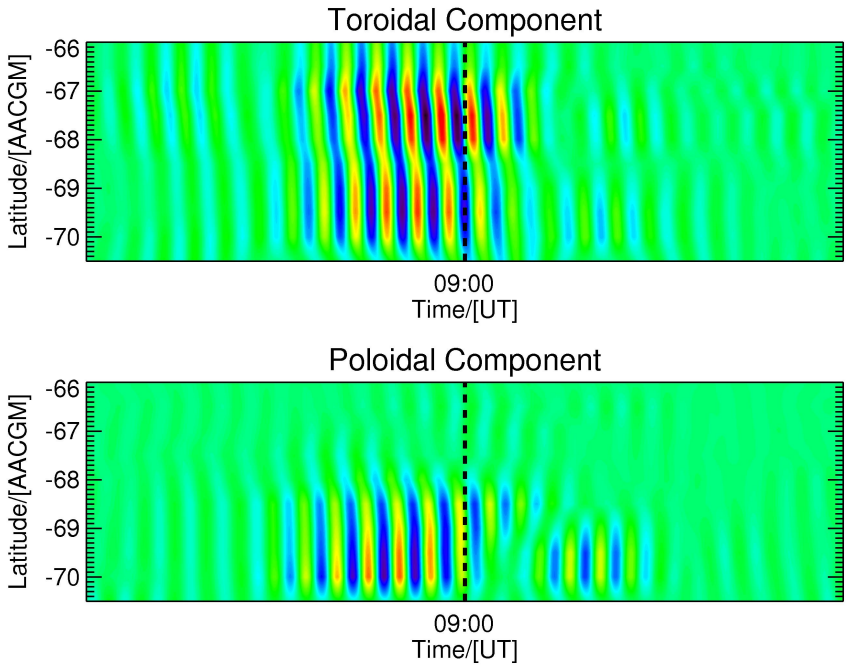

Figure 14.21: The merged poloidal and toroidal component for a line of constant AACGM longitude.

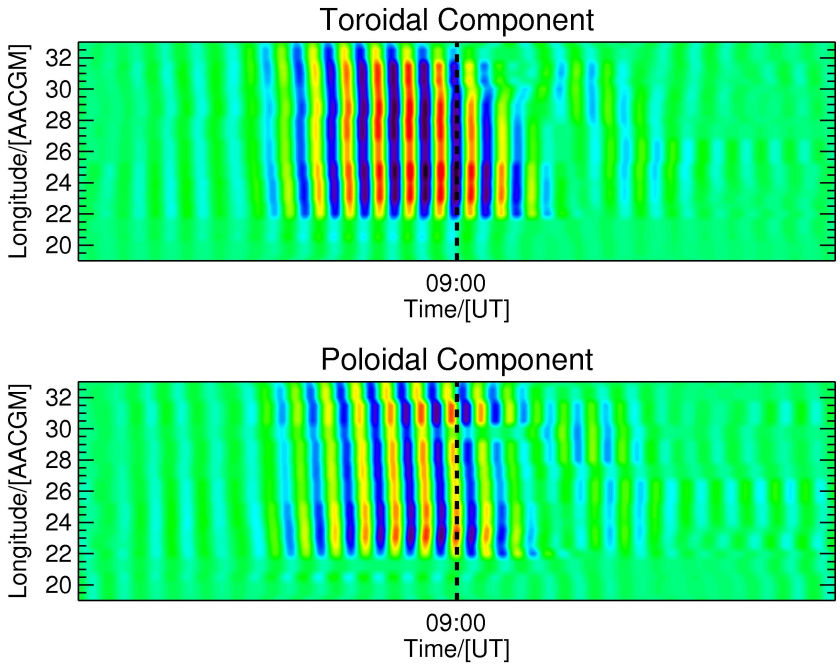

Figure 14.22: The merged poloidal and toroidal component for a line of constant AACGM latitude.

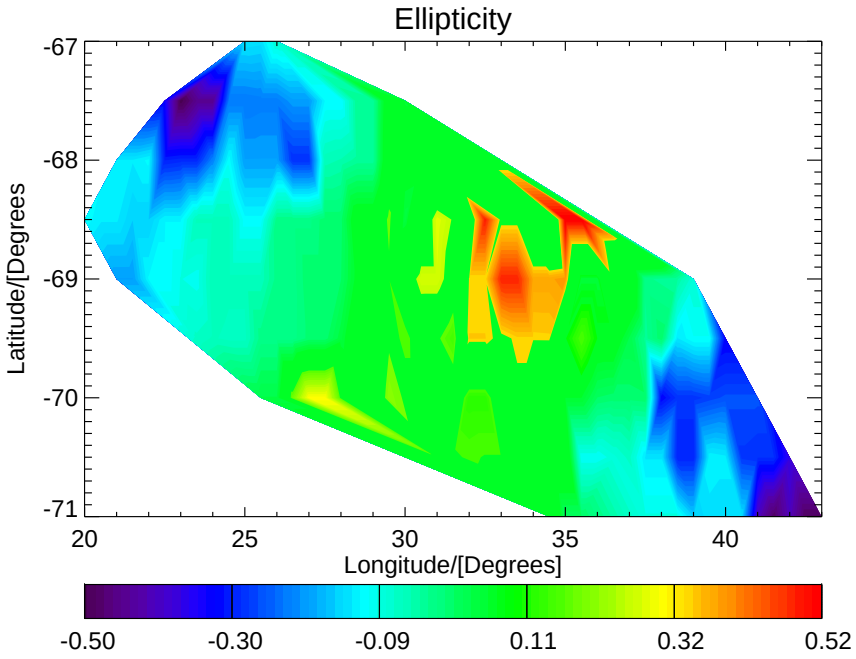

Figure 14.23: The ellipticity for the merged data.

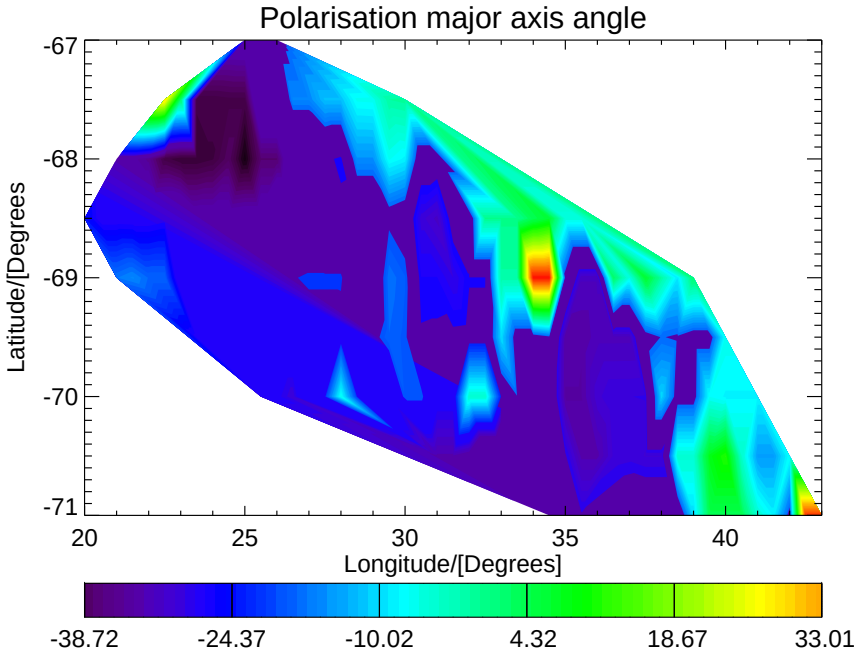

Figure 14.24: Angle of the major axis (θ) for the merged data.

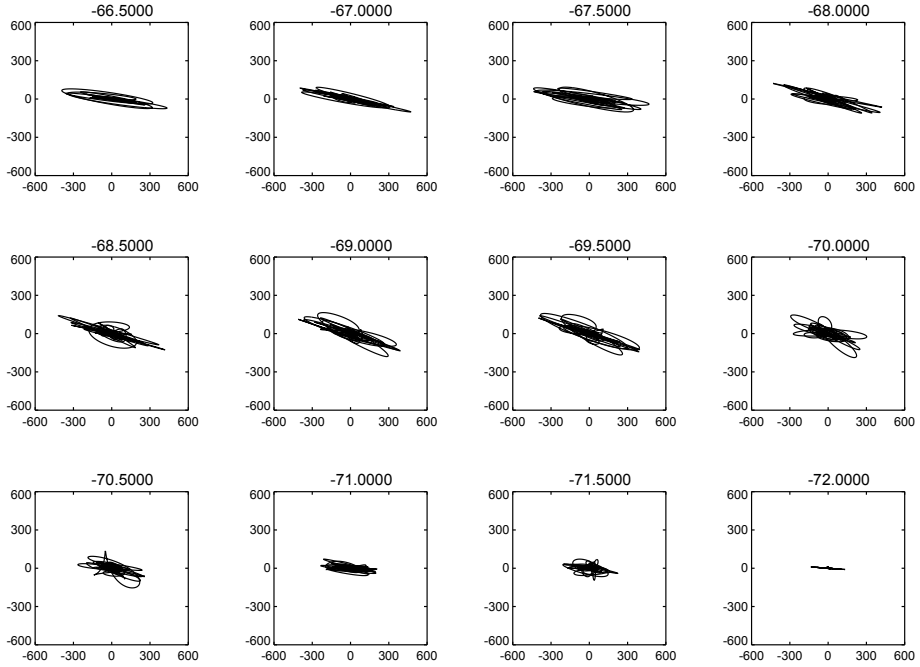

Figure 14.25: Hodograms for 5 August 2002. The plots are for 27.5° longitude AACGM and vary in latitude from 66.5° S to 72.0° S.

range $[-40° : -10°]$. These angles give bearings of $[100° : 130°]$ measured east of north. This is consistent with the finding of the single radar observations of section 14.2.1.

At lat:lon $-70° : 27°$ there is a small area of smaller directed motion in figure 14.24 together with a change in the sense of polarisation in figure 14.23 in the same area. This is the same place as the unexplained velocity measurements in figure 14.18. It appears that during that time the irregularity motion changed narrowing the angle between the motion and the beam direction. This would account for the increase in amplitude measured at that time. This area is towards the poleward edge of the data set and so there is no radar data at other locations for more information.

From figure 14.25 and the ellipticity values in figure 14.23 it is clear that the toroidal component of the signal is stronger than the poloidal signal. A strong toroidal velocity implies that there is a strong poloidal electric field ($\mathcal{E}_\nu$) in the ionosphere. A strong $\mathcal{E}_\nu$ means that there is a strong toroidal magnetic field $\mathcal{B}_\phi$. Chapter 4 showed that during a field line resonant pulsation event, the compressional pulsation couples with the resonant field lines and drives the strong toroidal pulsation that is observed. The driving pulsation, that is the poloidal component, was smaller and more constant in amplitude with latitude.

Amplitude and phase

The analytical signal was then calculated and the amplitude and phase of the toroidal component is shown in figure 14.26. The amplitude and phase data of figure 14.26 is typical of a field line resonant pulsation and follows the form of the theoretical characteristics of

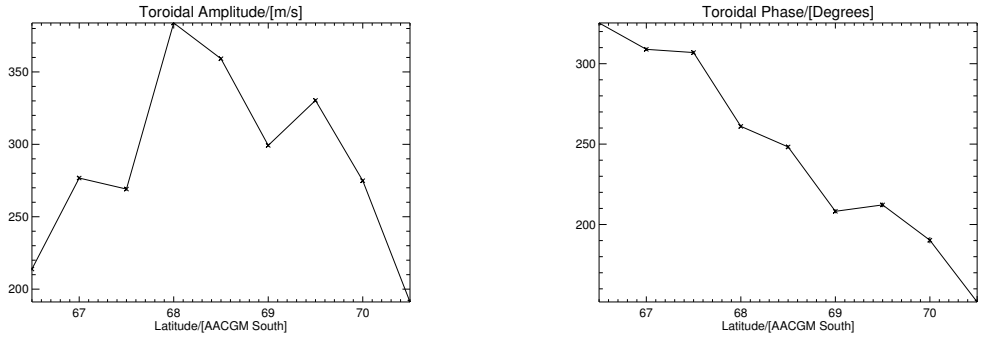

Figure 14.26: Amplitude and phase of the toroidal component of the data in figure 14.25 at 09:05 UT.

figure 5.6. Both the toroidal and poloidal perturbations in figure 14.22 show a phase change with longitude. The peak and trough lines slope from left to right suggesting a phase propagation towards lower longitudes, that is westward. The magnetic local time of the region is dawn (30°longitude at 09:00 UT is 06:00 MLT) so the propagation is tailward. This is confirmed by the two ground BAS low power magnetometers M84/386 and M83/348. M83/348 leads M84/386 by 90° in the x component and 50° in the y component.

The magnitude of the pulsation as well as a hodogram for each LPM station is shown in figure 14.27 for comparison. The lower latitude station (M81/338) has a lower amplitude as well as the angle of the major axis is different to the other two stations. This difference in orientation is further indication of the latitudinal phase difference that clear in figure 14.21 of the merged radar data. The difference in ellipticity between M83/348 and M84/386 indicates that the ratio between the magnitude of the y and x components is different at the two longitudes showing that there is a longitudinal profile to the amplitude of the x component. The components here are ground based magnetic coordinates and are thus rotated by 90° to GSM coordinates.

14.2.4 Conclusion

The field line resonant characteristics of figure 5.6 are governed by $g(\nu)$ in equation 5.5. For a specific event this is determined by the Pedersen conductivity (Σ_P). If Σ_P is low enough, the resonance is spread over more latitudes and the radar is able to observe the amplitude and phase structure of the pulsation as has been shown in this section. Using the method outlined in chapter 12 to merge the data and to obtain the poloidal and toroidal electric fields in the ionosphere, we conclude that this is firstly a field line resonant pulsation, due to the latitudinal amplitude and phase characteristics, and further that due to its occurrence at MLT dawn and the anti-sun-ward propagating phase with longitude that the driver is the Kelvin Helmholtz instability.

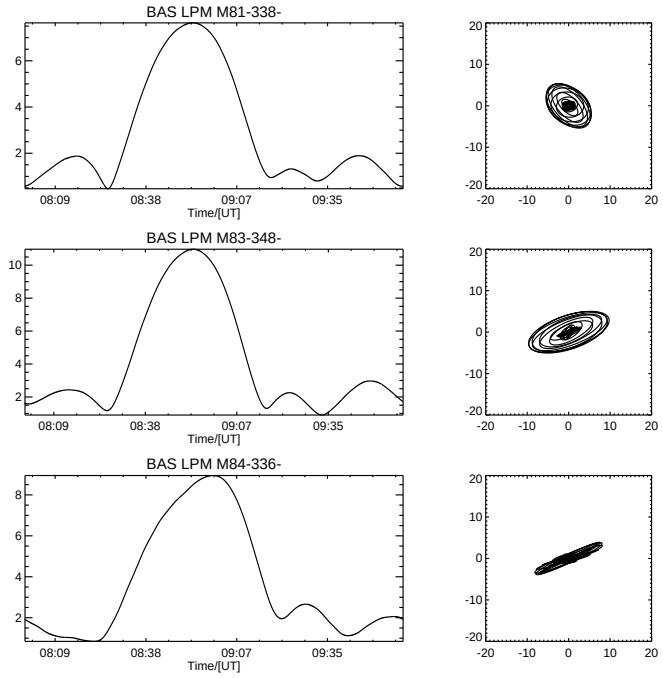

Figure 14.27: The amplitude and hodogram for the BAS LPM sites within the radar field of view.

14.3 Aliasing on 4 April 2004

The pulsation finder located what is tagged as a Pc5 pulsation occurring in beam 1 of the Halley Bay radar at range gate 9 at 18:00 UT on 4 April 2004. Further investigation of this event showed that the radar was in a special sounding mode where certain beams were being oversampled[1] with beam 1 being sampled at 99.2 s intervals and beam 2 at 16.5 s intervals. The data for the two beams are shown in figure 14.28.

It is clear that there is a much higher frequency pulsation present in the data of beam 2. The radar data are compared with geostationary satellite data and solar wind data to ascertain why two different signals were observed in the radar.

14.3.1 Spectra for the radar data

The data from beam 1 was sampled at 99.2 s intervals giving a Nyquist frequency of 5 mHz. The spectrum for this beam is shown in figure 14.29. The peak in the spectrum is at 1.4 mHz.

The data on beam 2 was sampled at 16.5 s intervals giving a Nyquist frequency of 30.3 mHz. The spectrum for the beam is shown in figure 14.30. The spectrum peaks between 11 mHz and 12 mHz.

[1]See section 6.8 for an example of beam oversampling.

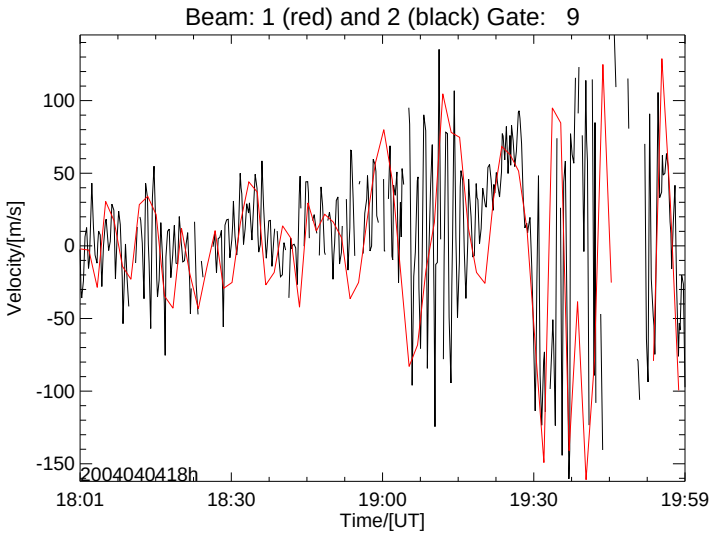

Figure 14.28: Doppler velocity data from Halley Bay on 4 April 2004. The red trace is for beam 1 and the black trace is for beam 2. Both plots are for range gate 9. This is an example of aliasing due to undersampling.

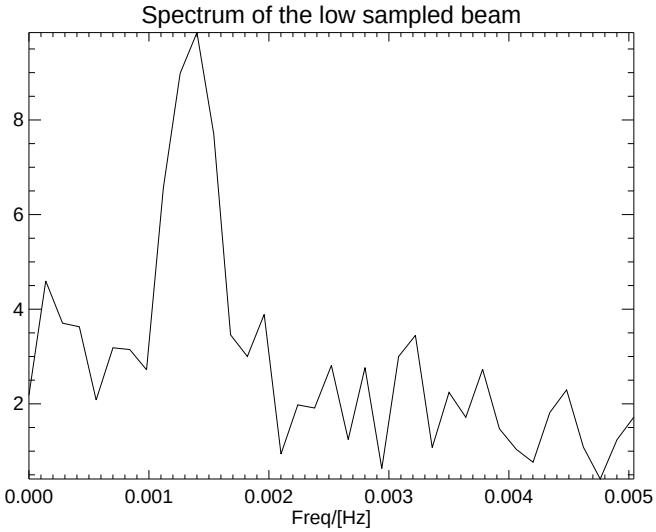

Figure 14.29: Spectrum of beam 1 range gate 9 for Halley Bay on 4 April 2004.

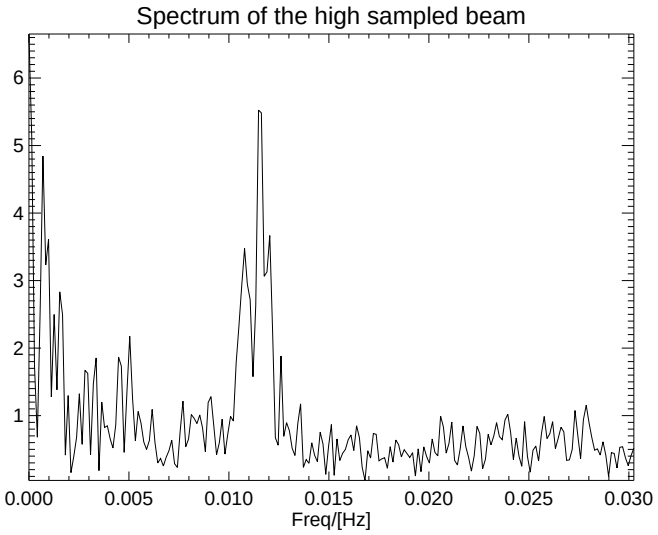

Figure 14.30: Spectrum of beam 2 range gate 9 for Halley Bay on 4 April 2004.

14.3.2 Other instruments

The location of the magnetic field line that passes through these cells traced into the GSM $x - y$ plane is shown as the black line in figure 14.31. The closest geostationary satellite is GOES 12 and is indicated in figure 14.31 in red. The figure also shows the position of ACE in the solar wind.

The data for the GOES 12 magnetometer is sampled at 60 s intervals giving a Nyquist frequency of 8.3 mHz (figure 14.32). There is a peak in the B_y spectrum between 5 mHz and 6 mHz

The data for the ACE solar wind satellite is sampled at 64 s intervals giving a Nyquist frequency of 7.8 mHz (figure 14.33). There is a peak in the v_z data between 4 mHz and 5 mHz.

14.3.3 Discussion

If a signal is sampled below the Nyquist frequency a peak will appear aliased in the spectrum of the data. Given a signal with frequency f_s sampled such that the sampling Nyquist frequency f_n is less than f_s, the peak in the spectrum will appear at $2f_n - f_s$. If $f_s > 2f_n$ then the peak is wrapped again and will appear at $f_s - 2f_n$.

The four different measurements of the same event are summarised in table 14.1. Here it is clear that although each different instrument shows a different peak (f_p), each of these peaks match the theoretical peak (f_{s_T}) if the original signal was a 11.5 mHz pulsation and then sampled with each of the instruments' sampling period.

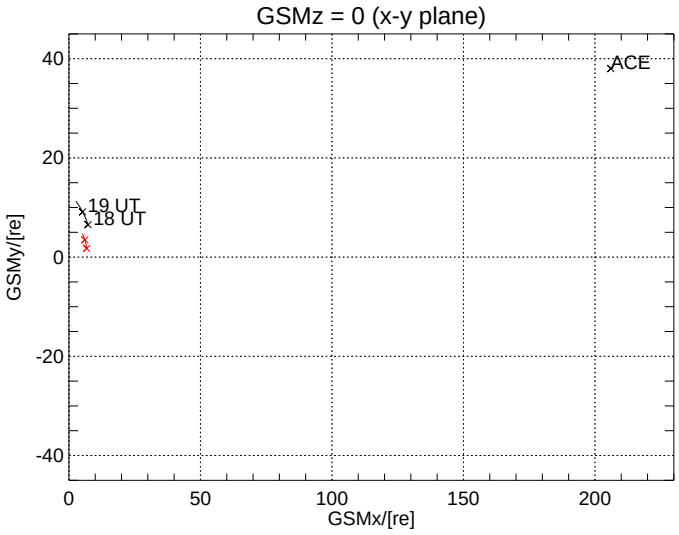

Figure 14.31: The GSM $x - y$ plane for 4 April 2004. The locations of the Tsyganenko field line (in black), GOES 12 (in red) and the ACE satellite in the solar wind are indicated.

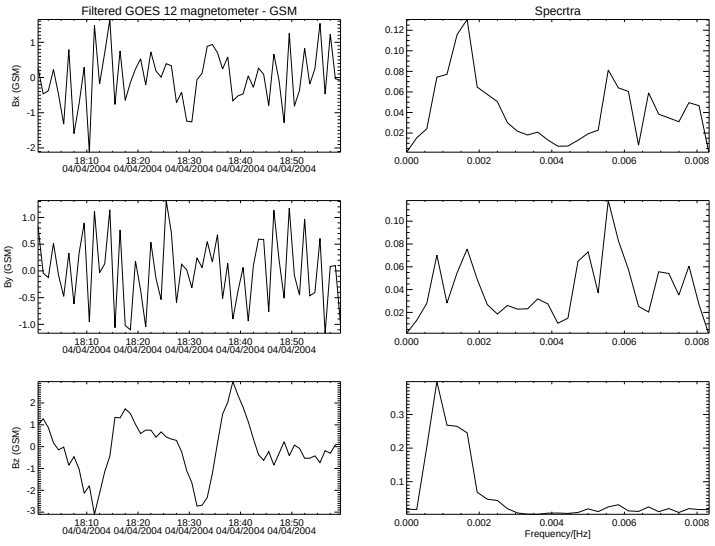

Figure 14.32: GOES 12 magnetometer data with the spectra shown in the right hand panels.

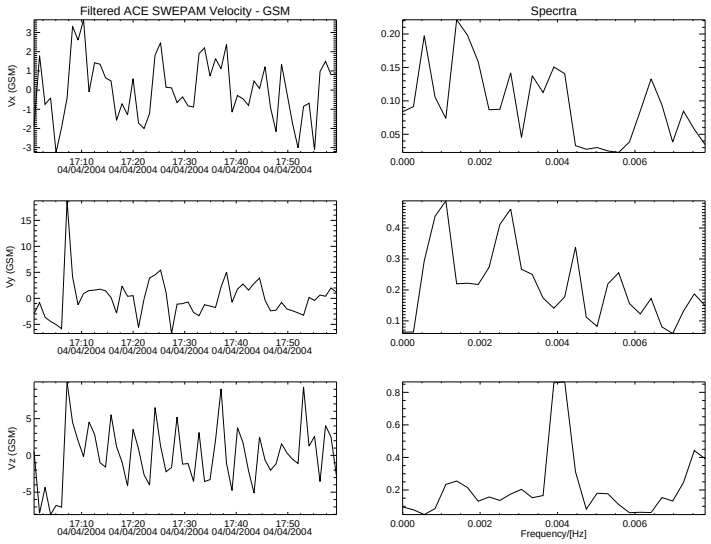

Figure 14.33: ACE SWEPAM solar wind velocity data.

Instrument	$f_s/[mHz]$	$T/[s]$	$f_n/[mHz]$	$f_p/[mHz]$	$f_{s_T}/[mHz]$
Radar Beam 2	11.5	16.5	30.3	11.5	11.5
Radar Beam 1	11.5	99.2	5.0	1.5	1.5
GOES 12	11.5	60	8.3	5.5	5.1
ACE SWEPAM	11.5	64	7.8	4.5	4.1

Table 14.1: Spectral peaks and aliased frequencies for the four different measurements. f_s is the actual signal frequency, T is the instrument sampling period, f_n is the instrument Nyquist frequency, f_p is the peak from the FFT spectrum and f_{s_T} is the theoretical frequency peak that would appear if the signal f_s is sampled with a period T, that is $f_{s_T} = 2f_n - f_s,\ f_s > 1 \times f_n$ or $f_{s_T} = f_s - 2f_n,\ f_s > 2 \times f_n$.

This event is included to illustrate that the radar does not have an analog anti-aliasing filter at its input and so care must be exercised when interpreting the pulsation results.

14.4 Sounding frequency changes on 5 April 2004

The convection maps produced by the SuperDARN network require as many data points as possible. The FITACF process rejects data that it considers noise. The SuperDARN radars have the ability to change their transmission frequency at any stage of the sounding. This is often done to try and maximise the amount of scatter observed by the radar so as to provide as many data points for the convection analysis.

The bar at the top of the summary plot in figure 14.34 shows that there were six different transmission frequencies during the four hour period. It is expected that each frequency travels on a different path. In this section we study the effects of changing the frequency on the path using ray tracing.

14.4.1 Ray tracing

Ray tracing was done on a modelled ionosphere with the signal originating at Prince George and propagating polewards in a direction roughly parallel to radar beam 8. The ionosphere was constrained with a $K_P = 2$ and a sunspot number of 55. The results for a 10 MHz and 14 MHz signal are shown for 02:00 UT in figure 14.35.

14.4.2 Data

A scaled line plot of the velocity parameter during the same period is shown in figure 14.36. Figure 14.36 shows clear pulsation characteristics during the four hour period. The pulsations are present in 14 - 15 MHz scatter as well as in the 10 - 11 MHz scatter after the frequency was changed at 02:30 UT. The horizontal line is at range gate 30 and the data from this range is shown in figure 14.37. It is clear that the pulsation signature is continuous across the frequency switching at 02:30 UT.

14.4.3 Discussion

Ground scatter flag

Data are tagged as ground scatter if the Doppler velocity is low enough and the spectral width is low. The pulsations in figure 14.36 are tagged as ground scatter in figure 14.34. The ray tracing in figure 14.35 shows that the higher frequency signals do indeed travel further through the ionosphere and so one would expect that the echoes would be from further range gates for the 14 MHz signal between 02:00 UT and 02:30 UT. During this

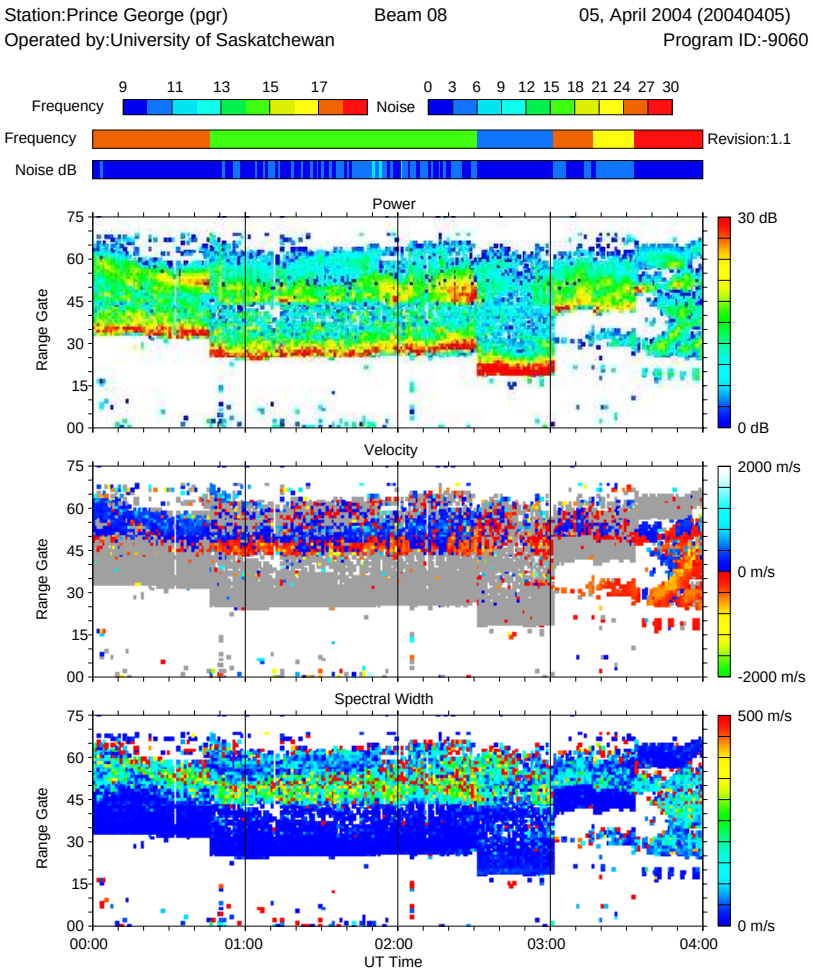

Figure 14.34: A summary plot of the Prince George radar on 5 April 2004 showing how the scatter changes for different transmission frequencies.

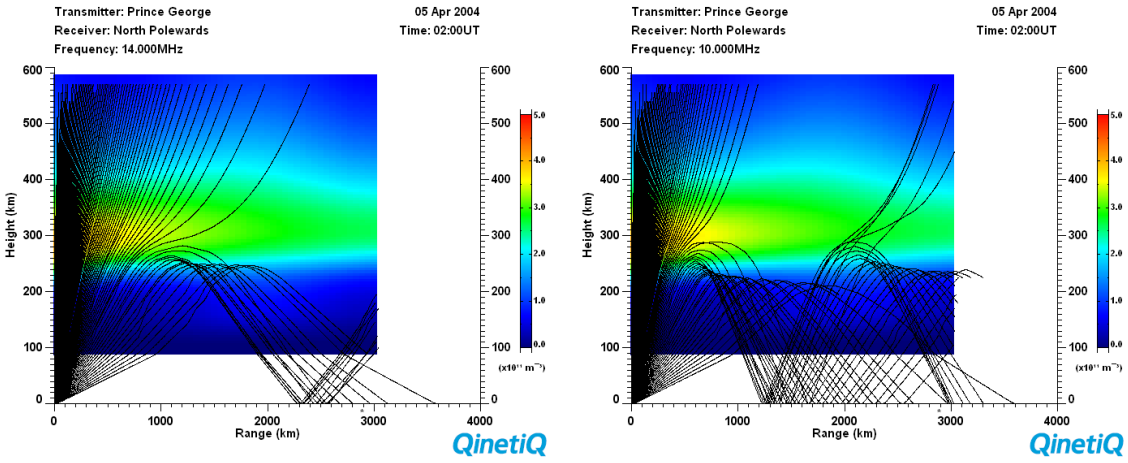

(a) (b)

Figure 14.35: Ray tracing a 14 MHz and 10 MHz signal through the ionosphere from Prince George polewards.

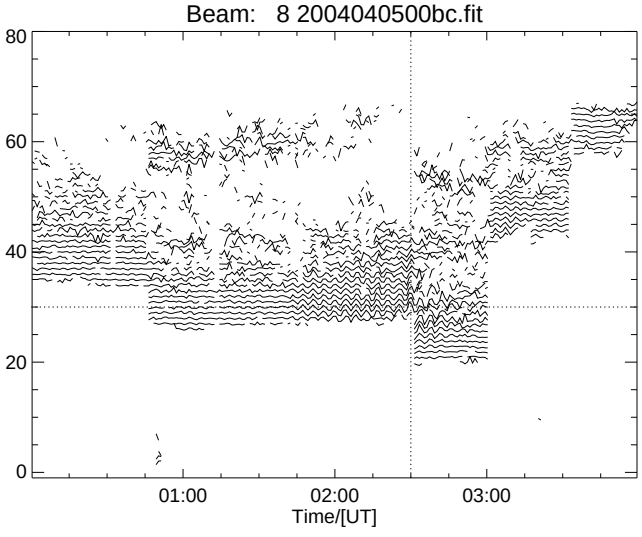

Figure 14.36: A line plot of the velocity parameter from the same time as the data shown in figure 14.34. The horizontal line is range gate 30. The vertical line is 02:30 UT.

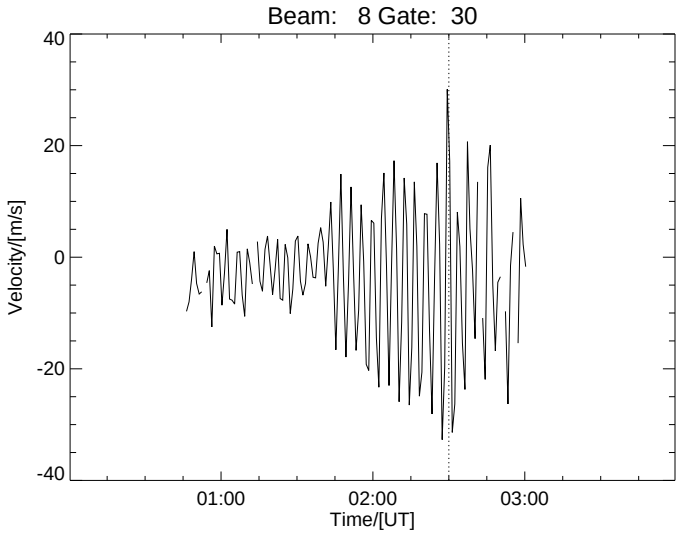

Figure 14.37: The velocity data from beam 8, range gate 30 on 5 April 2004.

time the first echoes come from range gate 25 which is 1205 km from the radar. A simple calculation using the ray paths in figure 14.35 shows that the half-hop range is 1176 km and the one-hop ground range is twice that. Similarly, the ray trace half-hop for 10 MHz is 650 km.

The ray tracing shows that it is not possible to receive ground scatter from the ranges as indicated in figure 14.34. This indicates that these echoes are likely to be ionospheric echoes that are incorrectly tagged as ground scatter. It must be remembered that ground scatter data are included in the pulsation finder algorithm.

Sounding frequency effects

The ray tracing showed that changing the sounding frequency changes the region of the ionosphere being observed. This has a negative impact on pulsation studies as it is not possible to build up long time series of data from the same region. Figure 14.37 shows that the pulsation is continuous across frequency changes if the scatter is from the same region. If there is no scatter, then the pulsation record is broken up as is the case with the rest of the ranges in figure 14.36.

Changing the sounding frequency is disruptive to pulsation studies and should only be undertaken when necessary.

Chapter 15

Conclusions

It is necessary to make observations across a large spatial extent to be able to understand the source of the MHD wave energy for pulsations and the way in which the MHD waves propagate through the magnetosphere. Ground based systems are limited in their ability to resolve fine spatial structures and spacecraft borne instruments are sparse and possibly moving with respect to the observational area. SuperDARN radars are able to observe pulsation signatures in the ionosphere and are thus not limited by the spatial restrictions of ground based instruments. Further, their observational area is vast and constant geographically, indicating that the radar network may be useful for studying the global dynamics of pulsation events. This thesis investigated the relative usefulness of SuperDARN radar data for global pulsation studies.

15.1 Summary of the thesis

Chapter 1 gives an historical overview of pulsation research and lays the platform for the topic of this thesis, that is, the usefulness of SuperDARN radar data for pulsation studies. Chapters 2 and 3 show how pulsations can be thought of as magnetohydrodynamic waves propagating through the magnetosphere and stetting up standing waves between the northern and southern ionospheres to form what is termed as the field line resonant structure. The box model of chapter 4 can be used to get an understanding of the pulsation dynamics but a more realistic dipole model of chapter 5 should be used to get quantitative results. Chapter 5 also shows how the Pedersen conductivity (Σ_P) is by far the most significant parameter that determines the ability of the radar to observe pulsation signatures. If Σ_P is too high then there will be no first order pulsating electric field in the ionosphere and further the resonance will be narrow such that the radar's spatial sampling may not be able to resolve the structure.

Chapter 6 introduced the SuperDARN radar and discussed its operation as it is the primary instrument for the data in this thesis. Further instruments and their data are introduced in chapter 7.

The significance detector is introduced in chapter 8 where it is used to reduce the noise in the radar data and detect significant peaks in amplitudes of FFT spectra.

Chapter 9 discusses the characteristics of clean records. It was found that the temporal variability of the number of clean records best correlated with the temporal variability of the IMF B_z component. It was also found that there are more clean records directed polewards than any other direction. This is due to the fact that there are more poleward directed cells in the radar network than any other direction.

As the data set is so vast (1200 records per radar in every two hour period) an automated pulsation finder was developed and the process is explained in chapter 10. The results of the pulsation finder are presented in chapter 11. It was found that the average daily distribution of pulsation events, shown as a function of pulsation frequency, followed $1/f$ distribution. It was also found, however, that the standard deviation of the average showed peaks close to the "magic" frequencies mentioned by Samson et al [52]. This indicated that on average there is more variation at these frequencies that any of the other pulsation frequencies measured. The occurrence of pulsations followed the clean scatter statistics both temporally and directionally telling us that the network is not suited for studying global pulsation dynamics because the variations in scatter dominates any variations in pulsation occurrence.

Chapter 12 shows how pulsation data from two overlapping radar cells can be merged to yield the poloidal and toroidal characteristics of the pulsation. Chapter 12 also discussed how data from overlapping radars should be preprocessed to prepare it for the merging calculations.

Chapter 13 filled a required space.

Chapter 14 shows some examples of the types of event analysis that can be done using the SuperDARN network. Data are presented from 2 September 2004 showing a pulsation occurring at two different frequencies. The data are compared with ground and satellite data and it is concluded that the higher frequency pulsation is possibly a higher harmonic of the lower frequency pulsation data. The higher frequency data is sparse in space and time and so a full characterisation of the event was not possible. There is an indication that the higher frequency pulsation may be of magnetospheric origin due to the high m number and sunward propagating phase. This event also highlights the ability of the radar to observe higher frequency pulsations that were not visible on the ground based data. On 4 April a beam that was sampled at 99 s intervals gave a pulsation with a spectral peak of 1.5 mHz. Data from an adjacent beam, being sampled at 16 s intervals, and satellite measurements at the same time showed that this peak is incorrect and is caused by aliasing. On 5 April pulsations were observed in Prince George data and using ray tracing calculations it was determined that the data were incorrectly tagged as ground scatter. Sounding frequency changes during the pulsation event also make it difficult to use the data for long time series analysis. Data from 5 August 2002 from the Halley Bay

and SANAE radars were merged using a high resolution approach to determine poloidal an toroidal pulsation characteristics of the event. The hodograms and the toroidal amplitude and phase characteristics indicate that this is a field line resonant event.

15.2 Summary of the results

The intent of this thesis was to determine the relative usability of SuperDARN radar time series data for global pulsation signature analysis. In this section, results and conclusions of novel work are presented.

15.2.1 Significance detectors

A review of the literature showed that there are no published automated pulsation finders for Pc5 pulsations in SuperDARN radar time series data. There are reports of pulsation finders for magnetometer data [17] and [44], but these data do not exhibit the problems that are experienced with radar data, namely, varying sampling periods and irregular points due to gaps in the data.

The tool used to detect the pulsations is a significance detector that detects peaks in the FFT spectra of the Doppler velocity data from the radar. The SuperDARN network was initially designed to map polar convection, and as such, is designed to receive echoes from open field lines. Pc5 field line resonant pulsations, as is shown in chapter 4, can only exist on closed field lines. This fact reduces the amount of usable data for the finder. Further, it is expected that the pulsation will manifest itself in the data as a periodic variation of the Doppler velocity. Outlying data points are thus removed using a further noise significance detector.

In order for an FFT spectrum to be calculated, there should be no gaps in the data and the data should be uniformly spaced. The SuperDARN data will only meet these criteria if there are no gaps. Gaps in the data are due the fitACF process or the echo is from an open field line or the data is considered to be an outlier. Gaps in the data can be interpolated using cubic splines. For this analysis, only records with less than 20% points missing were interpolated and used by the pulsation finder. This is clean scatter.

15.2.2 Scatter analysis

In order to determine if the pulsation dynamics that were identified by the pulsation finder were a result of the pulsation driving mechanism, or simply a consequence of the instrumental characteristics, the clean scatter for 2004 was characterised.

Characterisation of the temporal properties of the number of clean records from the network showed that the best correlation was with the IMF B_z component. A dynamic

spectrum of the IMF B_z showed the same peaks as the dynamic spectrum of the number of clean records during the year.

The poloidal and toroidal components of a pulsation can be used to determine if the pulsation event being observed is part of a field line resonant pulsation. A SuperDARN radar measures the line of sight component of the velocity of the ionospheric plasma. The pulsating electric field of the pulsation causes the plasma to $\mathbf{E} \times \mathbf{B}$ drift. If a radar beam is directed polewards then it is measuring the a toroidal electric field perturbation. Similarly a toroidally directed beam will measure the poloidal electric field. The scatter analysis showed that most of the clean cells are directed polewards as there are more poleward directed cells in the network

15.2.3 Pulsation finder

The daily average of the distribution of pulsation events showed that there were no preferred "magic" frequency peaks. The standard deviation of the average did show peaks near the documented "magic" frequencies. This indicated that there is more variation in the number of events at these frequencies than the other frequencies in the Pc5 band. These peaks were linked to events with a large number of contiguous cells.

The temporal variation in the number of pulsation events followed the IMF B_z component. This might lead one to believe that the pulsations are being modulated by B_z variations but this behaviour is actually a result of the clean scatter variations.

There were more pulsations found in poloidally directed cells. It is proposed that this is because of the fact that there are more clean records in the poloidal direction. Deconvolution of the scatter characteristics from the pulsation characteristics showed a peak in the toroidal direction associated with the Stokkseyri radar and this should be monitored for field line resonant pulsations.

The conclusion of this analysis is that the characteristics of pulsations identified by the pulsation finder are strongly modulated by the variations in the clean scatter and are thus not useful for global pulsation characterisation.

15.2.4 Merging

Velocity data are merged from overlapping radars to create polar convection maps. The merging routine averages the behaviour in time and space and is thus not suited for pulsation studies where the spatial and temporal variations may be averaged out. An instantaneous merging method was developed for pulsation studies. The merging method required the velocity data to be preprocessed by filling the data gaps with a two dimensional interpolation scheme and then resampling the data with one second resolution. This method can be used to merge data from overlapping radars with totally different sampling schemes and produce the poloidal and toroidal components of the pulsation.

15.2.5 Interesting events

A set of events were presented to illustrate some of the issues regarding using SuperDARN radar data for pulsation studies.

The first event shows that because the radar is measuring the pulsation in the ionosphere it is not subjected to the spatial filtering that limits ground based studies of pulsations, see section 4.5. In this event a pulsation was identified that showed the fundamental as well as possibly the third harmonic of a standing wave pulsation clearly visible in the radar data but only the lower frequency pulsation were observed on the ground. Both frequencies were observed simultaneously on the GOES12 satellite.

The second event presented shows how the merging method can be used to determine the components of the pulsation and confirm that this was a field line resonant pulsation.

The third event shows a pulsation that is occurring outside the Pc5 band but due to the low sampling rate of one of the beams, the pulsation is aliased into the Pc5 band. The radar was in a special mode where three beams were sampled at a much higher rate and were thus able to resolve the true pulsation perturbation frequency. This event illustrates that it is not possible to filter the pulsations with an anti-aliasing filter and so care should be taken in interpreting pulsation events and that, were possible, the higher the sampling rate the better.

The last event uses the fact that changing the sounding frequency of the radar can be used to show that ionospheric scatter was incorrectly tagged as ground scatter. Further, the incorrectly tagged ground scatter contained pulsations that were interrupted by the changing frequency making the data useless for long time series analysis. The event highlights the fact that pulsations can be observed in data tagged as ground scatter and that changing the sounding frequency results in breaks in the time series data.

15.3 Further work

15.3.1 Other significance detectors

The automated pulsation finder developed for this thesis is able to identify many pulsation events in SuperDARN data. The global characteristics of these events follow the spatial and temporal dynamics of the network rather than being indicative of the pulsation structure. A vast number of records were ignored by the pulsation finder as is shown in figure 9.3. Other significance detectors are able to work with sparse data [12] and it is suggested that these be investigated to determine if the unused data is less constrained by the network and are thus able to giver a better view of global pulsation dynamics.

15.3.2 Pulsation event studies

Although the events identified by the pulsation finder are not able to give global characteristics, the events, as was shown in chapter 14, do provide a interesting data set for pulsation research. It is suggested that the finder be extended to all the data of the network, not just 2004, and an events catalogue be generated for the pulsation community.

15.3.3 Real-time magnetospheric plasma densities

Cross phase analysis can be used to determine the natural resonant frequency of a field line spaced between two measurements [19]. If a pulsation can be identified automatically while the radar is sounding then the toroidal components, as a function of latitude, can be determined. The cross phase analysis can then be applied to the toroidal components and a real-time determination of the natural frequencies can be made. These measurements of the natural frequency can then be used to study plasma density variations along the field lines in the magnetosphere [74].

Appendix A

Glossary

AACGM	Altitude Adjusted Corrected Geomagnetic
ACF	Autocorrelation function
DARN	Dual Auroral Radar Network
FFT	Fast Fourier Transform
FIT	extension of the file containing the ACF fitted parameters
FITACF	the process of fitting an ACF
GSM	Geocentric Solar Magnetospheric
HF	High Frequency
HMO	Hermanus Magnetic Observatory
IAGA	International Association of Geomagnetism and Aeronomy
IDL	Interactive Data Language
MHD	Magnetohydrodynamics
RF	Radio Frequency
SHARE	Southern Hemisphere Auroral Radar Experiment
STARE	Scandinavian Twin Auroral Radar Experiment
SuperDARN	Super Dual Auroral Radar Network
WKBJ	Wentzel-Kramers-Brillouin-Jeffreys

Appendix B

Symbols

ρ	Density
$\mathbf{v} = v_x\hat{\mathbf{x}} + v_y\hat{\mathbf{y}} + v_z\hat{\mathbf{z}}$	Perturbation velocity
p	Pressure
B	Magnetic field strength
$\mathbf{B}$	Magnetic field vector
$\mathbf{E}$	Electric field vector
μ_0	Permeability of free space
γ	Ratio of specific heats
$\mathbf{b} = b_x\hat{\mathbf{x}} + b_y\hat{\mathbf{y}} + b_z\hat{\mathbf{z}}$	Perturbed magnetic field
$\mathbf{V}_A$	Alfvén Velocity
V_S	Sound Velocity
$\imath$	imaginary operator
$\mathbf{k} = k_x\hat{\mathbf{x}} + k_y\hat{\mathbf{y}} + k_z\hat{\mathbf{z}}$	wave number
m	wave number in the azimuthal direction
ω	perturbation frequency
θ	angle between the wave normal and the magnetic field
v_T	Transverse component of the perturbation velocity
v_L	Longitudinal component of the perturbation velocity
ξ	Perturbation displacement normal to $\hat{\mathbf{y}}$ and $\mathbf{B}$

η	Perturbation displacement perpendicular to $\hat{\mathbf{x}}$ and $\mathbf{B}$
ψ	Generalised perturbation pressure
x_T	Turning point in the magnetosphere
x_R	Resonance point in the magnetosphere
ζ	x coordinate transformation near the turning and resonance points
Ω_e	Electron gyrofrequency
Ω_i	Ion gyrofrequency
ν_e	electron collision frequency
ν_i	ion collision frequency
$\mathbf{J}$	Current density vector
σ	Conductivity
σ_P	Pedersen conductivity
σ_H	Hall Conductivity
Σ_P	Height integrated Pedersen conductivity
Σ_H	Height integrated Hall Conductivity
k_i	the imaginary part of the wave number
μ	dipole coordinate in the direction of the magnetic field
ν	dipole coordinate perpendicular to the magnetic field
ϕ	dipole coordinate measured as an angle in the equatorial plane
λ	geomagnetic latitude
L	L-shell
$z = \sin\lambda$	latitude coordinate substitution
$K = K_r + \imath K_i$	Normalised frequency with real and imaginary parts
K_0	Resonant normalised frequency
$\mathcal{E}_\nu$	Component of the perturbed magnetic field in the direction of ν given in dipole coordinates
v_{tor}	Toroidal component of ionospheric irregularity velocity
v_{pol}	Poloidal component of ionospheric irregularity velocity

Appendix C

Filtering

C.1 Introduction

Two types of filters were used extensively in this analysis. The first was a band limiting filter to restrict the pulsations to the Pc5 band (see section 1.1). The second was required for the determination of the analytical signal of a pulsation event where the pulsations are assumed to be monochromatic and in order to study the amplitude and phase characteristics of the signal the data were filtered with a narrow band filter.

C.2 Why use a FIR filter

As the data are discreete samples of the ionospheric echoes, digital filters are used. There are two types of digital filters available for analysis namely infinite impulse response (IIR) filters and finite impulse response filters (FIR) filters. IIR filters are more commonly used for digital filtering continuous-time signals whereas FIR filters are commonly used for data analysis as they can guarantee a linear phase response [43, ch 7].

C.3 Filter choice in this research

An FIR filter discrete approximation of a real filter. In figure C.1 and ideal low pass filter is shown in panel (a). In order to reproduce this ideal filter one would need and infinite number of points in the filter kernel as is shown in panel (b). A FIR filter kernel only has a finite number of points and so the infinite number of points are windowed in panel (c). The consequence is that there is now a high frequency ripple introduced to the ideal filter response. This high frequency ripple in the frequency domain can be removed using a low pass filter *of the frequency response*. This is achieved by multiplying the filter kernel with a suitably chosen window and is shown in panel (f). The result is a smoothed frequency response in panel (g). This type of filter is called the windowed-sync filter.

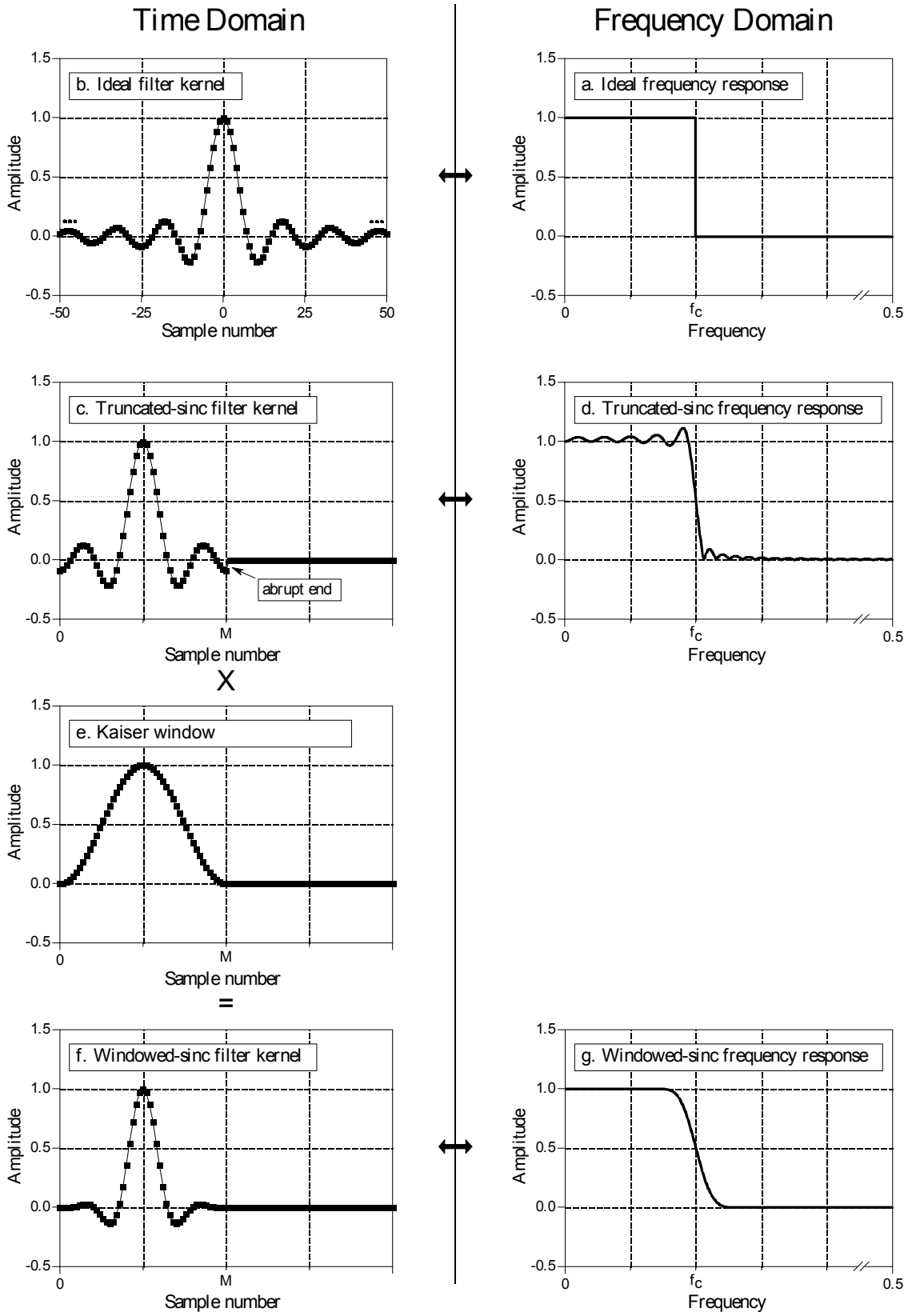

Figure C.1: A windowed sync filter [57, ch 16].

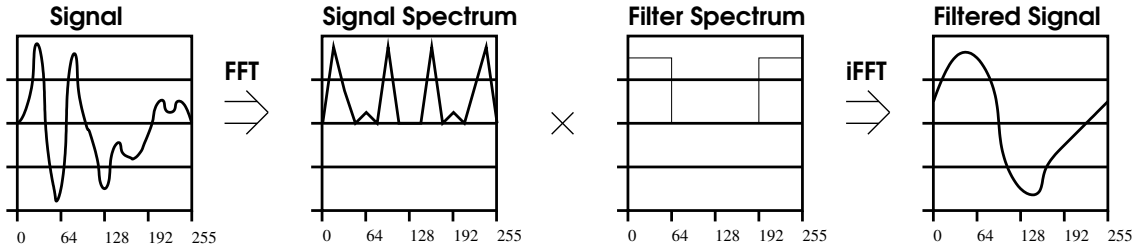

Figure C.2: A simple representation of how a signal is filtered in the frequency domain.

Kaiser found that a window based on the zeroth-order modified Bessel function of the first kind was much easier to compute [43, ch 7]. The window is parametrised by two parameters, M the length of the kernel and in turn the sharpness of transition and A that controls the shape of the kernel and in turn the ripple in the pass and stop band. Higher M gives a faster transition. Higher A gives less ripple.

The IDL *digital_filter* function returns that kernel values for a Kaiser window filter. Parameters for the function include the lower and upper cutoff frequencies as a function of sampling frequency and the two window parameter M and A. 50 was chosen as the default value for A in this analysis [1].

C.4 Time domain aliasing

Filtering of data without concern for time domain aliasing can yield erroneous data. Most filters are shown in the frequency domain where the spectrum of a signal is simply multiplied by the filter to reduce the unwanted components. An example is shown in figure C.2. This can be problematic due to the cyclic nature of the FFT. The Discrete Fourier Transform (DFT), of which the FFT is a variant, assumes that the data being transformed is repeated infinitely before and after the current data of interest. A transform pair that is of significance here is that multiplication in the one domain is equivalent to convolution in the other domain. If one sees filtering as simply multiplying the spectrum of the data with the desired filter response then it must be noted that convolution is being done in the time domain. Figure C.3 shows how this can give erroneous data. In this figure a data series of 256 points is convolved with a filter kernel of 65 points yielding a series of $N + M - 1 = 320$ points. This is known as linear convolution. If, however, one were to make use of the multiplication/convolution transform pair then the result is circular convolution which results in time domain aliasing also shown in figure C.3.

This presents a problem because a longer filter kernel (larger M) gives a faster transition between stop and pass band while a larger M also results in more time domain aliasing.

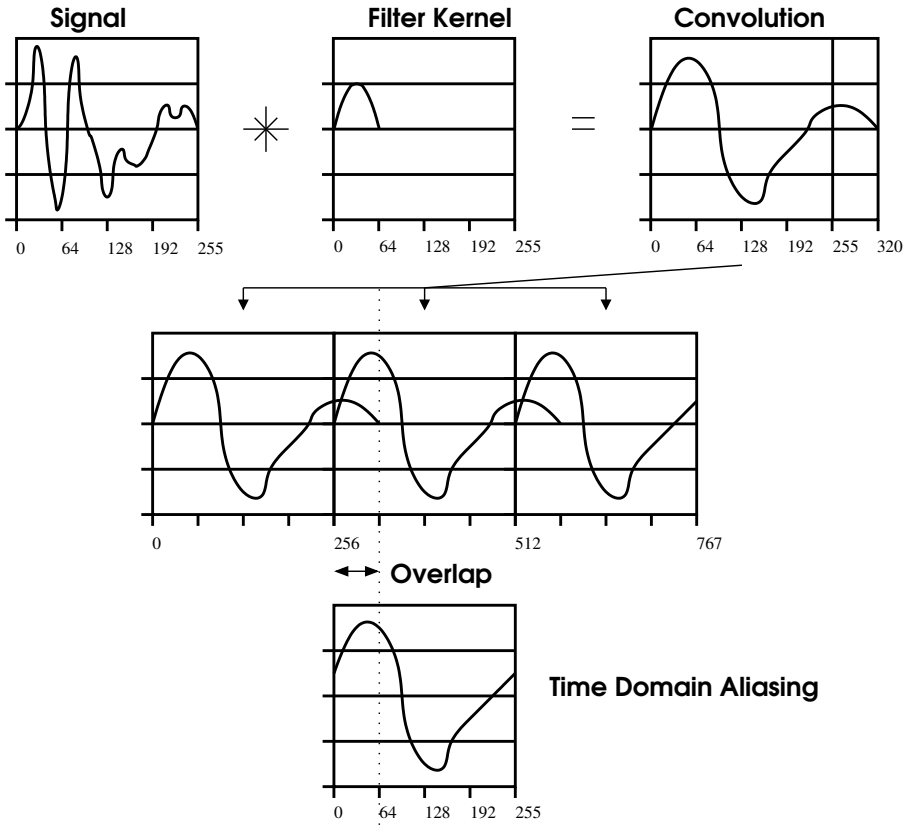

Figure C.3: Time domain aliasing.

C.5 IDL convolution options

Filtering in IDL is achieved by first creating the Kaiser window filter kernel and then convolving the kernel with the data using the IDL *convol* function. The if the data has N elements and the kernel has M elements then *convol* function always returns an array with M elements and not $N + M - 1$ elements are required by linear convolution. IDL has four ways to handle convolution.

1. The default way is that during the convolution whenever part of the kernel falls outside the data, the result is set to zero. This way only truly non aliased results are present.

2. The data array can be padded with zeros, this will give exactly the same result as linear convolution but only the first N elements will be returned where N is the number of elements in the original data array.

3. The data array can be mirrored about the zero element.

4. The data array can be wrapped around resulting in circular convolution and time domain aliasing.

If a symmetrical kernel is used then the convolution process can be centred thus aligning the result with the original array.

C.6 Conclusion

The data series analysis in this thesis are discrete and of finite duration. A Kaiser window FIR filter was chosen for this analysis. In order to maximise the foll-off between stop and pass band the parameter M in the Kaiser window was maximised such that circular convolution was still possible using IDL's *convol* function. This resulted in a kernel with the same number of elements as the data to be filtered.

Appendix D

Autocorrelation function

D.1 Introduction

The fitting of the autocorrelation function and the resulting data that is produced is the topic of much discussion at the moment [79, 47]. The velocity that is recorded as a result of the FITACF process is of importance to pulsation research if the radar data is to be used as a quantitative tool rather than as a qualitative tool.

In chapter 6 the radar operation was described. A detailed discussion on the technique for generating the ACF was not appropriate then and will thus be discussed here. The content of this appendix closely follows from a tutorial given at the 2002 Annual SuperDARN Workshop [14].

The radar makes use of a staggered pulse pattern (see figure 6.3) that transmits pulses before the furthest echoes have returned. What follows is an explanation of the process of creating an ACF with a staggered pulse pattern, using a three-pulse pattern for simplicity. A three-pulse pattern is shown in figure D.1. With a three-pulse pattern you can calculate a four lag ACF for each range.

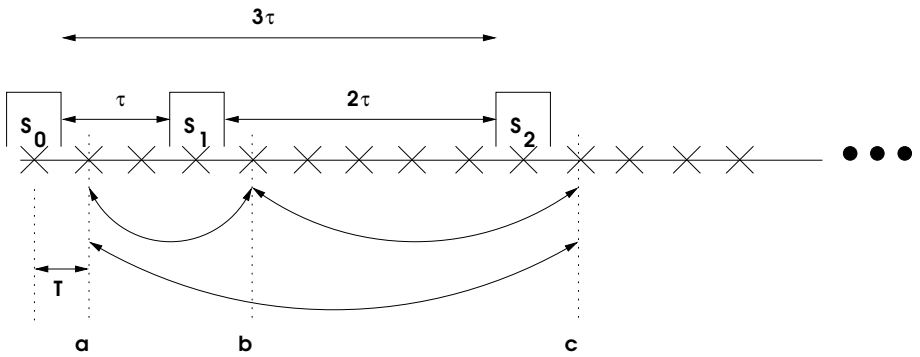

Figure D.1: A three-pulse pattern shown together with the lag and sampling times.

D.2 The transmitted pulses

Let the first transmitted pulse be represented by

$$s(t) = p(t)\exp[j2\pi ft] = s_0.$$

At some time later (τ) a second pulse is transmitted at the same frequency represented by

$$s(t-\tau) = p(t-\tau)\exp[j2\pi f(t-\tau)] = s_1$$

and finally, two lags later, the third pulse is transmitted represented by $s(t-3\tau) = s_2$.

During this whole process the receiver is making samples every T seconds. In the SuperDARN radar this is typically $300\,\mu s$ giving the range resolution of 45 km. These samples are represented as an $\times$ in figure D.1. Following is and illustration of how the ACF is generated for the first range gate using the nomenclature in figure D.1.

D.3 The ACF

Range one is the first sample after each pulse The sampling times are labelled as a,b and c in figure D.1. Each of the samples represents a complex number created by the I and Q samples made by the receiver. The lags are created as follows;

1. Lag zero is made by taking the sample at a and multiplying it with its own complex conjugate, that is, $R_{10} = r_a \cdot r_a^*$, where R_{10} is the ACF value for range one lag zero, r_a is the sample at a and r_a^* are the complex conjugate.

2. Lag one is made by taking the sample at a and multiplying it with the complex conjugate of the sample at b, that is, $R_{11} = r_a \cdot r_b^*$.

3. Lag two is made by taking the sample at b and multiplying it with the complex conjugate of the sample at c, that is, $R_{12} = r_b \cdot r_c^*$.

4. Lag three is made by taking the sample at a and multiplying it with the complex conjugate of the sample at c, that is, $R_{13} = r_a \cdot r_c^*$.

The ACF for range one is then $ACF_1 = R_{10}$, R_{11}, R_{12}, R_{13} where each of the R terms in the series represents an amplitude and phase of the lag term.

For a stationary and well correlated target the amplitude and phase for each of the R terms will be identical. If the target is moving but still well correlated, then the amplitude of the R terms will still be constant, but now there will be a phase difference between the terms related to the Doppler shift of the signal reflected from the moving target. If the target is uncorrelated then the amplitude will fall as the lag time increases.

D.4 FITACF

The FITACF routine makes the assumption that the ACF is characterised by only one frequency, so we get $R_{10} = A_{10} + rand$, $R_{11} = A_{11}e^{\imath\omega\tau} + rand$, $R_{12} = A_{12}e^{\imath 2\omega\tau} + rand$ and $R_{13} = A_{13}e^{\imath 3\omega\tau} + rand$, where A_{nm} is the amplitude of the ACF lag, ω is the principal Doppler frequency and $rand$ random noise terms. From this we can see that the phase terms are linearly related and so ω is determined by a least squares fit to the phase terms. The amplitude terms are modelled using either a linear fit to the log of the power terms or a quadratic fit to the log of the amplitude terms, that is;

$$|R| = Ae^{-\lambda\tau}$$

or

$$|R| = Ae^{-\sigma^2\tau^2}.$$

So $\ln|R| = C - \lambda\tau$ or $\ln|R| = C - \sigma^2\tau^2$. These can be least squares fitted to give either λ or σ.

The power spectrum from the linear fit of the amplitudes is a Lorentzian Power Spectrum, so the half width of the spectrum is $w = 2\lambda$. Similarly the power spectrum for the quadratic fit is a Gaussian Power Spectrum, with the half width $w = 4\sigma\sqrt{\ln 2}$. The fitted curve can then be compared with the original data to determine the accuracy of the fit. This is expressed as a standard deviation of the value of the parameter being used for the fit.

D.5 Limitations

There are various limitations to the way in which the ACF's are generated and fitted. These include ranges aliasing, bad lags and variations in the single frequency assumption in the FITACF procedure.

D.5.1 Range Aliasing

The staggered pulse pattern means that there are pulses that are transmitted before the final echo has returned from all the possible targets. Consider the sample made at point b in figure D.1 the signal that is received could be:

1. A signal from pulse one (s_1) reflected from the ionosphere from a range of $\frac{cT}{2}$.
2. A signal from pulse zero (s_0) reflected from the ionosphere from a range of $\frac{c(4T)}{2}$.

3. The sum of both of these.

When the ACF is created using the sample at point b, the signal received from $\frac{cT}{2}$ away will be correlated with the other samples that have signals from $\frac{cT}{2}$ away. The part of the sample that is from $\frac{c4T}{2}$ away will not be correlated and is considered noise. Similarly when the sample at point b is used to create the ACF for a range $\frac{c4T}{2}$, then the $\frac{cT}{2}$ part of the signal will be noise and thus uncorrelated.

D.5.2 Bad Lags

In figure 6.3 one can see that, given the pulse pattern, there are missing lags at lag 16, 19, 21, 23, 24 and 25. These cannot be avoided given that specific pulse pattern. It is possible to increase the number of pulses to avoid this, but this would lead to more range aliasing as described above.

D.5.3 Multiple frequencies in the ACF

The FITACF assumes that the ACF only contains one principal frequency. If the signal is decorrelated then there may be more frequencies present, but they are described by the modelled power spectrum. This is not always the case and may give rise to incorrect values in the fitting process [47].

D.6 Summary

The radar transmits a staggered pulse pattern and then samples the receiver in quadrature. The quadrature samples are used to create a multi-lag ACF for each range. A process known as FITACF then performs a linear fit on the phase and log of the amplitudes to determine the Doppler frequency ω, the Lorentzian Power spectrum parameter λ, the Gaussian power spectrum parameter σ and the spectral width parameters for the two spectra w_λ and w_σ. These fits are done using a least squares fitting process and so there are estimates as to the accuracy of the fit given as standard deviation errors for each of the parameters. The advantage of this process is that it allows one to sample the ionospheric motions suitably as to resolve large velocity movement of the polar ionosphere. The disadvantage is that there are assumptions made in the fitting process that may exclude certain data.

Appendix E

Field of view plots

The field of view plot is often be used and so requires some explanation. An example of a field of view plot is shown in figure E.1. Each panel of the plot represents a two hour record for a specific radar. The FIT time stamp is shown above each plot for identification. The display elements of each panel are shown in figure E.2. The arrow indicates the direction of the sun earth line. The field of view for each radar is plotted in AACGM coordinates looking from above the north pole. The southern hemisphere radars are thus plotted with their fields of view as seen from inside the earth. This convention is chosen to allow a simultaneous view of both northern and southern radars on the same plot. Plots like this allow one to determine if there is correlated conjugate behaviour between radars in the northern ans southern hemispheres. The centre of the plots thus represents the AACGM pole with dotted lines for latitudes of 80° and 70° respectively. The top of each plot represents the 0° line of AACGM longitude with east measured anti-clockwise and west measured clockwise. The colour for each cell represents the intensity of the parameter plotted, the dark colours indicate low intensity while bright colours indicate higher intensity.

E.1 Method

The geographic locations of six points in each radar cell are known, figure E.3. The geographic locations are then converted to AACGM coordinates so that magnetically conjugate positions can be compared.

To display multiple fields of view on the same plot, the AACGM coordinates are transformed form spherical coordinates to Cartesian by assuming a unit sphere and changing the sign of the southern hemisphere station's longitudes.

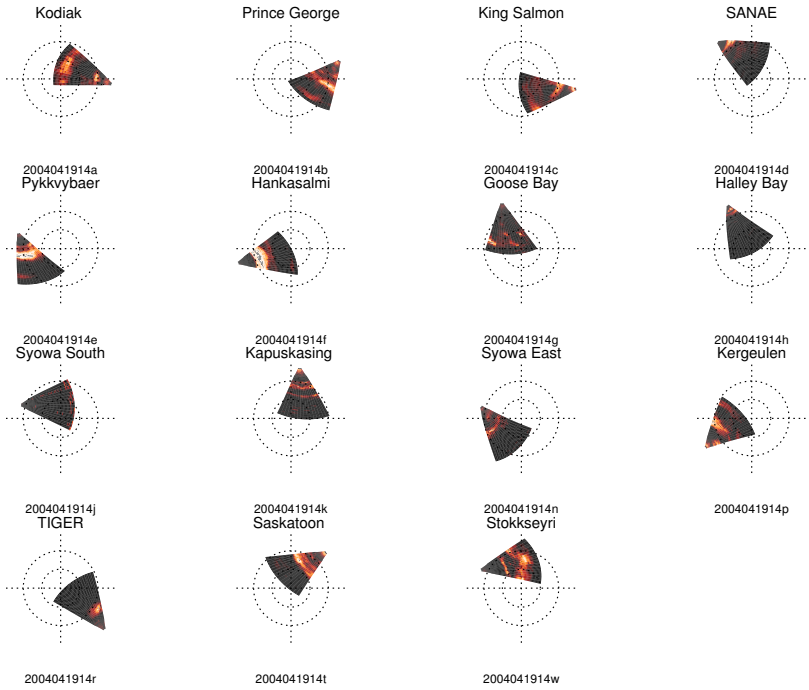

Figure E.1: The SuperDARN network field of view plot.

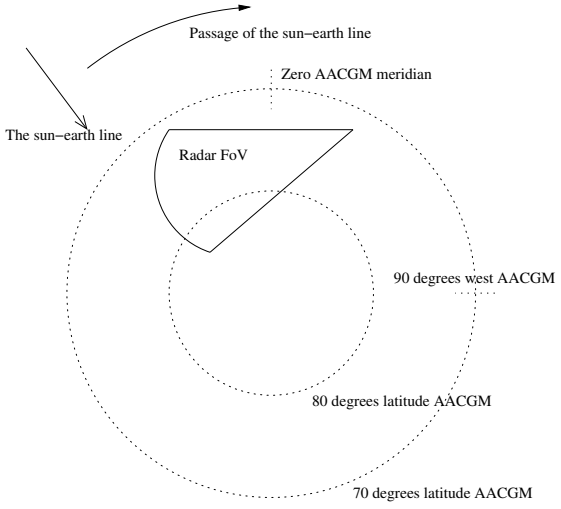

Figure E.2: The elements that make up the field of view plot of figure E.1.

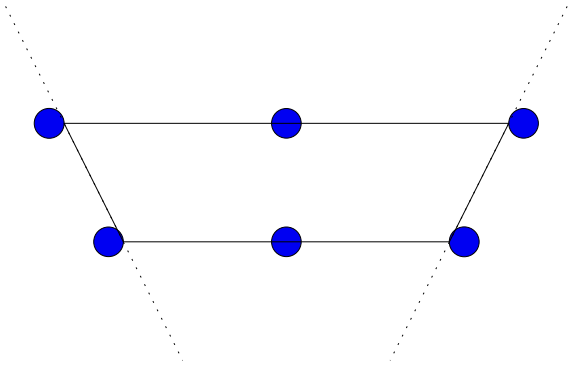

Figure E.3: The geographical location of six points of each radar cell are known.

E.1.1 Change of sign

The sign of the southern hemisphere longitudes are changed so that the field of view of a northern and southern hemisphere station can be displayed for comparison in the same plot. The plots use a static geomagnetic grid with AACGM zero longitude at the top of each field of view. The natural way to show the field of view for a northern hemisphere station would be as seen from above the north pole. In this case, the earth would be seen rotating in an anti-clockwise direction in the reference frame with the sun-earth line fixed. If the southern hemisphere stations were displayed with the same convention, that is with the field of view as seen from above the pole, then the earth would be seen to rotate clockwise with respect to the sun-earth line.

In this study one of the primary interests is the location of pulsation scatter as seen by the radar network. It was felt that a more convenient way to display data from the network would be such that at a glance one would be able to see if there were any conjugate scatter. The change of longitude sign means that the southern hemisphere station are now actually viewed from inside the earth. Although fictitious, this results in both the northern and southern hemisphere stations being viewed from about the north pole.

Appendix F

Merging Calculations

F.1 Introduction

In order to merge the data from two overlapping cells in the SuperDARN network it in necessary to calculate the bearing angles for the cells. If one is interested in the components of the motion in the magnetic poloidal and toroidal directions then you need to calculate the magnetic bearing angles.

F.2 The Components

For a radar cell, the geographic coordinates of six points along the cell are known, see figure F.1. One can use these coordinates to determine the corresponding AACGM coordinates [16]. Once this is done, the bearing of the line through the centre two coordinates is taken as the bearing of the cell measured east of AACGM north.

If you then have data from two overlapping cells that have recorded the bulk motion of the ionosphere and the bearing angles have been determined as in figure F.2, then the

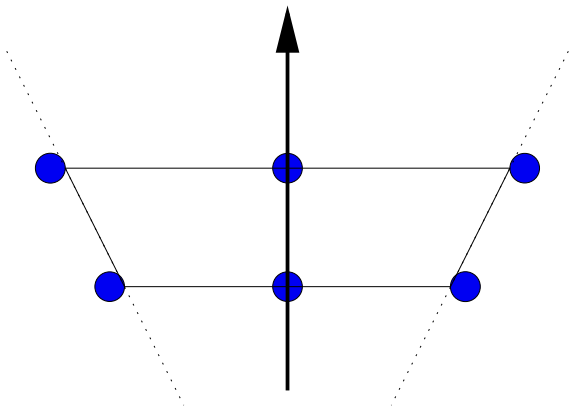

Figure F.1: In a radar cell, the locations of the six points shown are known. The bearing of the cell is then the direction of the line connecting the centre two points.

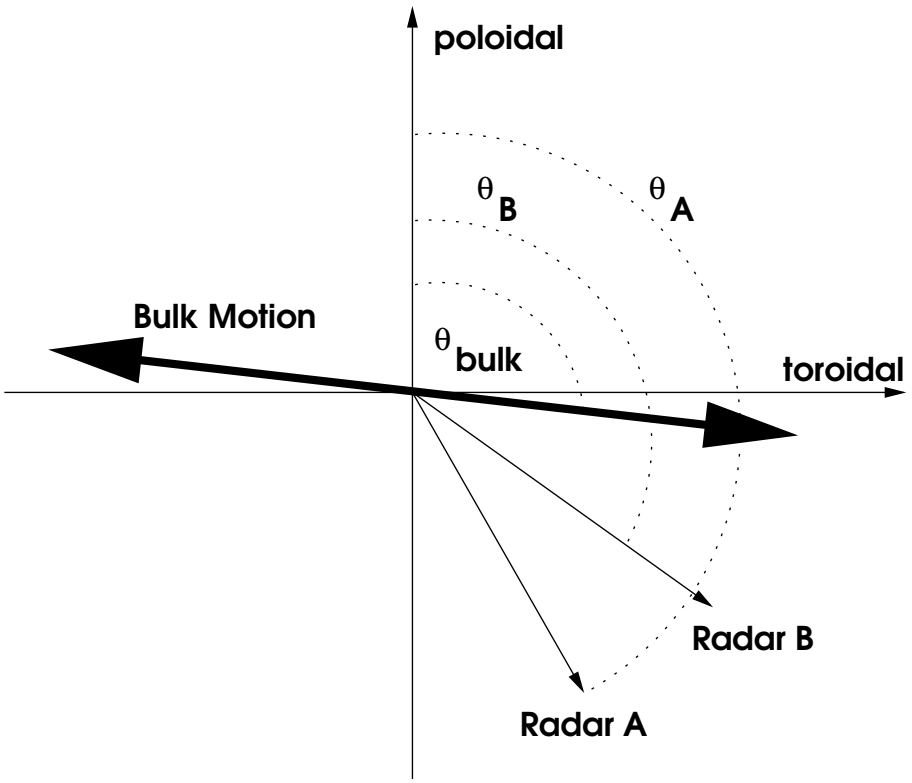

Figure F.2: Radar bearing angles together with an ionospheric bulk motion.

component of the motion that is measured by each radar is given by

$$v_A = v_{bulk} \cdot \hat{A}$$

where v_A is the velocity measured by radar A, v_{bulk} is the velocity of ionospheric irregularities, $\hat{A}$ is a unit vector in the direction of the bearing of the line-of-sight of radar A measured east-of-north. This can then be written as

$$v_A = v_{bulk} \cos\left(\theta_{\hat{A}} - \theta_{\hat{b}}\right)$$

where $\theta_{\hat{A}}$ is the bearing angle of radar A and $\theta_{\hat{b}}$ is the direction of the bulk motion. If expanded out you get

$$v_A = v_{bulk}\left(\cos\theta_{\hat{A}}\cos\theta_{\hat{b}} + \sin\theta_{\hat{A}}\sin\theta_{\hat{b}}\right) = v_{pol}\cos\theta_{\hat{A}} + v_{tor}\sin\theta_{\hat{A}} \tag{F.1}$$

where $v_{pol} = v_{bulk}\cos\theta_{\hat{b}}$ and $v_{tor} = v_{bulk}\sin\theta_{\hat{b}}$.

Similarly you get

$$v_B = v_{pol}\cos\theta_{\hat{B}} + v_{tor}\sin\theta_{\hat{B}} \tag{F.2}$$

Equations F.1 and F.2 can be solved to give

$$v_{tor} = \frac{\cos\theta_{\hat{B}} v_A - \cos\theta_{\hat{A}} v_B}{\sin\left(\theta_{\hat{A}} - \theta_{\hat{B}}\right)} \tag{F.3}$$

$$v_{pol} = -\frac{\sin\theta_{\hat{B}} v_A - \sin\theta_{\hat{A}} v_B}{\sin\left(\theta_{\hat{A}} - \theta_{\hat{B}}\right)} \tag{F.4}$$

F.3 The Error in the Components

Now in order to calculate the uncertainty of a function one can use the fact that if $Z = f(A_i)$, where A_i are the independent variables, then

$$\delta Z = \sqrt{\sum_i \left(\frac{\partial f}{\partial A_i}\right)^2 (\delta A_i)^2} \tag{F.5}$$

So in order to calculate δv_{tor} one would need;

$$\frac{\partial v_{tor}}{\partial v_A} = \frac{\cos\theta_{\hat{B}}}{\sin\left(\theta_{\hat{A}} - \theta_{\hat{B}}\right)}$$

$$\frac{\partial v_{tor}}{\partial v_B} = -\frac{\cos\theta_{\hat{A}}}{\sin\left(\theta_{\hat{A}} - \theta_{\hat{B}}\right)}$$

$$\frac{\partial v_{tor}}{\partial \theta_{\hat{A}}} = \frac{\cos\theta_{\hat{B}}\left[v_B - v_A\cos\left(\theta_{\hat{A}} - \theta_{\hat{B}}\right)\right]}{\sin\left(\theta_{\hat{A}} - \theta_{\hat{B}}\right)^2}$$

$$\frac{\partial v_{tor}}{\partial \theta_{\hat{B}}} = \frac{\cos\theta_{\hat{A}}\left[v_A - v_B\cos\left(\theta_{\hat{A}} - \theta_{\hat{B}}\right)\right]}{\sin\left(\theta_{\hat{A}} - \theta_{\hat{B}}\right)^2}$$

If we were to assume that uncertainty in measuring or determining v_A, v_B, $\theta_{\hat{A}}$ and $\theta_{\hat{B}}$ are constant through a measurement and just focus on what effect the difference in bearing angles for the two cells would have on the calculations we can get from F.5 that

$$\delta v_{tor} \approx \sqrt{\left(\frac{C_1}{\sin\left(\theta_{\hat{A}} - \theta_{\hat{B}}\right)}\right)^2 + \left(\frac{C_2}{\sin\left(\theta_{\hat{A}} - \theta_{\hat{B}}\right)^2}\right)^2}$$

where C_1 and C_2 are constant during the measurement. From this it can be seen that the biggest contributing factor to the uncertainty in the toriodal velocity is the $1/\sin\left(\theta_{\hat{A}} - \theta_{\hat{B}}\right)^2$ term. If the angle between the bearings of the two cells is small, then this term can swamp the calculations. For a difference in bearing angle of 10° there will be a factor of 33m/s uncertainty just from this term.

F.4 Summary

It is possible to calculate to poloidal and toroidal components of the a patch of irregularities moving in the polar ionosphere from the line of sight velocities measured by two overlapping SuperDARN radars. One can also calculate the uncertainty in these calculations and it was found that the largest component of error is the angle between the line of sight of the radars. The smaller the angle between the two radars, the larger the error.

References

[1] IDL Reference Guide. IDL online help, 2005.

[2] Coordinated Data Analysis Web (CDAWeb). Online: http://cdaweb.gsfc.nasa.gov/istp_public/, Accessed 2006.

[3] Ionospheric conductivity model. Online: http://swdcwww.kugi.kyoto-u.ac.jp/ionocond, Accessed 2006.

[4] Storage area network. Online: http://en.wikipedia.org/wiki/Storage_area_network, Accessed 2006.

[5] SuperDARN Radar Locations. Online: http://superdarn.jhuapl.edu/sites/index.html, Accessed 2006.

[6] SuperDARN data archive. Online: http://superdarn.jhuapl.edu/, Accessed 2007.

[7] BAS LPM network Locations. Online: http://www.antarctica.ac.uk/bas_research/our_research/az/lpm/locations.php, Accessed 2008.

[8] Lagrange Points. Online: http://en.wikipedia.org/wiki/Image:Lagrange_very_massive.svg, Accessed 2008.

[9] Lorem ipsum. Online: http://en.wikipedia.org/wiki/Lorem_ipsum, Accessed 2008.

[10] H. Alfven. Existence of electromagnetic-hydromagnetic waves. *Nature*, 150(3805):405–406, 1942.

[11] I. Amidror. Scattered data interpolation methods for electronic imaging systems: a survey. *Journal of Electronic Imaging*, 11(2):157–176, 2002.

[12] S. Baisch and G. Bokelmann. Spectral analysis with incomplete time series: an example from seismology. *Computers and Geosciences*, 25(7):739–750, 1999.

[13] G. L. Baker, E. F. Donovan and B. J. Jackel. A comprehensive survey of auroral latitude Pc5 pulsation characteristics. *Journal of Geophysical Research*, 108(A10):1384, 2003.

[14] K. Baker. FITACF - A SuperDARN Tutorial. In *Proceedings of the 2002 SuperDARN Workshop*, 2002.

[15] K. B. Baker, R. A. Greenwald, J. P. Villian and S. Wing. Spectral characteristics of High Frequency (HF) backscatter for high latitude ionospheric irregularities: Preliminary analysis of statistical properties. Interim report, Johns Hopkins University Applied Physics Laboratory, Laurel, MD., 1988.

[16] K. B. Baker and S. Wing. A new magnetic coordinate system for conjugate studies at high latitudes. *Journal of Geophysical Research*, 94:9139–9143, 1989.

[17] J. Bortnik, J. Cutler, C. Dunson and T. Bleier. An automatic wave detection algorithm applied to Pc1 pulsations. *Journal of Geophysical Research*, 112, 2007.

[18] L. Chen and A. Hasegawa. A theory of long-period magnetic pulsations. I - Steady state excitation of field line resonance. II - Impulse excitation of surface eigenmode. *Journal of Geophysical Research*, 79:1024–1037, 1974.

[19] P. Chi and C. Russell. Interpretation of the cross-phase spectrum of geomagnetic pulsations by the field line resonance theory. *Geophysical Research Letters*, 25(24):4445–4448, 1998.

[20] G. Chisham, M. P. Freeman and T. Sotirelis. A statistical comparison of SuperDARN spectral width boundaries and DMSP particle precipitation boundaries in the nightside ionosphere. *Geophysical Research Letters*, 31(2), 2004.

[21] G. Chisham, M. Lester, S. Milan, M. Freeman, W. Bristow, A. Grocott, K. McWilliams, J. Ruohoniemi, T. Yeoman, P. Dyson et al. A decade of the Super Dual Auroral Radar Network (SuperDARN): scientific achievements, new techniques and future directions. *Surveys in Geophysics*, 28(1):33–109, 2007.

[22] S. W. H. Cowley, A. P. van Eyken, E. C. Thomas, P. J. S. Williams and D. M. Willis. Studies of the cusp and auroral zone with incoherent scatter radar - The scientific and technical case for a polar-cap radar. *Journal of Atmospheric and Terrestrial Physics*, 52:645–663, Aug. 1990.

[23] L. Davies and U. Gather. The Identification of multiple outliers. *Journal of the American Statistical Association*, 88(423):782–792, 1993.

[24] J. Dungey. Electrodynamics of the outer atmosphere. *The Physics of the Ionosphere*, page 229.

[25] J. Dungey. The structure of the exosphere or adventures in velocity space. *Geophysics: The Earth's Environment*, pages 505–550, 1963.

[26] P. L. Dyson. Relationships between the rate of change of phase path/Doppler shift/and angle of arrival. *Journal of Atmospheric and Terrestrial Physics*, 37:1151–1154, 1975.

[27] M. Engebretson, K. H. Glassmeier, M. Stellmacher, W. J. Hughes and H. Lühr. The dependence of high-latitude Pc5 wave power on solar wind velocity and on the phase of high-speed solar wind streams. *Journal of Geophysical Research*, 103(A11):26271–26284, 1997.

[28] F. Fenrich, J. Samson, G. Sofko and R. Greenwald. ULF high-and low-m field line resonances observed with the Super Dual Auroral Radar Network. *Journal of Geophysical Research*, 100(A11).

[29] J. L. Green and S. Boardsen. Plasma and radio wave imaging survey of the earth's magnetosphere. Online: http://nssdc.gsfc.nasa.gov/~boardsen/wave/wsurvey.html, Accessed 2006.

[30] R. A. Greenwald, K. B. Baker, J. R. Dudeney, M. Pinnock, T. B. Jones, E. C. Thomas, J. P. Villain, J. C. Cerisier, C. Senior, C. Hanuise et al. DARN/SuperDARN. *Space Science Reviews*, 71(1):761–796, 1995.

[31] C. Hanuise, C. Senior, J. Cerisier, J. Villain, R. Greenwald, J. Ruohoniemi and K. Baker. Instantaneous mapping of high-latitude convection with coherent HF radars. *Journal of Geophysical Research*, 98(A10).

[32] S. K. F. Hattingh and P. R. Sutcliffe. Pc3 pulsation eigenperiod determination at low latitudes. *Journal of Geophysical Research*, 92:12433–12436, 1987.

[33] W. J. Hughes. The effect of the atmosphere and ionosphere on long period magnetospheric micropulsations. *Planetary and Space Science*, 22:1157–1172, 1974.

[34] W. J. Hughes and D. J. Southwood. The screening of micropulsation signals by atmosphere and ionosphere. *Journal of Geophysical Research*, (81):3234–3240., 1976.

[35] J. A. Jacobs, Y. Kato, S. Matsushita and V. A. Troitskaya. Classification of Geomagnetic Micropulsations. *Journal of Geophysical Research*, 69:180, 1964.

[36] M. Kivelson and C. Russell, editors. *Introduction to Space Physics*. Cambridge University Press, New York, NY, 1995.

[37] M. G. Kivelson and D. J. Southwood. Resonant ULF waves: A new interpretation. *Geophysical Research Letters*, (12):49–52, 1985.

[38] J. D. Krauss. *Antennas*. Mc Graw Hill, New York, 1988.

[39] E. Lee, I. Mann, T. Loto'aniu and Z. Dent. Global Pc5 pulsations observed at unusually low L during the great magnetic storm of 24 March 1991. *Journal of Geophysical Research*, 112(A5):A05208, 2007.

[40] L. G. Magnus. Expanding the capabilities of the DPS Ionosonde system. Master's thesis, Rhodes University, 2001.

[41] D. J. McComas, S. J. Bame, P. Barker, W. C. Feldman, J. L. Phillips, P. Riley and J. W. Griffee. Solar Wind Electron Proton Alpha Monitor (SWEPAM) for the Advanced Composition Explorer. *Space Science Reviews*, 86(1):563–612, 1998.

[42] R. L. McPherron. Magnetic Pulsations: their sources and relation to solar wind and geomagnetic activity. *Surveys in Geophysics*, 26(5):545–592, 2005.

[43] A. V. Oppenheim and R. W. Schafer. *Discrete-time signal processing.* Prentice-Hall, Upper Saddle River, NJ, 1989.

[44] F. Plaschke, K. Glassmeier, O. Constantinescu, I. Mann, D. Milling, U. Motschmann and I. Rae. Statistical analysis of ground based magnetic field measurements with the field line resonance detector. *Annales Geophysicae*, 26:3477–3489, 2008.

[45] P. Ponomarenko, F. Menk and C. Waters. Visualization of ULF waves in SuperDARN data. *Geophysical Research Letters*, 30(18), 2003.

[46] P. Ponomarenko, C. Waters, M. Sciffer, B. Fraser and J. Samson. Spatial structure of ULF waves: Comparison of magnetometer and Super Dual Auroral Radar Network data. *Journal of Geophysical Research*, 106(A6), 2001.

[47] P. V. Ponomarenko and C. L. Waters. Spectral width of SuperDARN echoes: measurement, use and physical interpretation. *Annales Geophysicae*, 24:115–128, 2006.

[48] D. Rankin and R. Kurtz. Statistical study of micropulsation polarizations (Micropulsations polarization characteristics from statistical spectrum analysis). *Journal of Geophysical Research*, 75:5444–5458, 1970.

[49] J. Ruohoniemi and R. Greenwald. Rates of scattering occurrence in routine HF radar observations during solar cycle maximum. *Radio Science*, 32(3).

[50] J. M. Ruohoniemi and K. B. Baker. Large-scale imaging of high-latitude convection with SuperDARN HF radar observations. *Journal of Geophysical Research*, 103(20,797), 1998.

[51] J. M. Ruohoniemi, R. A. Greenwald, K. B. Baker and J. C. Samson. HF radar observations of Pc5 field line resonances in the midnight/early morning sector. *Journal of Geophysical Research*, (96):15697–15710, 1991.

[52] J. C. Samson, B. G. Harrold, J. M. Ruohoniemi, R. A. Greenwald and A. D. M. Walker. Field line resonances associated with MHD waveguides in the earth's magnetosphere. *Geophysical Research Letters*, (19):441–444, 1992.

[53] J. C. Samson, J. A. Jacobs and G. Rostoker. Latitude-dependant characteristice of long-period geomagnetic micropulsations. *Journal of Geophysical Research*, 76(16):3675–3683, 1971.

[54] T. Sarris, X. Li and H. Singer. A long-duration narrowband Pc5 pulsation. *Journal of Geophysical Research*, 114, 2009.

[55] H. J. Singer, L. Matheson, R. Grubb, A. Newman and S. D. Bouwer. Monitoring space weather with the GOES magnetometers. In *SPIE Proceedings*, volume 2812, 1996.

[56] C. W. Smith, J. L'Heureux, N. F. Ness, M. H. Acuña, L. F. Burlaga and J. Scheifele. The ACE magnetic fields experiment. *Space Science Reviews*, 86(1):613–632, 1998.

[57] S. Smith. *The scientist and engineer's guide to digital signal processing*. California Technical Publishing San Diego, CA, USA, 1997.

[58] D. J. Southwood. Some features of field line resonances in the magnetosphere. *Planetary and Space Science*, 22:483–491, 1974.

[59] J. A. E. Stephenson and A. D. M. Walker. HF radar observations of Pc5 ULF pulsations driven by the solar wind. *Geophysical Research Letters*, 29(9):11, 2002.

[60] B. Stewart. On the great magnetic disturbance which extended from August 28 to September 7, 1859, as recorded by photography at the Kew Observatory. *Philosophical Transactions of the Royal Society of London*, 151:423–430, 1861.

[61] P. R. Sutcliffe. Fourier transformation as a method of reducing the sampling interval of a digital time series. *Computers & Geosciences*, 14(1):125–129, 1988.

[62] P. R. Sutcliffe, S. K. F. Hattingh and H. F. V. Boshoff. Longitudinal effects on the eigenfrequencies of low-latitude Pc3 pulsations. *Journal of Geophysical Research*, 92:2535–2543, 1987.

[63] P. R. Sutcliffe and A. W. V. Poole. The relationship between ULF geomagnetic pulsations and ionospheric Doppler oscillations: model predictions. *Planetary and Space Science*, 38(12):1581–1589, 1990.

[64] J. P. H. Taylor and A. D. M. Walker. Accurate approximate formulae for toroidal standing hydromagnetic oscillations in a dipolar geomagnetic field. *Planetary and Space Science*, 32(9):1119–1124, 1984.

[65] N. Trivedi, B. Arora, A. Padilha, J. Da Costa, S. Dutra, F. Chamalaun and A. Rigoti. Global Pc5 geomagnetic pulsations of March 24, 1991, as observed along the American sector. *Geophysical Research Letters*, 24(13).

[66] N. Tsyganenko. Modeling the Earth's magnetospheric magnetic field confined within a realistic magnetopause. *Journal of Geophysical Research*, 100(A4):5599–5612, 1995.

[67] A. Walker, R. Greenwald and K. Baker. HF radar observations of pulsations near the magnetospheric cusp. *Journal of Geophysical Research*, 91, 1986.

[68] A. D. M. Walker. Modelling of Pc5 pulsation structure in the magnetosphere. *Planetary and Space Science*, 28:213–223, 1980.

[69] A. D. M. Walker. The SHARE Radar at SANAE, Antarctica. *South African Journal of Science*, 98(5-6):257–263, 2002.

[70] A. D. M. Walker. Excitation of field line resonances by sources outside the magnetosphere. *Annales Geophysicae*, 23(10):3375–3388, 2005.

[71] A. D. M. Walker. *Magnetohydrodynamic Waves in Geospace*. The Institute of Physics, Bristol, 2005.

[72] A. D. M. Walker, R. A. Greenwald, W. F. Stuart and C. A. Green. Stare auroral radar observations of Pc5 geomagnetic pulsations. *Journal of Geophysical Research*, (84):3373–3388, 1979.

[73] A. D. M. Walker, J. M. Ruohoniemi, K. B. Baker, R. A. Greenwald and J. C. Samson. Spatial and temporal behavior of ULF pulsations observed by the Goose Bay HF radar. *Journal of Geophysical Research*, (92):12187–12202, 1992.

[74] C. Waters, J. Samson and E. Donovan. Variation of plasmatrough density derived from magnetospheric field line resonances. *Journal of Geophysical Research*, 101:24–24, 1996.

[75] C. L. Waters. ULF resonance structure in the magnetosphere. *Advances in Space Research*, 25(7):1541–1558, 2000.

[76] A. N. Wright. Dispersion and wave coupling in inhomogeneous MHD waveguides. *Journal of Geophysical Research*, (99):159–167, 1994.

[77] D. Wright, T. Yeoman, L. Baddeley, J. Davies, R. Dhillon, M. Lester, S. Milan and E. Woodfield. High resolution observations of spectral width features associated with ULF wave signatures in artificial HF radar backscatter. *Annales Geophysicae*, 22(1):169–182, 2004.

[78] T. K. Yeoman and D. M. Wright. ULF waves with drift resonance and drift-bounce resonance energy sources as observed in artificially-induced HF radar backscatter. *Annales Geophysicae*, (19):159–170, 2001.

[79] A. S. Yukimatu, M. Tsutsumi, H. Yamagishi and N. Sato. A new method for monitoring and removing SuperDARN radar DC offsets. *Advances in Polar Upper Atmosphere Research*, 16:181–192, 2002.

[80] C. Ziesolleck, F. Fenrich, J. Samson and D. McDiarmid. Pc5 field line resonance frequencies and structure observed by SuperDARN and CANOPUS. *Journal of Geophysical Research*, 103(A6), 1998.

[81] C. W. S. Ziesolleck and D. R. McDiarmid. Auroral latitude Pc5 field line resonances: quantized frequencies, spatial characteristics, and diurnal variation. *Journal of Geophysical Research*, 99:5817, 1994.

The end!